NTNU

Norwegian University of
Science and Technology

Assessment of Marine Riser Joints During Offshore Drilling Operation

Martine Gripp Bay

Marine Technology
Submission date: August 2016
Supervisor: Svein Sævik, IMT
Co-supervisor: Catalin Toderan, Bureau Veritas, Paris

Norwegian University of Science and Technology
Department of Marine Technology

Move Forward with Confidence

BUREAU VERITAS proposal
N° DTO4 – 6 m Thesis

Bureau Veritas Marine&Offshore Division

Assessment of Marine Riser Joints during Offshore Drilling Operation

Written	Validated	Revision	Date
Catalin Toderan Subsea Manager		**0**	**25/06/2015**

TABLE OF CONTENTS

1 INTRODUCTION

1.1 Scope

The present document gives the scope, the context and the technical description of a project relating to the assessment of drilling risers, subject of a six month internship thesis framework.

1.2 Context – Offshore Drilling Process

Offshore drilling is performed from various types of drilling rigs, known also as mobile offshore drilling units (MODU). These rigs may be fixed on the seabed (platforms, jack-up) or floating units (semi-submersible, drillships). The purpose of drilling operations is to create and to commission a well on the seabed, in contact with a hydrocarbon reservoir and equipped for production of oil/gas.

Drilling equipment installed onboard is to ensure a very complex process. This process is generally divided as follows:

1. Mechanical drilling

   Drilling is performed by inducing a torque in the drilling string, composed by successive segments of pipe and ended with a drill-bit in contact with the geological formation. Depending on the rig, the following types of equipment are involved:

   - Derrick, masts
   - Rotary tables
   - Topdrives (electrical engines)
   - Hoisting/lifting equipment

2. Well barriers and well control

   Well control is the part of the process which is the most critical from safety/environmental point of view. The purpose is to ensure successive barriers between the well and the rig in order to control at any moment of the operation the events of blowout or gas release.

   Well control involves:

   - Drilling mud circuit (water mud or oil mud)
   - Marine (drilling) riser : the subject of the proposed work
   - Blow out preventer (BOP) and associated equipment.

3. Well completion

   Well completion involves the installation and cementing of casing, as well as the installation of production equipment

4. Well testing

   Well testing involves several tests for determining the main characteristics of a drilled well (pressure, temperature, chemical analysis of hydrocarbons).

The present document proposes a work focusing on the integrity of drilling (marine riser). This equipment is an important part of well control and an interface between all parts of the process.

1.3 Drilling risers

Drilling risers (or marine risers) are one of the most safety critical systems for offshore drilling operations. They provide a link between the drilling rig and the well, ensuring a barrier between the sea and the drilling fluid (mud) and protecting the drilling equipment (pipe, string) during operations (see Fig 1).

Drilling risers are generally used in water depth between 90m to 2000m. Recent developments of very deep offshore rigs propose various designs of risers for 3000m or more. Risers are typically rigid segments fabricated in steel, connected with specific joints.

If several existing industrial standards (API, ISO or NORSOK) provide technical requirements for the assessment of marine risers integrity, there is no standard today for the direct assessment of risers' joints. TH HILL, a Bureau Veritas Group's enterprise located in Houston and specialized in drilling equipment, develops now such a new standard. The thesis proposed here will address a part of this work, relating to the mechanical modelling of risers and risers' joints under the effect of environmental and functional loads.

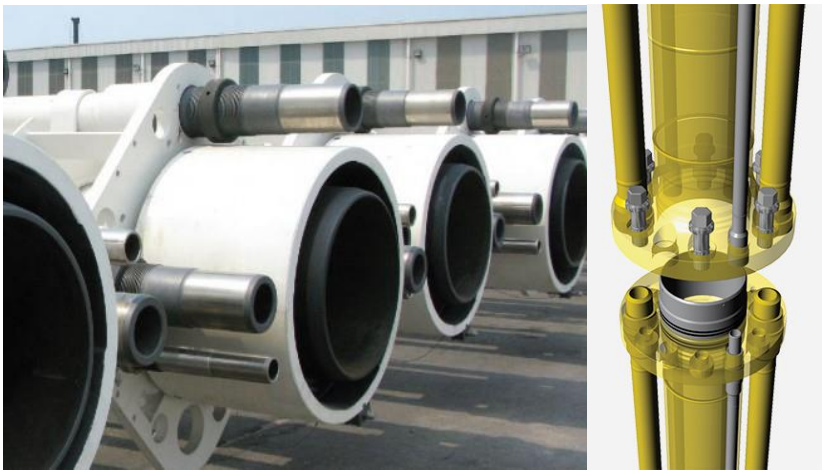

Fig 1 : Examples of drilling risers joints

1.4 BV Organization for this internship thesis

This thesis will be coordinated by the following personnel:

Thesis supervisor : Catalin Toderan **Tel : +33 (0)1 55 24 74 87** **Fax : +33 (0)1 47 14 70 01** **E-mail : catalin.toderan@bureauveritas.com**
BV Unit Manager : Laurent Leblanc **Tel : +33 (0)1 55 24 72 43** **Fax : +33 (0)1 47 14 70 01** **E-mail : laurent.leblanc@bureauveritas.com**

All correspondences, technical documents and deliverables will be written in English.

2 TECHNICAL PROPOSAL

2.1 Scope of work

The scope of this internship thesis is to provide a methodology for the mechanical assessment of marine risers' joints including:

- A report providing a documentation on existing technology for risers and joints
- A method for estimating the environmental loads (waves and currents) and their cycles for a given offshore site, starting from a scatted diagram and meteorological data; the definition of this method requires numerical tests using software available at Bureau Veritas : Hydrostar, FlexCom
- A method for estimating the effect of vortex induced vibrations (VIV) on riser's structure, for fatigue assessment purpose; this will require a set of tests using a specific module of FlexCom
- A structural modelling of risers and risers joints using global and local finite elements models using one of the generic tool available at BV : ABAQUS or NASTRAN
- A test of the model with applied loads for the assessment of joints from yielding, buckling and fatigue point of view.

The scope described above may be restrained or extended, depending on the findings of each phase and on the available time.

2.2 Deliverables

The deliverables of the proposed internship will be a thesis report covering all aspects of the scope. This document has to address the description of the work and will provide technical interpretations of findings.

Preface

This master thesis is a part of the 5- year Master of Science program in Marine Technology at NTNU. The thesis has been a collaboration with NTNU and Bureau Veritas, with supervision from Svein Sævik from IMT and Catalin Toderan from Bureau Veritas. The work has been carried out during spring semester 2016 at Bureau Veritas' head office in Paris, France.

Parts of the literature study is based on the project work carried out in the fall 2015, as a preparation project for the master thesis. The title of the thesis is marine riser joints during offshore drilling operation, and the purpose is to create a methodology for the mechanical assessment of marine riser joints. The assignment was suggested by Catalin Toderan from Bureau Veritas.

The majority of the time has been used to create a the model in Flexcom and perform the different analysis. Research of existing technology and standards have also been an important part of the work. All input data, design and methodology have been discussed and evaluated with help from the different departments at Bureau Veritas.

Paris, 1st of August

Martine Gripp Bay

Acknowledgment

I would like to thank Svein Sævik for the great help and guidance he has offered me during the thesis work. The weekly guidance and discussions have been very important for me. In addition I would like to thank Damien Ameline from Bureau Veritas, for the discussions and help with software related issues in Flexcom. I would also like to thank Martin Dumont from Bureau Veritas, for performing the analysis in Ariane, and Sime Malenica, Yann Giorgiutti and Guillaume De Hauteclocque from Bureau Veritas, for their contribution to the discussions during the thesis work. I would also like to thank Catalin Toderan from Bureau Veritas, for the proposal of the master thesis and for providing information and discussion about the topic.

Summary

Riser technology is pushed to its limits as the demand for deeper drilling operations increases. There exist no standards for the mechanical assessment of marine riser joints today, however new standards are under development at TH HILL, a Bureau Veritas enterprise in Texas. The work in this thesis focuses on parts of the development work, more specifically creation of a methodology of the riser and riser joints, with respect to strength and fatigue.

A documentation of the existing technology for riser and riser joints have been presented in this thesis, and it includes an overview of the available products in the industry and standards of riser components and analysis methodologies. Theory of the drilling riser system and the different analysis, have also been presented in the thesis.

The global load analysis and fatigue analysis are carried out with Flexcom. The vortex-induced vibration analysis is performed through an interface between SHEAR7 and Flexcom. The second order vessel motions are calculated with Ariane. The methodology is developed based on one case study, and the input data for the geometry is based on the documentation on the existing technology. All input data have been carefully selected and discussed with employees from different sections at Bureau Veritas, who holds a broad industry experience within the field. Based on these discussions, a number of sensitivity studies and investigations have been conducted. This include definition of boundary conditions, current direction, wave effect, application of second order vessel motions, simplified second order vessel motions and stress concentration factors. From these investigations, a final analysis model has been established and one combination of current, wind and wave direction has been investigated.

The final analysis model consists of current, waves and second order motions. The current velocity is 1.13m/s and the wind velocity is 22.5m/s. The current profile is based on a combination of an internal metocean report from Bureau Veritas, and the API standard *Interim Guidance on Hurricane Conditions in the Gulf of Mexico* (API, 2007). The riser is connected to the vessel, which limits the significant wave height to 6m. The irregular waves are applied with a JONSWAP spectrum and the second order vessel motions are calculated based on a dynamic positioning system with maximum offset of 20m. In the global load analysis in Flexcom, yield and buckling

have been investigated. The worst sea states have been selected based on the resultant moment for a 1-hour analysis. The effective tension, bending moments and shear force, have been studied for a 3-hour analysis. Fatigue from waves and current have been investigated in two separate analyses. The fatigue analysis in Flexcom investigates the affect from waves by use of three cycle counting methods, i.e. rainflow, spectrum and statistics. The vortex-induced vibration analysis investigates the effect from current, based on the eigenvalue analysis in Flexcom.

The results from the worst sea states in the global load analysis showed that the highest moments occurred at the bottom and at the top of the riser. Sea state 8, with Hs=6m and Tp=11.5s, gave the highest moment at the bottom, and sea state 6, with Hs=6m and Tp=9.5s, gave the highest moment at the top of the riser. The standard deviation was largest at the bottom of the riser, and the shear force was highest at the top. The effective tension showed that a small part of the riser was in compression, but this has been neglected due to the results from hand calculations.

The results from the fatigue analysis showed that the damage due to waves, was close to zero for all sea states. Flexcom calculates the damage with an accuracy of 1.0E-5, so hand calculations of the damage for selected sea states was therefore carried out. From the analysis with stress concentration factor 10, sea state 6, 5 and 4 showed a reduction in lifetime at the bottom and at the top of the riser. The highest damage was at the top of the riser. A stress concentration factor equal to 10 is most likely unrealistic, but it showed that Flexcom performs fatigue calculations. The rainflow counting method gave the highest damage on the riser, compared to the statistics and spectrum methods. The analysis with no second order vessel motions gave also almost zero damage, and the results were exactly the same as the analysis with second order vessel motions. Based on these results, the complexity of the methodology can be reduced by excluding the calculations in Ariane. The results from the vortex-induced vibration analysis showed that the damage due to current was highest at the bottom. The damage was, however quite low over the whole riser. With a stress concentration factor of 9, the results showed significant damage of 0.47, at the bottom of the riser.

Based on the results from the different analysis, the potential of the methodology is shown, and it can hopefully be a useful tool when developing new standards for deeper water depths.

Sammendrag

Stigerørteknologien blir presset til sine ytterste grenser når etterspørselen etter dypere boreoperasjoner øker. Det finnes ingen standarder for den mekaniske vurderingen av marine stigerørsledd i dag, men nye standarder er under utvikling hos TH HILL, en Bureau Veritas bedrift i Texas. Arbeidet i denne avhandlingen fokuserer på deler av utviklingsarbeidet, mer spesifikt etablering av en metodikk for stigerør og stigerørsledd, med hensyn til styrke og utmatting.

En dokumentasjon av eksisterende teknologi for stigerør og stigerørsleddene har blitt presentert i denne avhandlingen og den inkluderer en oversikt over tilgjengelige produkter i bransjen og standarder for stigerørskomponenter og analysemetodikk. Teori av borestigerørssystemet og de ulike analysene, har også blitt presentert i denne avhandlingen.

Den globale lastanalysen og utmattingsanalysen er utført med Flexcom. Den virvelinduserte vibrasjonsanalysen er utført via en kobling mellom SHEAR7 og Flexcom. Andre ordens fartøysbevegelse er beregnet med Ariane. Metodikken er utviklet basert på ett case-studie, og input dataen for geometrien er basert på dokumentasjonen av eksisterende teknologi. All input data er nøye utvalgt og drøftet med ansatte fra ulike seksjoner på Bureau Veritas, som innehar en bred bransjeerfaring innenfor feltet. Basert på disse diskusjonene, har en rekke sensitivitetsstudier og undersøkelser blitt gjennomført. Dette inkluderer definisjonen av grensebetingelser, strømretning, bølge effekt, applikasjon av andre ordens fartøysbevegelser, forenklet andre ordens fartøysbevegelser og spenningskonsentrasjonsfaktorer. Fra disse undersøkelsene, har en endelig analysemodell blitt etablert og en kombinasjon av strøm, vind og bølgeretning har blitt undersøkt.

Den endelige analysemodellen består av strøm, bølger og andre ordens bevegelser. Strømningshastigheten er 1.13 m/s og vindhastigheten er 22.5 m/s. Strømprofilen er basert på en kombinasjon av en intern metocean rapport fra Bureau Veritas, og API standarden *Interim Guidance on Hurricane Conditions in the Gulf of Mexico* (API, 2007). Stigerøret er koblet til fartøyet, noe som begrenser den signifikante bølgehøyden til 6m. De irregulære bølgene påføres med et JONSWAP spektrum og andre ordens fartøysbevegelser er beregnet basert på et dynamisk posisjoneringssystem med maksimalt avvik på 20m. I den globale lastanalysen i Flexcom, har

flyt og knekking blitt undersøkt. De verste sjøtilstandene har blitt valgt basert på resultant momentet for en 1-times analyse. Den effektive spenningen, bøyemomentene og skjærkraften, har blitt studert for en 3-timers analyse. Utmatting fra bølger og strøm har blitt undersøkt i to separate analyser. Utmattelsesanalysen i Flexcom undersøker påvirkningen fra bølger ved bruk av tre tellemetoder av stress sykluser dvs. rainflow, spektrum og statistikk. Den virvelinduserte vibrasjonsanalysen undersøker påvirkningen fra strøm, basert på egenverdianalysen i Flexcom.

Resultatene fra de verste sjøtilstander i det globale lastanalysen viste at de høyeste momentene oppsto ved bunnen og ved toppen av stigerøret. Sjøtilstand 8, med Hs=6m og Tp=11.5s, gav det høyeste momentet på bunnen, og sjøtilstand 6, med Hs=6m og Tp=9.5s, gav det høyeste momentet øverst på stigerøret. Standardavviket var størst ved bunnen av stigerøret, og skjærkraften var størst ved toppen. Den effektive spenningen viste at en liten del av stigerøret var i kompresjon, men dette har blitt neglisjert på grunn av resultatene fra håndberegningene.

Resultatene fra utmattingsanalysen viste at skadene på grunn av bølger, var tilnærmet null for alle sjøtilstandene. Flexcom beregner skaden med en nøyaktighet på 1.0E-5 så håndberegninger av skaden for utvalgte sjøtilstander ble derfor utført. Fra analysen med spenningskonsentrasjonsfaktor 10, viste sjøtilstand 6, 5 og 4 en reduksjon i levetiden ved bunnen og ved toppen av stigerøret. Den høyeste skaden var på toppen av stigerøret. En spenningskonsentrasjonsfaktor lik 10 er mest sannsynlig urealistisk, men den viste at Flexcom utførte utmattingsberegninger. Rainflow tellemetoden gav den høyeste skaden på stigerøret, sammenlignet med statistikk og spektrum metodene. Analysen uten noen andre ordens fartøysbevegelser gav også nesten null skade, og resultatene var nøyaktig lik analysen med andre ordens fartøysbevegelser. Basert på disse resultatene, kan kompleksiteten av metoden reduseres ved å utelukke beregningene i Ariane. Resultatene fra den virvelinduserte vibrasjonsanalysen viste at skader på grunn av strøm var høyest ved bunnen. Skaden var likevel ganske lav over hele stigerøret. Med en spenningskonsentrasjons faktor på 9 viste resultatene vesentlig skade på 0,47, ved bunnen av stigerøret.

Basert på resultatene fra de ulike analysene, er potensialet for metoden vist og forhåpentligvis kan den være et nyttig verktøy for utvikling av nye standarder for dypere vanndybder.

Contents

List of Figures

List of Tables

Nomenclature

Acronyms

ALS Accidental limit state

API American Petroleum Institute

BOP Blow out preventer

CCA Convected coordinate axis

CCM Convected coordinate method

CF Cross-flow

DFF Design fatigue factor

DNV Det Norske Veritas

DOF Degrees of freedom

DP Dynamic positioning

DTL Dynamic tension limit

FEA Finite element analysis

FEM Finite element method

FLS Fatigue limit state

GoM Gulf of Mexico

IL In-line

IMT Department of Marine Technology

ISO International Organization for Standardization

LF Low frequency

LFJ Lower flex joint

LMRP Lower marine riser package

MWL Mean water level

PDF Probability density function

PGB Permanent guide base

QTF Quadratic transfer function

RAO Response amplitude operator

SLS Serviceability limit state

SCF Stress concentration factor

TGB Temporary guide base

ULS Ultimate limit state

UPJ Upper flex joint

VIV Vortex-induced vibrations

WF Wave frequency

Roman symbols

A_0 Surface area in original coordinate frame

A External cross-section area in Morison's equation

A_e External cross-section area

A_i Internal cross-section area

A_j Wave amplitude

$\bar{a}$ Intercept of log N axis in the S-N curve

C_0 Initial configuration

C_{0n} Reference of the rotation center

C Fitting parameter in Paris Erdogan law

C Damping matrix

C_D Quadratic drag coefficient

C_{DL} Linear drag coefficient

C_n Deformed configuration at time t

C_{n+1} New incremental configuration at time t+Δt

$\tilde{c}$ Viscous damping density function

c^h Hydrodynamic damping per unit length

D Miner-Palmgren damage sum / Diameter of cylinder

D_{fat} Long-term fatigue damage

dS_0 Length of segment PQ before deformation

dS_n Length of segment PQ after deformation

E Strain tensor in original coordinate frame

$\tilde{\mathbf{E}}$ Strain tensor co-rotated coordinate frame

f_0 Body forces in original coordinate frame / Eigenfrequency

f_{osc} Oscillation frequency

f_v Vortex shedding frequency

g Gravitational acceleration

Hs Significant wave height

$\mathbf{I}_i$ Original base vector

$\mathbf{I}_j$ Original coordinate frame

$\tilde{\mathbf{I}}_i$ Rotated base vector along C_{0n}

$\tilde{\mathbf{I}}_j$ Co-rotated coordinate frame

$\bar{\mathbf{i}}_i$ Nodal base vector

$\mathbf{i}_i$ Base vector for C_{0n}

$\mathbf{i}_i^0$ Base vector for deformed beam-end

$\mathbf{i}_k$ Nodal base vector for the base vector i_i^0

$\mathbf{I}_k$ Coordinate frame for base vector i_i^0

j Interaction cycle

K Stress intensity factor

$\mathbf{K}$ Tangential stiffness matrix / Stiffness matrix

$\mathbf{K}_E$ Load correction stiffness matrix

k Incremental load step / Stiffness in oscillation frequency

$\mathbf{k}_G$ Geometric stiffness matrix

k_j Wave number

$\mathbf{k}_M$ Material stiffness matrix

$\mathbf{K}_S$ Tangential structural stiffness matrix

L_0 Initial element length

L Deformed element length

$\mathbf{M}$ Mass matrix

M_A Bending moment from accidental loads

M_d Design bending moment

M_E Bending moment from environmental loads

M_F Bending moment from functional loads

M_y Bending moment in y-direction

M_z Bending moment in z-direction

M_θ Bending moment in θ-direction

m Mass of cylinder / Negative inverse slope of S-N curve

m_{ao} Added mass in still water

m_a Added mass in 2D

m^h Added mass pr. unit length

$\mathbf{m}^h$ Added mass matrix

m_p Mass of pipe pr. unit length

m^s Structural mass pr. unit length

$\mathbf{m}^s$ Structural mass matrix

N Interpolation functions

N Axial force / Number of cycles to failure / Number of tensioners / Active translational DOFs

N_{xx} Axial force

n Number of failed tensioners

p Load intensity vector

P_e External hydrostatic pressure

P_i Internal hydrostatic pressure/probability for a sea state

Q Excitation load

R_d Design resistance

$\mathbf{R}^D$ Damping force vector

$\mathbf{R}^E$ External reaction force vector

$\mathbf{R}^I$ Inertia force vector

$\mathbf{R}^K$ Force imbalance vector

$\mathbf{R}^S$ Internal reaction force vector

$\mathbf{r}$ Displacement vector

$\dot{\mathbf{r}}$ Velocity vector

$\ddot{\mathbf{r}}$ Acceleration vector

S_d Design load effect

$\mathbf{S}$ Piola-Kirchhoff stress tensor in original coordinate frame

$\tilde{\mathbf{S}}$ Piola-Kirchhoff stress tensor in co-rotated coordinate frame

$\mathbf{S}^e$ External nodal load vector for an element

St Strouhals number

$\mathbf{S}_{int}$ Internal reaction force vector

$S(w)$ Wave spectrum

$S_\eta(w)$ Wave spectrum

T Effective tension

$\mathbf{T}$ Rotation matrix

$\bar{\mathbf{T}}$ Rotation matrix

$\bar{\mathbf{T}}^0$ Rotation matrix

$\tilde{\mathbf{T}}$ Rotation matrix

T_e Effective tension

T_{eA} Effective tension from accidental loads

T_{ed} Design effective tension

T_{eE} Effective tension from environmental loads

T_{eF} Effective tension from functional loads

T_{min} Minimum top tension

T_p Tension in pipe wall/peak period

T_{real} Axial pipe wall tension

T_{SRmin} Minimum slip ring tension

T_w Axial wall force

t_0 Surface traction in original coordinate frame vector

t Time/plate thickness

t_{ref} Reference pipe wall thickness

U Flow speed

U^c Current velocity component in Morsion equation

$\mathbf{u}$ Displacement vector

$\dot{\mathbf{u}}$ Velocity vector

$\ddot{\mathbf{u}}$ Acceleration vector

u^I Velocity component in Morsion equation

V_0 Volume in original coordinate frame

$\mathbf{v}$ Displacement vector

v_i Internal fluid velocity

w Effective weight

$\mathbf{X}$ Position vector

$\tilde{\mathbf{X}}$ Position vector in co-rotated ghost reference

x Position of particle at time t

y Displacement amplitudes

Greek symbols

α_1 Mass proportional damping coefficient

α_2 Stiffness proportional damping coefficient

β Numerical integration type

γ Artificial damping / Peakedness parameter

γ_A Accidental load effect factor

γ_E Environmental load effect factor

γ_F Functional load effect factor

Δ Finite small increment

δ Virtual quantities

ϵ Tolerance requirement for convergence

ϵ_j Phase angle in wave elevation

θ Rotational motion

λ_i Modal damping

ξ Natural coordinate ($\xi = \frac{x}{L}$)

ρ Density

σ Variance of Gaussian distribution / Stress in S-N curves

σ_{as} Resultant axial stress

τ Time

ϕ Eigenvector

Ψ Wave elevation

ω Eigenfrequency

ω_j Circular frequency in surface elevation

ω_p Circular peak frequency in surface elevation curve

Chapter 1

Introduction

1.1 Background

Drilling risers provide a link between the well and the rig, and is therefore a safety critical systems during offshore operations. The drilling operations are usually conducted up to 2000m water depths, but the demand for deeper operations are increasing.

Today there are no standard for the direct assessment of marine riser joints. However, there are several standards of marine riser integrity, such as API, ISO, DNV and NORSOK. New standards are therefore under development at TH HILL, a Bureau Veritas enterprise in Texas (Toderan, 2015). The work of this thesis focuses on parts of the development work, more specifically creation of a methodology for the mechanical assessment of marine riser joints, with respect to strength and fatigue.

The geometry of the model is simplified so that it can easily be changed for different riser designs. One case study has been investigated in the global load analysis, fatigue analysis and vortex-induced vibration (VIV) analysis. The geometry is based on information from technical standards and existing technology. The input data have been discussed with different teams from Bureau Veritas. Based on these discussions, a number of sensitivity studies and investigations have been conducted.

1.2 Literature review

As exploration moves into deeper water depths the importance of designing a safe marine drilling riser system becomes vital. Several articles regarding dynamic and fatigue analysis methodologies of risers have been published over the years, but as the article *The Complexities of Fatigue Analysis for Deepwater Risers* states, there is a need for finding analysis methods which are not too simplified nor overly conservative (Campbell, 1999). Different areas cause uncertainties, and are often the reason for why methodologies are less accurate. Vessel motion is one of the uncertainties, and papers such as *An Analysis of Marine Risers for Deep Water* looks particularly into the effect from vessel motions for riser in different water depths. The dynamic behavior due to vessel response was found to be significantly affected by the riser length (Burke, 1973). These findings were supported in the article *Random Wave and Vessel Motion Effects on Drilling Riser Dynamics*, where the effect of random waves and vessel motions were found to be a significant design factor (Sexton & Agbezuge, 1976).

Other uncertainties in the development of methodologies are vortex-induced vibrations, and several approaches have been presented for how to calculate the response correct. The paper *Vortex-Induced Vibration of Deepwater Risers* stresses the importance of finding a correct calculation method for deepwater risers. The article focuses on important parameters to consider in the analysis approach, and the effect of suppression devices and riser interference (Allen, 1998). Calculations including vortex-vibrations are often a costly analysis, and different articles have been published of how the cost can be reduced, but still give an acceptable accuracy. The paper *Dynamic Analysis as an Aid to the Design of Marine Risers* aim towards an economically approach for calculating the riser response due to waves and current. Many riser models have been designed in the time domain, often because it is the preferred calculation method or that it is the necessary method for solving the problem. The frequency domain method has often been a less desirable method due to linearization of the drag force, but as the article states, there are still great uncertainties in the representation of waves and current that doesn't often justify the costly time domain analysis (Young et al., 1978). This is supported in the article *Dynamic Behavior of a Top Tensioned Riser in Frequency and Time Domain*, where a comparison of deepwater risers, solved in frequency domain and time domain, is presented. The article concludes

however, that a frequency response method should be applied in the first phases of the design process, but a time domain analysis should be conducted in later phases, in order to correctly represent the nonlinearities (Morooka et al., 2006). Other articles, with focus on developing approaches with concern of vessel motions and current, are *Nonlinear Response Analysis of Marine Risers*, which calculates the response in frequency domain (Ahmad & Datta, 1992), and *Dynamic Response of Marine Risers*, which calculates the response in time domain (Ahmad & Datta, 1989).

Fatigue analysis methods for drilling riser is also a debated topic, and articles such as *Dynamic Response and Fatigue Damage Analysis for Drilling Riser*, focuses on developing methods for properly calculating fatigue damage. A time domain analysis has been used in the approach, in addition to rainflow counting, S-N curve and Miner-Palmgren rule (Chen et al., 2012). Solution in time domain and the choice of cycle counting method, are supported by the paper *Methodology for Time Domain Fatigue Life Assessment of Risers and Umbilicals*. The paper emphasizes the need for describing nonlinearities from waves and vessel motions accurately, and states the importance of selecting the correct simulation length, in order to calculate the correct fatigue response. The methodology represented in this paper was used in the updated version of DNV-RP-F204 Riser Fatigue 2010 (Steinkjer et al., 2010).

The need for new revisions was recognized by the DeepStar program in 1999. The recommended practice for design, selection, operation and maintenance of marine drilling riser systems (API RP 16Q) was developed in 1993, and since then new findings have led to improvements of the analysis methodologies presented in the recommended practice. A Joint Industry Project between API and MCS International led to a revision of the standard, focusing on subjects such as the methodology related to coupled analysis and drift-off (Kavanagh et al., 2002).

Based on the existing literature, little information have been found regarding the mechanical assessment of riser joints. As drilling operations exceeds into deeper depths, the need for standards concerning these components is recognized. The development work presented in this thesis can hopefully contribute to the development of a standard for riser joints.

1.3 Objective

The objective of this thesis is to create a method for the assessment of marine riser joints. This includes creating a simplified model of the riser, that can easily be modified for different riser configurations. Rules and standards, in addition to the existing technology, should be carried out to give the background information for selecting the cases to be investigated. A literature study and familiarization of the software tools, should be carried out to obtain knowledge about the topic. A global load analysis, fatigue analysis and a VIV analysis should be performed for one case-study. Sensitivity studies and investigations regarding the input data in the different analysis, should be carried out in order to validate the methodology.

1.4 Scope and limitations

The scope is to create a methodology for the mechanical assessment of marine riser joints, based on strength and fatigue. Information on existing technology and rules and standards, should be presented in order to create cases which can be used to validate the methodology. The methodology will hopefully contribute to the development of a new standard for riser joints.

The master thesis work has been performed with limited time. In the beginning of the thesis, a workplan was created by Catalin Toderan, given in appendix E. Limited resources were made available during the stay at Bureau Veritas, such as lack of software licences. The work in phase 4 and parts of phase 3 and 5 in the workplan, were therefore reduced after agreement with Catalin Toderan and Svein Sævik. This includes point 4 in the scope of work in *BV proposal N° DTO4 - 6m Thesis: Assessment of Marine Riser Joint during Offshore Drilling Operation, dated 25/06/2015* (Toderan, 2015). The focus has been to develop the methodology for one combination of wave, wind and current direction, in a global load analysis, fatigue analysis and VIV analysis.

1.5 Thesis structure

1. **Introduction** gives information about the background, literature review, objective, scope and limitations.
2. **The marine drilling riser** gives information about different drilling platforms, drilling riser system, drilling operation and technology in the industry.
3. **Theory** compares the fundamental theory behind SIMA/RIFLEX and Flexcom, and presents the theory behind the different analysis
4. **Rules and standards** presents the theory from rules and standards for the drilling riser and its components, in addition to the methodology for the different analysis
5. **Method of analysis** presents the methodology of the mechanical assessment of riser joints.
6. **Results and discussion** presents the results and uncertainties from the analysis.
7. **Conclusion** summarizes the conclusion from the methodology and results.
8. **Further work** gives recommendations and suggestions for future studies.

Chapter 2

The marine drilling riser

In order to find potential hydrocarbon reservoirs, seismic surveys are used. The surveys give information through sound waves, which are reflected by the rock formations, and sent to the hydrophones. If the operation is successful, a series of tests will be conducted in order to map the location and the properties of the reservoir. If the reservoir gives the desired outcome, the drilling operation of the well can begin (Mather, 2011).

The well is tested after the drilling operation is conducted. Completing a well is expensive and it is therefore important to know how much the well will produce. After testing, the well is either plugged and becomes a dry hole, or is completed. If the well is completed a thin steel pipe is inserted into the hole. The pipe consist of casings of same size, which are attached together and create a long casing string. A drillstring with a bit at the end is run into the well and cuts the hole and the casing string is attached with cement. Drilling mud helps to smooth the hole and remove cuttings. The last phase is the workover phase, which includes solving problems related to the well and cleaning the well. When a well is killed a kill fluid is pumped into the well (Hyne, 2001).

2.1 Drilling platforms

The type of drilling platforms depend on different factors, such as the water-depth, location and environment. The exploration wells are usually drilled by semi-submersibles, drill ships or barges. Jack-up rigs, that are self-elevating, are also an option if the water depth is not too large. However, fixed platforms are most common for development wells. In general, offshore drilling platforms can be divided into three categories: fixed platforms, self-contained fixed platforms and mobile units.

The first category, fixed platforms, consist of piles that go into the seabed, and a drilling tender that is moored close to the platform. The tender is often a barge, which leaves after the drilling operation is done. These types of platforms are usually used for development wells, and are less common today. The second category, self-contained fixed platforms, are either concrete gravity structures or tubular steel structures pinned by piles to the seabed. The gravity-based structures can stand on the seabed freely, because of their large mass. The third category, mobile units, are designed either to float or to rest on the seabed. The ones that float are drill ships, barges and semi-submersibles. The ones that rest on the seabed are jack-ups and semi-submersibles (Maclachlan, 1987).

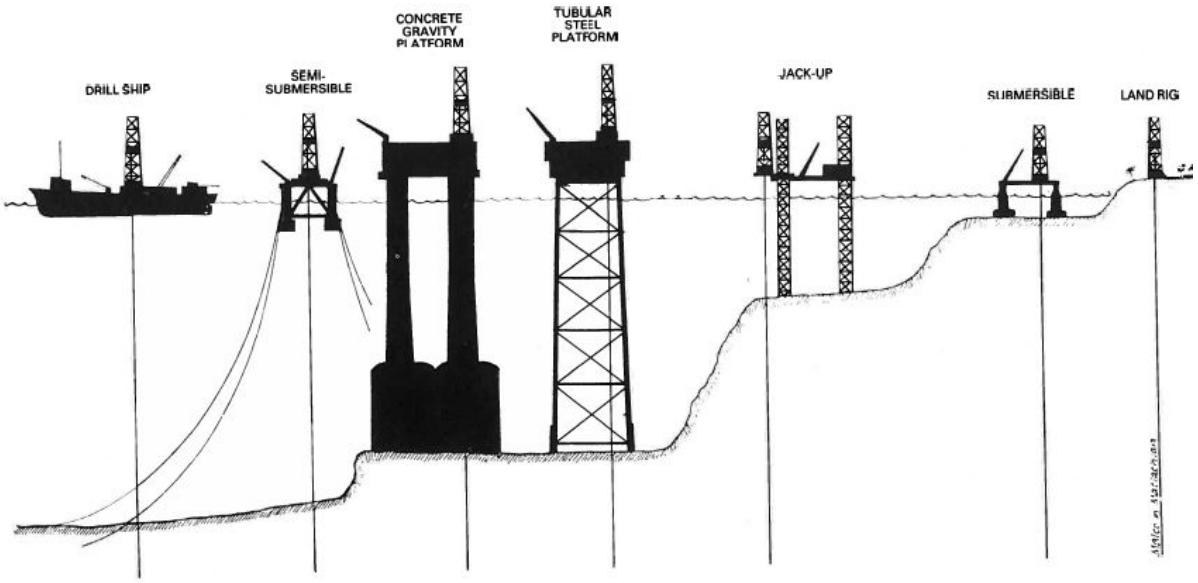

Figure 2.1: Offshore drilling platform types (Maclachlan, 1987)

2.2 Drilling riser system

The marine riser system has according to American Petroleum Institute (API) four main functions.

- Ensure that the well and drilling vessel transport fluid between each other
- Give support of the choke, auxiliary and kill lines
- Lead different tools into the well
- Assist the Blow out preventer (BOP) stack by acting as a retrieving and running string

We can divide the system into three parts, an upper part, the riser and a lower stack. The information in this chapter is taken from the standard API-RP-16Q (API, 2010a).

Figure 2.2 shows a drawing of the marine riser system.

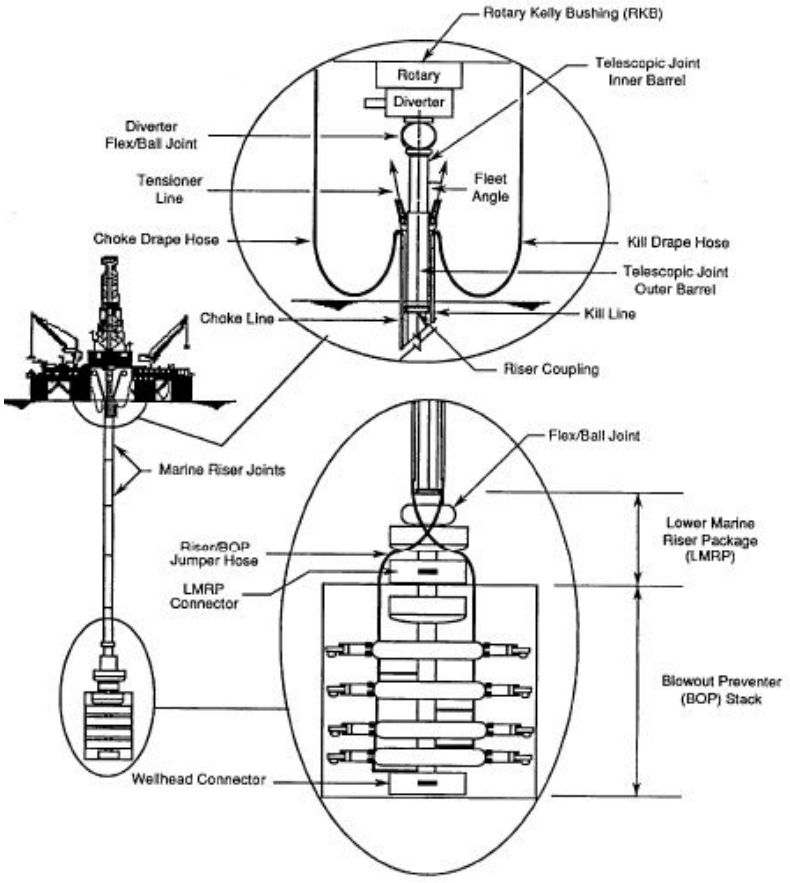

Figure 2.2: The marine riser system (API, 2010a)

2.2.1 Upper part

Tensioner system

The purpose of the tensioner system is to control the stress and the displacement of the marine drilling riser, by applying a vertical force through tensioner units. The tensioner units, which are placed near the drillfloor on the drilling vessel, ensure constant axial tension, when the vessel experience environmental loads. The constant tension is ensured by attaching one end of the tensioner line to the tensioner, and the other to the tensioner ring near the outer barrel of the telescopic joint. The line is usually built up by four lines, and the piston stroke is therefore $\frac{1}{4}$ of the heave motion of the vessel. The tensioner system is designed according to different criteria, to ensure an effective system. The criteria are defined with respect to the dynamic tension limit (DTL), friction and inertia losses, fluid and air requirements, wireline life, accumulator and air pressure vessels. Redundancy is also important to consider when designing the system. If one of the tensioner units is in maintenance, the tensioner system must still ensure a constant axial stress in order to prevent buckling (API, 2010a).

Diverter system

The purpose of the diverter system is to direct flow from the well aboard the rig. Blowouts are usually prevented by the BOP, but the BOP is not installed when the drilling process is in the beginning phase (API, 2010a). The BOP's main function is to seal the drill pipe when it is placed in the drill hole, or when the hole is open. It is arranged in a vertical stack above the wellhead, and therefore often referred to as the BOP stack (Maclachlan, 1987). It is therefore important to have the diverter system if the well flows. The diverter system is installed below the rotary table (API, 2010a). The rotary table is a housing where all of the casings and tools are run through, and where the drill string and kelly are operated. The rotary table transmits the torque to the kelly, which is connected to the drill string. The kelly is formed like a steel pipe and is able move the drill bit vertically (Maclachlan, 1987).

Below the diverter is the flex/ball joint, which represent the first part of the marine riser system. The diverter system may also consist of a diverter stack, which is installed on the wellhead. The function of this is to divert subsea (API, 2010a).

2.2.2 The riser

Telescopic/slip joint

The purpose of the telescopic joint is to prevent damages to the riser, when the vessel experience heave motions. As mention in the tensioner system, the outer barrel of the joint supports the tensioner line. It is connected to the riser, while the inner barrel is connected to the vessel. The tensioner ring is an important component of the telescopic joint. The function of the ring is to transfer loads that support the riser. The telescopic joint is designed with respect to different criteria. These criteria involve strength, stroke length, storage, tensioner ring, auxiliary lines, packing element and handling of the joint (API, 2010a).

Riser joints

The riser joint is a high strength pipe with couplings welded to each end. The upper end of the joint support the loads, when the BOP and the riser is removed from the spider (API, 2010a). The spider is a steel frame placed around the rotary opening (Maclachlan, 1987). The riser couplings come in four different designs; breech-block, flanged, threaded union and dog type. They usually support the auxiliary, choke and kill lines and the buoyancy equipment. The riser joints are the main components of the marine riser system, and contributes to the four main functions of the system (API, 2010a).

Choke/kill and auxiliary lines

The choke/kill and auxiliary lines are attached to the riser main tube by brackets. The lines are used when the BOP stack is closed and fluid must be carried in a controlled manner from the wellbore to the surface. The design is developed based on different criteria, such as type of fluid in the line, operation pressure, couplings, internal diameter, orientation, support and corrosion. The choke and kill lines can also be flexible lines. These ensure that the flex/ball joints and the telescopic joints can experience movement. They are typically designed either as flow loops with threaded, clamped or flanged end fittings, steel reinforced hoses or as flexible pipes (API, 2010a).

Riser main tube

The main tube of the riser must be able to withstand loads from the environment, motions from the vessel, weight and tension applied to the riser. The strength to resist these loads are determined by the diameter, thickness and material characteristics. They are designed based on criteria such as corrosion, fatigue, bend radius, length, pressure and collapse (API, 2010a).

Pup joints

Pup joints are joints with a smaller length. The purpose of this joint is to ensure that the required length of the string is covered (Maclachlan, 1987).

Running equipment

The running equipment contributes with moving the riser and BOP stack vertically up and down. The operation is supported by the riser spider at the drill floor. The support from the spider helps to reduce impact loads and bending moments. The running equipment is designed with respect to the max static load capacity, bending loads and impact loads during operation, and loads from the environment and vessel motion (API, 2010a).

Buoyancy equipment

Buoyancy equipment is attached the riser in order to reduce the submerged weight, and by that reduce the requirements regarding top tension. The equipment can be foam modules made of composites or air chambers. The foam modules are installed around the riser joints, while the air chambers are installed to the riser couplings (API, 2010a).

2.2.3 Lower stack

Lower marine riser package

The lower marine riser package (LMRP) connects the riser to the BOP stack and ensure hydraulic control of the stack. The package consist of a flex ball joint, subsea control pods, hydraulic connector, a riser adapter and sometimes annular BOPs. The design is based on several criteria such as height, weight, loads, pressure, well control, water depth, running/retrieving the control pods as well as emergency recovery (API, 2010a).

Flex and ball joint

Flex joints reduce the bending moment of the riser, by providing flexibility to create angles between the BOP stack and the riser. They can also contribute with reducing stress at the lower part of the telescopic joint. Flex joints can also be part of the diverter system, where they provide flexibility when the rig experience motions. Ball joints are used to seal drilling fluids, and have less effective rotational stiffness, compared to flex joints. The design of these two types of joints are based on criteria such as pressure, angular rotation, tensile loads and there location in the system (API, 2010a).

The wellhead

The wellhead consist of a casinghead and a tubing head. The casinghead is at the bottom, and the tubing head is on top of the casinghead. From the casinghead, a string casing is attached and helps to release pressure by a gas outlet. The conductor pipe is attached to the wellhead, and on top of the casing and tubing, the wellhead equipment is attached. The equipment consist of the tubinghead, casinghead, christmas tree, pressure gauges and stuffing box (Hyne, 2001). A drawing of the well and the christmas tree is shown in figure 2.3 and 2.4.

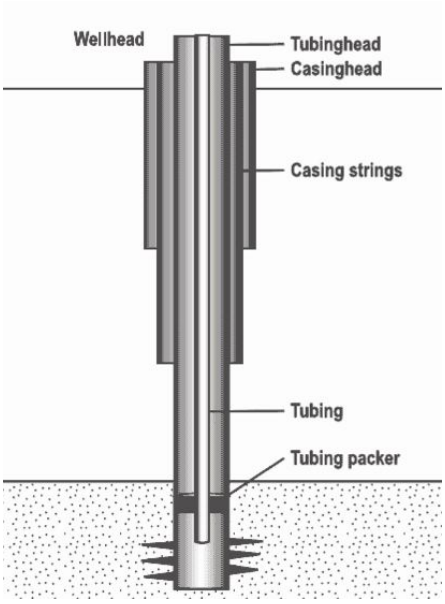

Figure 2.3: The well (Hyne, 2001)

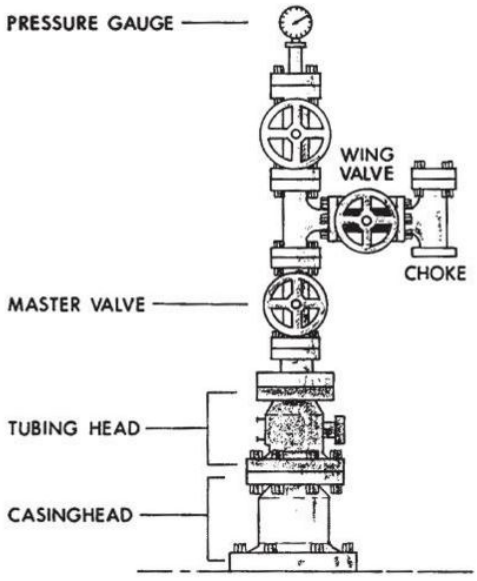

Figure 2.4: Christmas tree (Hyne, 2001)

2.3 Drilling operation

The drilling operation is different from rig to rig due to factors such as water depth, rigtype and standard practice, however the main features of the operation is given below (Maclachlan, 1987).

Move rig, run anchors and prepare rig

First, the rig must be moved to its location, anchors must be run and the rig must be prepared for drilling. The path for the drillbit is restricted from deviating more than 20 m from the target location. A temporary guide base (TGB) is installed on the seabed with four attached guidelines.

Drill 36" hole and run 30" casing

A hole opener, a 36" diameter bit, is run to the TGB to drill a hole 16' below seabed. The hole is filled with seawater and bentonite, to prevent it from collapsing. The hole opener is pulled back and the outer conductor, 30" casing, is run into the hole and fixed with cement. A permanent guide base (PGB) is attached to the outer conductor to ensure a safe landing of the BOP .

Drill 26" hole and run 20" casing

A 26" drilling bit is run down to the PGB and drills a vertical hole to 1500' .The hole is filled with seawater and bentonite in order to prevent sloughing. The bit is then pulled back to the rig and the inner conductor is run into the hole. The 20" conductor is also fixed with cement.

Run 18 $\frac{3}{4}$" BOP stack and marine riser

The wellhead is then attached to the casing with internal diameter of 18$\frac{3}{4}$", and the BOP stack and the marine riser are installed.

Drill 17 $\frac{1}{2}$" hole and run 13 $\frac{3}{8}$" casing

A drill bit with diameter 17 $\frac{1}{2}$" drills a hole and a 13 $\frac{3}{8}$" surface string casing is run down to the hole and fixed with cement. A water base mud is used for this part of the operation.

Drill 12 $\frac{1}{4}$" and run 9 $\frac{5}{8}$"

A new drill bit with diameter 12 $\frac{1}{4}$" drills a hole and a 9 $\frac{5}{8}$" casing is run and fixed with cement.

Drill 8 $\frac{1}{2}$" and run 7"

A 8 $\frac{1}{2}$" bit drills the last part of the total depth. The water base mud is now replaced with an oil base mud. A 7" liner is run and fixed with cement (Maclachlan, 1987).

2.4 Technology in the industry

An extensive internet search has been performed in order to find how different companies design and manufacture the riser and its components. As the purpose of this thesis is to define a methodology, it is important that the method can be applied to different configurations/designs of risers. The geometry of the riser have been simplified, but a few important components have been considered. These are the riser joints and the connections, the buoyancy modules and the lower flex joint. Case-studies for validation of the methodology, can be established based on the information given in this chapter.

2.4.1 Connections

The important information regarding the connections are the type of the connection, the load rating and the geometric properties. The different connections presented below are designed/manufactured by Dril-quip, Oil States Industries, Claxton and GE Oil & Gas.

Figure 2.5: FRC (Dril-Quip, 2014)

The FRC riser connector is a design by dril-quip, and is a flat-faced flange connection with 6-8 bolt configuration, as shown in figure 2.5. The connection is flange in order to reduce the loads on the bolts, and the configuration of the bolts makes exploratory drilling or high pressure drilling for TLP and Spar convenient. The FRC connection complies with API 16R and ISO-9001 and can be designed with different load and pressure capacities. In addition, due to tensile load sharing, the thickness of the pipe can be reduced, which reduces the weight of the riser (Dril-Quip, 2014).

Vetcogray has three different designs of connectors, the MR-6E riser, MR-6H SE riser and the HMF. The MR-6E Riser, shown in figure 2.6, is a dog style connection. Its load rating is classified after API 16R class E, and is rated for 2 million pound with a make-up torque equal to 950 foot-pound. The outer diameter, without buoyancy material, is 41.125 inches and inner diameter 19.75 inches. The length is 23.125 inches and the weight is 2510 pound. The MR-6H SE Riser,

shown in figure 2.7, has an external surface of pin and box, and is rated for 3.5 million pound after API class H. It is an automated make-up connection, with capability of higher pressure conditions by incorporation of a metal seal. The HMF riser, shown in figure 2.8, has a good design for deep water conditions and for current water depth for 10011 feet in the gulf of Mexico (GoM). The connector has pin/box flanges, and complies with API 16R, class D, E, F, G, H, J. The fatigue life of the coupling is extended by ensuring that the bolts are preloaded over the rated coupling load before locking (GE Oil & Gas, 2008).

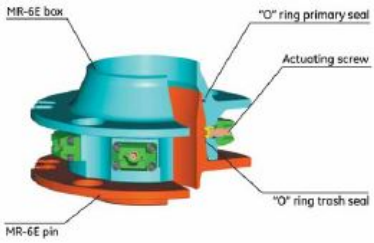

Figure 2.6: MR-6E (GE Oil & Gas, 2008)

Figure 2.7: MR-6H SE (GE Oil & Gas, 2008)

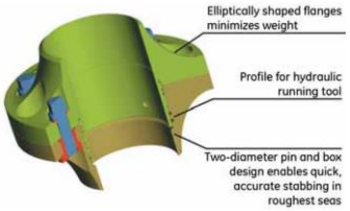

Figure 2.8: HMF (GE Oil & Gas, 2008)

Oil States Industries have in total six different design of connectors for semi-submersibles/drillships and jack-ups. However, the Merlin connector, shown in figure 2.9, is the only connector suited for jack-ups. The connector has great fatigue characteristics and is used for high pressure drilling (Oil States Industries, 2016b). For semi-submersibles the OR-21-, OR-6-, OR-F, OMR-M- or the OR-6C connector is proposed. The OR-21 connector, shown in figure 2.10, is design with lock-ring and is a full preloaded connection. The connection is designed to qualify the API 16R recommended practices. The OR-6 connector, shown in figure 2.11, is also a fully preloaded dig type connector. The connector can be fitted with buoyancy (Oil States Industries, 2016c).

Figure 2.9: Merlin (Oil States Industries, 2016b)

Figure 2.10: OR-21(Oil States Industries, 2016c)

Figure 2.11: OR-6(Oil States Industries, 2016c)

The OMR-M connector, shown in figure 2.12, is a non-integral Merlin connector. It has great fatigue characteristics and can be applied for water depths of 10000 feet (Oil States Industries, 2016c). The OR-6C connector, shown in figure 2.13, is a fully preloaded dog type connector. The connector have load rating 1.25M pound after API 16R (Oil States Industries, 2012a). The OR-F connector, shown in figure 2.14, have tensile load rating 2.5M pound after API 16R. The connector is flanged and is a fully preloaded connection (Oil States Industries, 2012b).

Figure 2.12: OMR-M (Oil States Industries, 2016c)

Figure 2.13: OR-6C (Oil States Industries, 2012a)

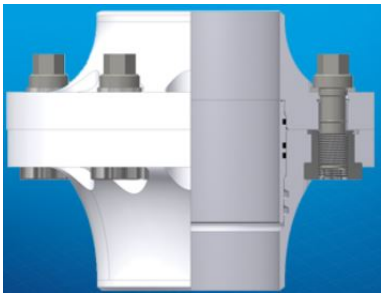

Figure 2.14: OR-F (Oil States Industries, 2012b)

Claxton have three types of connections, the SRP Shrink-Fit high performance flange, the API custom/SRP high performance flange and the Merlin quick connection from Oilstates, displayed in figure 2.9. The SRP Shrink-fit high performance flange, shown in figure 2.15, has operation pressure equal to 12200 pounds per square inch. The outer diameter is 24 inches and the inner diameter is 18.3/4 inches. The custom or SRP high performance flange, shown in figure 2.16, has operating pressure 5000 pounds per square inch. The outer diameter is also 24 inches, but the inner diameter is.1.1/2 inches. The Merlin quick connection from Oilstates, shown in figure 2.17, has operating pressure equal to 5000 found per square inch. The outer diameter is 24 inches and inner is 21 inches (Claxton, 2014a).

Figure 2.15: SRP Shrink-Fit (Claxton, 2014a)

Figure 2.16: Custom/SRP (Claxton, 2014a)

Figure 2.17: Merlin (Claxton, 2014a)

2.4.2 Joints

The important information regarding the joints are the length of the joint, the operating pressure and the geometric properties. The different joints presented below are designed/manufactured by Dril-quip, Oil States Industries, Claxton and GE Oil & Gas.

Dril-quip has designed a joint with six auxiliary lines attached to the riser. The joints are usually slick or buoyant joints, where the latter is manufactured by other companies. The buoyancy joints are designed to integrate with the slick joints created by Dril-quip (Dril-Quip, 2014).

Cameron has two different designs for the riser joints, the LoadKing riser and the RF riser. The LoadKing riser is designed for deep water, 7000 feet or more, and has tension ratings up to 4 MMlb. The RF riser is designed for mid water drilling, and has tension ratings up to 2 MMlb (Schlumberger, 2015).

Oil States Industries have designed two joints, the OR-F joint and the OR-6C joint. The OR-F joint is either slick a joint or buoyancy joint, of lengths between 5 feet and 90 feet, approved by API 16F (Oil States Industries, 2012b). The OR-6C joints have the same length as the OR-F,

and is a box up pin down connection. The joint can also be buoyant joint or a click joint, and is approved by API 16F (Oil States Industries, 2012a).

Claxton have several types of joints in different dimensions and operating pressures. All of the joints have flange type API. Three joints have the same minimal diameter of 13.5/8 inches, but different operating pressures and lengths. The largest operating pressure is equal to 15000 pound per square inch and is 20 feet long. Next in line is the joint with 10000 pounds per square inch and length equal to 275 feet. At last is the joint with the smallest operating pressure, 5000 pound per square inch, with length of 50 feet. Another type of joint, designed by Claxton, has diameter 20.3/4 inches. The joint is 55 feet long and has operating pressure equal to 3000 pound per square inch. In addition to the joints mentioned above, Claxton has designed two other joints with same minimal diameter of 21.1/4 inches. The operating pressures are 5000 pounds per square inch and 2000 pound per square inch, and the lengths are 33 feet and 135 feet respectively (Claxton, 2014b).

2.4.3 Buoyancy modules

The buoyancy modules are designed by several companies. However, the information regarding the density of the modules are often protected, and the information is therefore limited. Two of the largest companies designing buoyancy modules are Trelleborg and Balmoral Offshore Engineering, but both companies have limited information on their websites. Another company which provides design of buoyancy modules is Matrix Composites and Engineering. They company has restricted the information available on their website, but after a wider search more detailed information was found. Matrix Composites and Engineering have buoyancy modules which are either in two or in three parts, depending on how the line assemblies are managed. The modules consist of a core and a skin. The core is made of composites syntactic foam that is vacuum processed and moulded, and the skin is FRP reinforced. Matrix Composites and Engineering divide the densities in four different categories of densities, premium, ultra-light, hybrid and standard. The first category is the lightest density and the last is the most heavy density. For the premium density, the lift efficiency is maximized by reducing the cross-section area of the buoyancy. The Ultra-light density has properties which helps reducing the tensioner capacity

and improves the lift per riser joint. These qualities are achieved by decreasing the weight of the riser when it is submerged, and by reducing the cross-section area of the buoyancy respectively. As an example, for a 75 inch joints of total height of 3048 m/1000 feet the outer diameter is reduced by 4 inches and the weight by 4884 kg/10745 pounds. The Hybrid density is more economical compared to the Premium and Ultra-light densities, and the Standard density is used when there are no specific requirements concerning the operational drag loads, the dry weight or the dimensions. The densities are given in table 2.1 for selected depths (Matrix Composites and Engineering, 2014).

Depth [m]	Premium [kg/m^3]	Ultra-light[kg/m^3]	Hybrid[kg/m^3]	Standard[kg/m^3]
610		324 (min)		346 (min)
1219			396 (min)	
1829		428	461	488
2134		449	484	516
3353	523 (min)			
3658			601 (max)	649 (max)
4267	569 (max)	591 (max)		

Table 2.1: Buoyancy module densities

2.4.4 Lower flex joint

The important information regarding the flex joints are the angular deflection and the working pressure. The different flex joints presented below are designed by Dril-quip, Cameron, GE Oil & Gas and Oil States Industries, and placed at the lower part of the riser, above the LMRP.

The lower flex joint designed by Dril-quip has angular deflection up to ten degrees, and are used in water depths up to 12000 feet (Dril-Quip, 2014). Cameron have designed a flex joint with same angular deflection and water depth. The joint has a working pressure up to 6000 pound per square inch (Schlumberger, 2015). The flex joint designed by GE Oil & Gas has same angular deflection, but an internal pressure of 3000 pound per square inch. The tensile load capacity is up to 2 million pound (GE Oil & Gas, 2008). Oil States Industries has also same angular deflection, but a working pressure up to 6000 pound per square inch. The maximum water depth is 12000 feet and the max axial tension is 3500 kilo pounds (Oil States Industries, 2016a).

Chapter 3

Theory

There are several types of software that can be used to analyze drilling risers. Two of them are presented in this chapter, RIFLEX and Flexcom. RIFLEX was used in the project thesis, while Flexcom in the master thesis. A focus has been given to the theory based on the RIFLEX program, but a comparison to the Flexcom software has been given for the fundamental theory in 3.1, static analysis in 3.2.1, eigenvalue analysis in 3.2.2, and dynamic analysis in 3.2.3.

3.1 Fundemental theory

RIFLEX uses two reference systems for describing the motion of the particle, the total Lagrangian formulation and the Co-rotated ghost reference. The first formulation is used for bar elements, and the second for beam elements.

For a general reference system, the position of a particle at time t, is given by equation 3.1, where X is the position vector and u is the displacement vector.

$$x(\mathbf{X}, t) = \mathbf{X} + \mathbf{u} \tag{3.1}$$

This is implemented into finite element formulations with equation 3.2. The notations are the same, expect the displacement vector is now denoted with v.

$$x = \mathbf{X} + \mathbf{v} \tag{3.2}$$

Each node of the structure has three translations and three rotations. The movement of the node is followed by a base vectors $\bar{\mathbf{i}}_i$, which is parallel to the global base vectors $\mathbf{I}_i$, as shown in figure 3.1.

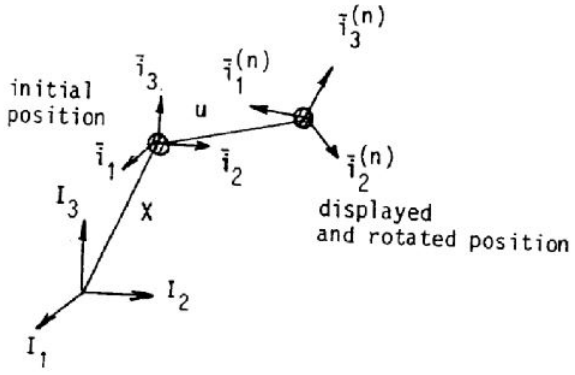

Figure 3.1: Translation and rotation of nodal point (MARINTEK, 2015a)

The orientation of the nodal point is given in equation 3.3, where $\bar{\mathbf{T}}_{ij}$ is the rotation matrix.

$$\bar{\mathbf{i}}_i^{(n)} = \bar{\mathbf{T}}_{ij}^{(n)} \mathbf{I}_j \tag{3.3}$$

The orientation of the nodal point at configuration C_{n+1} from a point at C_n, is found by updating the transformation matrix. This is shown with equation 3.4. I_j is the original coordinate frame vector.

$$\bar{\mathbf{i}}_i^n (n+1) = \bar{\mathbf{T}}_{ij}^{n+1} \mathbf{I}_j \tag{3.4}$$

For small increments, equation 3.4 can be expressed with equation 3.5, where the rotation matrix is expressed as $\tilde{\mathbf{T}}_{kj}$.

$$\bar{\mathbf{i}}_i^n(n+1) = \bar{\mathbf{T}}_{ij}^{n+1}\mathbf{I}_j = \bar{\mathbf{T}}_{ik}^n\tilde{\mathbf{T}}_{kj}\mathbf{I}_j \tag{3.5}$$

The nodal displacement in the C_{0n} configuration is defined with two new coordinate systems, as shown in figure 3.2.

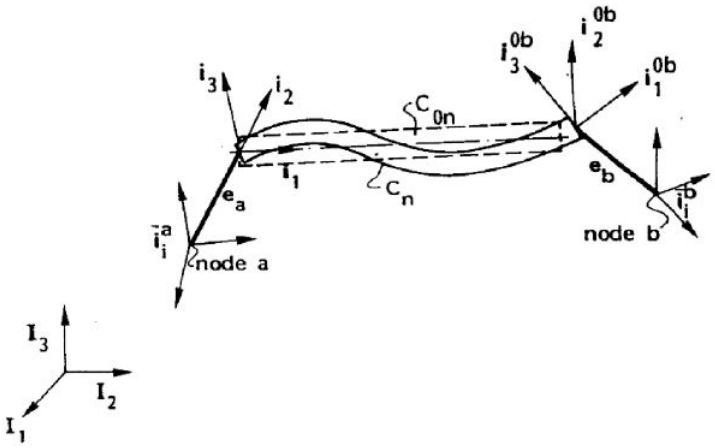

Figure 3.2: Displacement for beam element(MARINTEK, 2015a)

The base vectors, $\mathbf{i}_i$, represent the transformation between the global system and C_{0n} configuration, and is given in equation 3.6.

$$\mathbf{i}_i = \mathbf{T}_{ij}\mathbf{I}_j \tag{3.6}$$

The base vectors $\mathbf{i}_i^0$, follows the end of the beam as it deforms, as shown in equation 3.7. The equation is obtained by inverting equation 3.6 (MARINTEK, 2015a).

$$\mathbf{i}_i^0 = \bar{\mathbf{T}}_{ik}^0\mathbf{I}_k = \bar{\mathbf{T}}_{ij}^0\mathbf{T}_{kj}\mathbf{i}_k \tag{3.7}$$

3.1.1 Bar element

The motion of material particles have position vectors referring to a fixed coordinate frame with base vectors $\mathbf{I}_i$ in the initial configuration C_0. The strains in the deformed configuration, C_n, and incremental configuration, C_{n+1}, are referred to the initial configuration. This is the total Langrangian formulation.

Motion

The motion of the material particle in the total Lagrangian formulation is shown in figure 3.3.

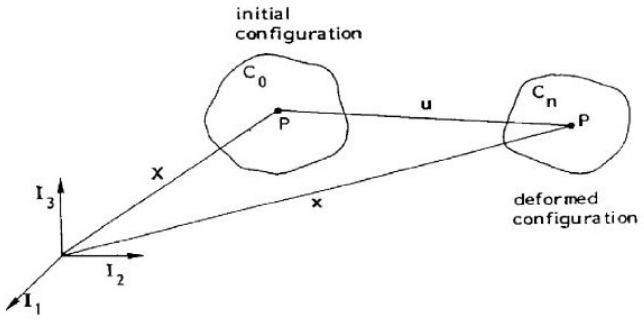

Figure 3.3: Total Lagrangian formulation(MARINTEK, 2015a)

Strain

The strains for the Lagrangian formulation is defined by Green strains, where the differences in length for segment PQ shown in figure 3.5, is given in equation 3.8.

$$dS_n^2 - dS_0^2 = 2d\mathbf{X} \cdot \mathbf{E} \cdot d\mathbf{X} \tag{3.8}$$

The strain tensor is given in equation 3.9, where $\mathbf{I}_i$ is the original base vector and $\mathbf{I}_j$ is the original coordinate frame.

$$\mathbf{E} = E_{ij}\mathbf{I}_i\mathbf{I}_j \tag{3.9}$$

The strain component is given in equation 3.10.

$$E_{ij} = \frac{1}{2}\left(\frac{\partial \mathbf{u}_i}{\partial \mathbf{X}_j} + \frac{\partial \mathbf{u}_j}{\partial \mathbf{X}_i} + \frac{\partial \mathbf{u}_m}{\partial \mathbf{X}_i}\frac{\partial \mathbf{u}_m}{\partial \mathbf{X}_j}\right) \tag{3.10}$$

Stress

The stress tensor is given by 2nd Piola-Kirchhoff stress, and is shown in equation 3.11.

$$\mathbf{S} = S_{ij}\mathbf{I}_i\mathbf{I}_j \tag{3.11}$$

Principle of virtual work

The Green strain and the Piola-Kirchhoff stress is used in virtual work equations which express dynamic equilibrium. Equation 3.12 express the virtual work, where A_0 is the surface and t_0 surface traction. V_0 is the volume and f_0 the body forces for initial configuration.

$$\int_{V_0} \mathbf{S} : \partial\mathbf{E} \cdot dV_0 = \int_{A_0} t_0 \cdot \partial\mathbf{u} \cdot dA_0 + \int_{V_0} f_0 \cdot \partial\mathbf{u} \cdot dV_0 \tag{3.12}$$

For non-linear problems linearization between C_n and C_{n+1} gives the incremental form of the equilibrium equation, shown in equation 3.13. The first term gives the geometric stiffness, and the second term material the stiffness.

$$\int_{V_0} (\mathbf{S} : \partial\Delta\mathbf{E} + \Delta\mathbf{S} : \partial\mathbf{E}) dV_0 = \int_{A_0} \Delta t_0 \cdot \partial\mathbf{u} \cdot dA_0 + \int_{V_0} \Delta f_0 \cdot \partial\mathbf{u} \cdot dV_0 \tag{3.13}$$

Dynamic equilibrium

The dynamic equilibrium equation is given in equation 3.14, where $\tilde{c}$ is the viscous damping density function and ρ is the mass density.

$$\int_{V_0} \mathbf{S} : \partial\mathbf{E} \cdot dV_0 + \int_{V_0} \rho_0 \cdot \ddot{\mathbf{u}} \cdot \partial\mathbf{u} \cdot dV_0 + \int_{V_0} \tilde{c} \cdot \dot{\mathbf{u}} \cdot \partial\mathbf{u} \cdot dV_0 = \int_{A_0} t_0 \cdot \partial\mathbf{u} \cdot dA_0 + \int_{V_0} f_0 \cdot \partial\mathbf{u} \cdot dV_0 \tag{3.14}$$

Incremental form in is shown in equation 3.15.

$$\int_{V_0} (\mathbf{S} : \partial\Delta\mathbf{E} + \Delta\mathbf{S} : \partial\mathbf{E}) dV_0 + \int_{V_0} \rho_0 \cdot \Delta\ddot{\mathbf{u}} \cdot \partial\mathbf{u} \cdot dV_0 + \int_{V_0} \tilde{c} \cdot \Delta\dot{\mathbf{u}} \cdot \partial\mathbf{u} \cdot dV_0 = \int_{A_0} \Delta t_0 \cdot \partial\mathbf{u} \cdot dA_0 + \int_{V_0} \Delta f_0 \cdot \partial\mathbf{u} \cdot dV_0 \tag{3.15}$$

The fundamental theory is now implemented into finite element formulations. The bar element has two nodes, with three degrees of freedom (DOF), as shown in figure 3.4.

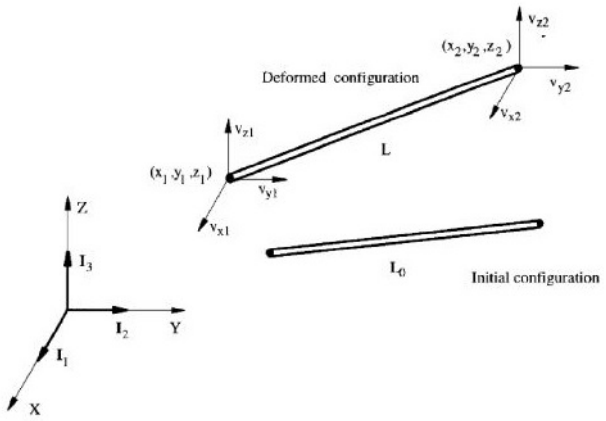

Figure 3.4: Bar element (MARINTEK, 2015a)

The strain is expressed with Green strain, stress with Piola-Kirchhoff stress and the displacement with interpolation functions. The interpolation functions are given in equation 3.16.

$$\mathbf{N} = \mathbf{N}_u = \mathbf{N}_v = [1-\xi, \xi] \tag{3.16}$$

From virtual work equation 3.12, the internal reaction force vector can be expressed with equation 3.17. L_0 is the initial stress free element length and N is the axial force.

$$\mathbf{S}_{int} = \begin{bmatrix} S_{x1} \\ S_{y1} \\ S_{z1} \\ S_{x2} \\ S_{y2} \\ S_{z2} \end{bmatrix} = \frac{N}{L_0} \begin{bmatrix} -\Delta x \\ -\Delta y \\ -\Delta z \\ \Delta x \\ \Delta y \\ \Delta z \end{bmatrix} \tag{3.17}$$

From the non-linear problems expressed in equation 3.13, the tangential stiffness relation can be expressed for an element, as shown in equation 3.18. k_G and k_M defines the geometric and material stiffness matrices respectively.

$$\Delta \mathbf{S}_{int} = (\mathbf{k}_G + \mathbf{k}_M)\Delta \mathbf{v} \tag{3.18}$$

The external nodal load vector in three DOFs can be expressed with the interpolation functions and intensity load vectors, as shown in equation 3.19.

$$\mathbf{S}^e = \begin{bmatrix} \mathbf{S}_u^e \\ \mathbf{S}_v^e \\ \mathbf{S}_w^e \end{bmatrix} = \int_L \mathbf{N}^T \mathbf{N} \begin{bmatrix} \mathbf{p}_x \\ \mathbf{p}_y \\ \mathbf{p}_z \end{bmatrix} dx \tag{3.19}$$

Both structural mass and added mass are considered in the mass matrix. Structural and added mass in three translations are given by equation 3.20 and 3.21 respectively.

$$\mathbf{m}^s = m^s \int_{L_0} \mathbf{N}^T \mathbf{N} dx \tag{3.20}$$

$$\mathbf{m}^h = \begin{bmatrix} \mathbf{m}_{uu}^h \\ \mathbf{m}_{vv}^h \\ \mathbf{m}_{ww}^h \end{bmatrix} = \int_{L_0} \mathbf{N}^T \begin{bmatrix} m_x^h \\ m_y^h \\ m_z^h \end{bmatrix} \mathbf{N} dx \tag{3.21}$$

The structural mass per unit length, m^s is equal in all directions, but the added mass per unit length, m^h will vary in the three directions.

Both structural and hydrodynamic damping are considered in the damping matrix. The structural damping is expressed with the Rayleigh damping model, as explained in 3.2.3. There are no hydrodynamic damping contributions in x-direction, but for y and z-direction the damping is expressed in equation 3.22 (MARINTEK, 2015a).

$$\mathbf{c} = \begin{bmatrix} \mathbf{c}_{uu} \\ \mathbf{c}_{vv} \\ \mathbf{c}_{ww} \end{bmatrix} = \int_{L_0} \begin{bmatrix} \mathbf{N}_u \\ \mathbf{N}_v \\ \mathbf{N}_w \end{bmatrix}^T \begin{bmatrix} 0 \\ c_y^h \\ c_z^h \end{bmatrix} \begin{bmatrix} \mathbf{N}_u \\ \mathbf{N}_v \\ \mathbf{N}_w \end{bmatrix} dx \tag{3.22}$$

3.1.2 Beam element

The motion of the particles are related to a local coordinate frame with base vectors, $\tilde{\mathbf{I}}_i$, that both rotates and translates around the average motion of the body. The base vectors come from the original base vectors $\mathbf{I}_i$, from the initial configuration C_0, that rotates along C_{0n}. By combining the motion of the local position vector and reference system, the total motion can be found. This is called the co-rotated ghost reference.

Motion

The motion of the material particle in the co-rotated ghost reference is shown in figure 3.5, where C_{0n} is the reference of the rotation center.

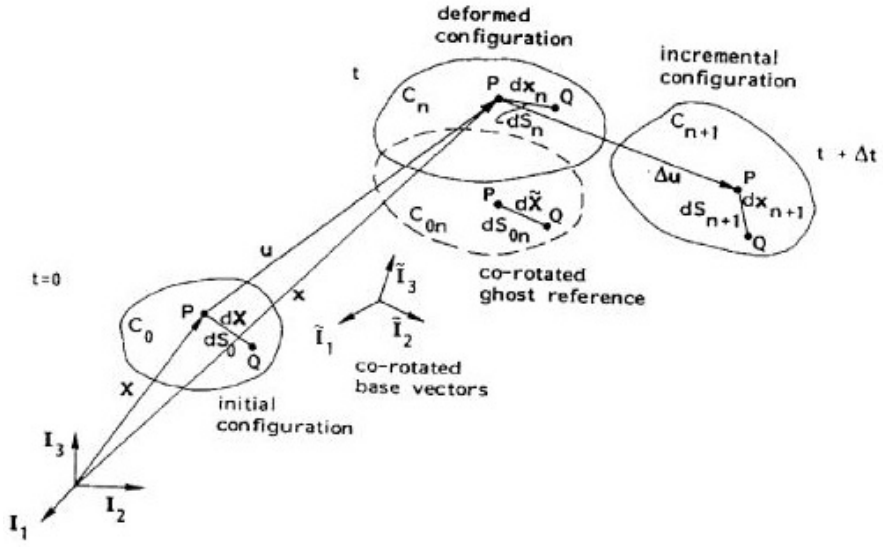

Figure 3.5: Co-rotated ghost reference (MARINTEK, 2015a)

Strain

The strains for the co-rotated ghost reference is given by Green strains, where the differences in length for segment PQ in figure 3.5, is given in equation 3.23.

$$dS_n^2 - dS_0^2 = 2d\tilde{\mathbf{X}} \cdot \tilde{\mathbf{E}} \cdot d\tilde{\mathbf{X}} \tag{3.23}$$

The strain tensor is given in equation 3.24, where $\tilde{\mathbf{I}}_i$ is the co-rotated base vector and $\tilde{\mathbf{I}}_j$ is the co-rotated coordinate frame.

$$\tilde{\mathbf{E}} = \tilde{E}_{ij}\tilde{\mathbf{I}}_i\tilde{\mathbf{I}}_j \tag{3.24}$$

Stress

The stress for the co-rotated ghost reference system is also given by 2nd Piola-Kirchhoff stress, and is shown in equation 3.25.

$$\tilde{\mathbf{S}} = \tilde{S}_{ij}\tilde{\mathbf{I}}_i\tilde{\mathbf{I}}_j \tag{3.25}$$

Principle of virtual work

The Green strain and the Piola-Kirchhoff stress can also for the beam element be used in virtual work equations. The equations will be the same as equation 3.12 and 3.13, but the E_{ij} will be $\tilde{E_{ij}}$ and the S_{ij} will be $\tilde{S_{ij}}$. Also, A_0, t_0, V_0 and f_0 will refer to the co-ghost reference.

Dynamic equilibrium

The dynamic equilibrium equation is also expressed in the same way as for the bar element shown in equation 3.14 and 3.15, however the same changes must be made, as explained in principle of virtual work in the paragraph above.

The fundamental theory is now implemented into finite element formulations. The beam element has three translations and three rotations for each node as shown in figure 3.6.

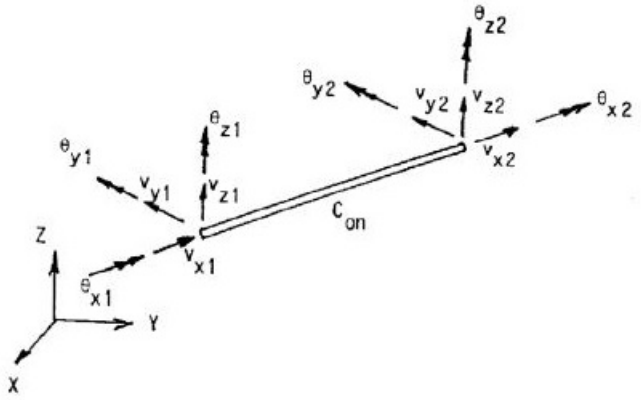

Figure 3.6: Beam element (MARINTEK, 2015a)

The beam element is based on small strains and Navier's hypothesis. Shear deformations are also neglected, as well as lateral contraction and coupling effects between bending and torsion. The displacements are expressed with interpolation functions with natural coordinates. The interpolation function in x and angular direction are the same as for the bar, shown in equation 3.16. However, in y and z-direction the interpolation functions are cubic.

From virtual work in equation 3.12, the internal reaction forces can be expressed in equation 3.26.

$$\mathbf{S}_{int} = \begin{bmatrix} S_u \\ S_v \\ S_w \\ S_\theta \end{bmatrix} = \int_{L_0} \begin{bmatrix} \mathbf{N}_{u,x}^T \\ \mathbf{N}_{v,xx}^T \\ \mathbf{N}_{w,xx}^T \\ \mathbf{N}_{\theta,xx}^T \end{bmatrix} \begin{bmatrix} N_{xx} \\ M_y \\ M_z \\ M_\theta \end{bmatrix} dx \tag{3.26}$$

The equation consist of cross-section force resultants, which are determined from moment-curvature and axial force-elongation curves. By using the incremental form of virtual work principle defined in equation 3.13, the geometric and material stiffness can be found the same way as for the bar element.

The external nodal load vectors are expressed in equation 3.27, where $\mathbf{N}$ is defined in equation 3.16.

$$\mathbf{S}^e = \begin{bmatrix} \mathbf{S}_u^e \\ \mathbf{S}_v^e \\ \mathbf{S}_w^e \\ \mathbf{S}_\theta^e \end{bmatrix} = \int_L \begin{bmatrix} \mathbf{N}_u \\ \mathbf{N}_v \\ \mathbf{N}_w \\ \mathbf{N}_\theta \end{bmatrix}^T \mathbf{N} \begin{bmatrix} \mathbf{p}_x \\ \mathbf{p}_y \\ \mathbf{p}_z \\ \mathbf{p}_\theta \end{bmatrix} dx \tag{3.27}$$

Both structural and added mass are considered in the mass matrix. The structural mass is given by equation 3.28.

$$\mathbf{m}^s = \begin{bmatrix} \mathbf{m}^s_{uu} \\ \mathbf{m}^s_{vv} \\ \mathbf{m}^s_{ww} \\ \mathbf{m}^s_{\theta\theta} \end{bmatrix} = m^s \int_{L_0} \begin{bmatrix} \mathbf{N}_u \\ \mathbf{N}_v \\ \mathbf{N}_w \\ \mathbf{N}_\theta \end{bmatrix}^T \begin{bmatrix} \mathbf{N}_u \\ \mathbf{N}_v \\ \mathbf{N}_w \\ \mathbf{N}_\theta \end{bmatrix} dx \tag{3.28}$$

The added mass is given by equation 3.29. The added mass per unit length changes with the direction.

$$\mathbf{m}^h = \begin{bmatrix} \mathbf{m}^s_{uu} \\ \mathbf{m}^s_{vv} \\ \mathbf{m}^s_{ww} \\ \mathbf{m}^s_{\theta\theta} \end{bmatrix} = \int_{L_0} \begin{bmatrix} \mathbf{N}_u \\ \mathbf{N}_v \\ \mathbf{N}_w \\ \mathbf{N}_\theta \end{bmatrix}^T \begin{bmatrix} m^h_x \\ m^h_y \\ m^h_z \\ m^h_\theta \end{bmatrix} \begin{bmatrix} \mathbf{N}_u \\ \mathbf{N}_v \\ \mathbf{N}_w \\ \mathbf{N}_\theta \end{bmatrix} dx \tag{3.29}$$

Both structural and hydrodynamic damping are considered in the damping matrix. The structural damping is expressed with the Rayleigh damping model, and is presented in 3.2.3. There are no damping contributions for the hydrodynamic damping in x-direction, but for y, z and angular direction the damping is expressed in equation 3.30 (MARINTEK, 2015a).

$$\mathbf{c} = \begin{bmatrix} \mathbf{c}_{uu} \\ \mathbf{c}_{vv} \\ \mathbf{c}_{ww} \\ \mathbf{c}_{\theta\theta} \end{bmatrix} = \int_{L_0} \begin{bmatrix} \mathbf{N}_u \\ \mathbf{N}_v \\ \mathbf{N}_w \\ \mathbf{N}_{w\theta} \end{bmatrix}^T \begin{bmatrix} 0 \\ c^h_y \\ c^h_z \\ c^h_\theta \end{bmatrix} \begin{bmatrix} \mathbf{N}_u \\ \mathbf{N}_v \\ \mathbf{N}_w \\ \mathbf{N}_\theta \end{bmatrix} dx \tag{3.30}$$

Flexcom uses a 3D beam element called a hybrid beam-column element with fourteen DOFs, as shown in figure 3.7. The axial force is interpolated separately from the axial strain, and the stress-strain compatibility relationship is not inserted into the virtual work, but applied outside with Lagrangian constraints. The torque has also been applied with Lagrangian constraints.

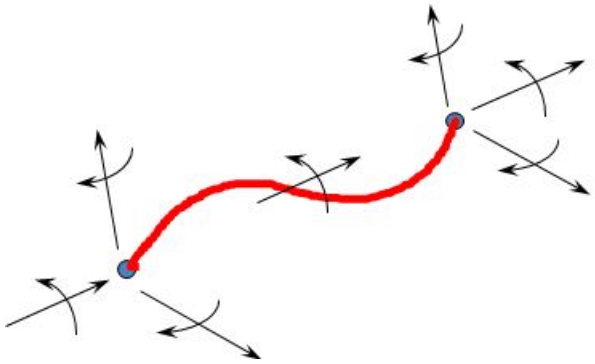

Figure 3.7: Hybrid beam-column element (Wood Group Kenny, 2015)

The method for solving the equilibrium equations is called the convected coordinate method (CCM). Each element has a convected coordinate axis (CCA) which follows the movement of the element as it displays through space, as shown in figure 3.8. The local displacement vector in the convected axis system is defined as $u^{def} = [u_x u_y u_z]$ and the local rotation vector as $u^d ef = [w_x - u'_z u'_y]$, when assuming small rotations. Each element has an equation of motion according to the CCA, and is assembled into the global set of equations. The equation of motion for each element are obtained from the virtual work statement, which includes calculation of the internal virtual work and the external virtual work.

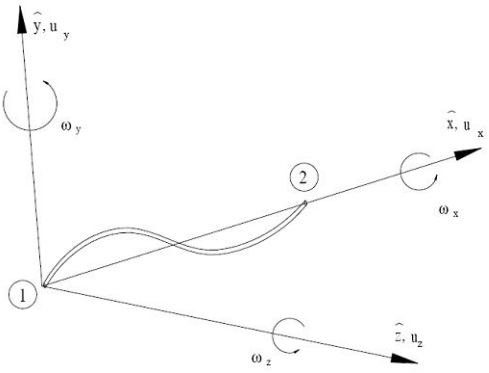

Figure 3.8: Convected axis system (Wood Group Kenny, 2015)

The internal virtual work is calculated by substituting the strains and the stresses into the internal virtual work statement. The strains are Greens strains, and are a sum of the linear and nonlinear strains. They are presented both on total and incremental form for calculation of the internal virtual work. The stresses are 2nd Piola-Kirchhoff stresses and are given by the axial force and the torque moments. An additional stress vector is defined due to the applied Lagrange constraints, which is solved directly in the finite element equations. The external virtual work is calculated by substituting the displacements and accelerations into the external virtual work statement. The displacements and accelerations are found by interpolation of the nodal solution vector. The local nodal solution vector d^{def} is based on the local rotation vector and the local displacement vector given above. The interpolation is linear for u_x and w_x, but cubic for u_y and u_z. The forces, axial force and torque moment in x-direction, are constant over the element. The equation of motion for each element is rotated before assembling them into the global set of equations (Wood Group Kenny, 2015).

3.2 Analysis

3.2.1 Static analysis

In order to obtain equilibrium, a static analysis is conducted. A static analysis in RIFLEX begins with equation 3.31. The displacement vector is found from this equation.

$$\mathbf{R}^S(r) = \mathbf{R}^E(r) \tag{3.31}$$

The left hand side of the equation represents the internal reaction force vector, and the right hand side represents the external force vector. Both of the reaction forces are nonlinear functions.

The static equilibrium is found with Euler-Cauchy incrementation. This procedure is based on dividing the load into small increment loads, and then solve for equation 3.31 for each step. The difference in force vectors is given in equation 3.32.

$$\mathbf{R}_k(r) = \mathbf{R}_k^S(r) - \mathbf{R}_k^E(r) \tag{3.32}$$

The displacement vector from the previous incremental load step, k, is used to solve the equation. The displacement vector at the new incremental load step is given in equation 3.33, where Δr_k^0 is shown in equation 3.34.

$$\mathbf{r}_k^0 = \mathbf{r}_{k-1} - \Delta\mathbf{r}_k^0 \tag{3.33}$$

$$\Delta\mathbf{r}_k^0 = -\left[\frac{\partial\mathbf{R}_{k-1}}{\partial\mathbf{r}}\right]^{-1}(\mathbf{R}_{k-1}^S - \mathbf{R}_k^E) \tag{3.34}$$

The partial derivative in 3.34 represents the tangential stiffness matrix, K, which be expressed as in equation 3.35. K_S represents the material and geometric stiffness and K_E represents load correction stiffness from the change of the displacement vector (MARINTEK, 2015a).

$$\mathbf{K} = \frac{\partial\mathbf{R}}{\partial\mathbf{r}} = \frac{\partial\mathbf{R}^S}{\partial\mathbf{r}} - \frac{\partial\mathbf{R}^E}{\partial\mathbf{r}} = \mathbf{K}_S - \mathbf{K}_E \tag{3.35}$$

Euler-Cauchy method does not fulfill total equilibrium, as shown in figure 3.9 (Moan, 2003).

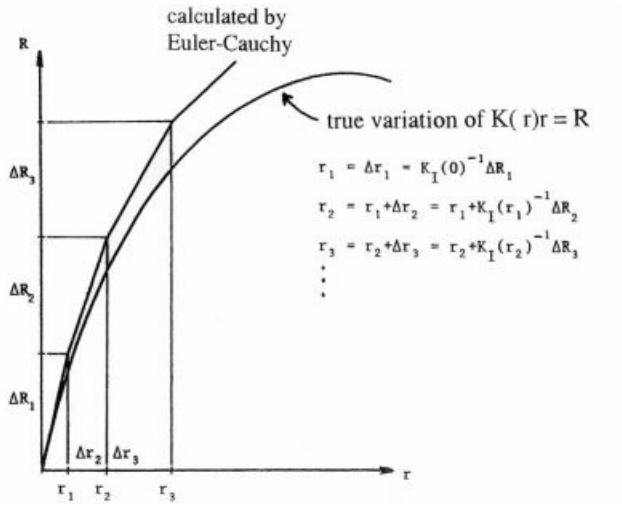

Figure 3.9: Euler-Cauchy incrementation (Moan, 2003)

In order to correct the displacement vector, an approach called Newton-Raphson iteration procedure is adopted. The displacement correction is shown in equation 3.36 and 3.37 (MARINTEK, 2015a).

$$\mathbf{r}_k^j = \mathbf{r}_k^{j-1} - \Delta\mathbf{r}_k^j \tag{3.36}$$

$$\Delta\mathbf{r}_k^j = \left[\frac{\partial \mathbf{R}_{k-1}}{\partial \mathbf{r}}\right]^{-1} \mathbf{R}_k^{j-1} \tag{3.37}$$

The Newton-Raphson approach is shown in figure 3.10 and the combination of the incremental and iterative method is shown in figure 3.11 (Moan, 2003).

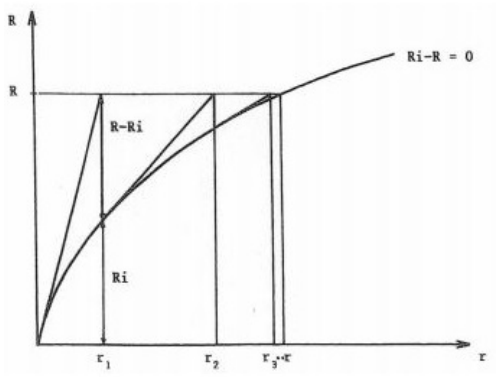

Figure 3.10: Newton-Raphson method (Moan, 2003)

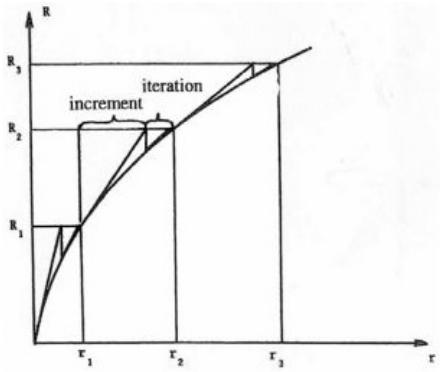

Figure 3.11: Combination of incrementation and iteration (Moan, 2003)

The convergence criterion is given in equation 3.38, where $|| r_k ||= \frac{1}{N}\sum_{i=1}^{\infty} r_{ki}^2$ and ϵ is a given tolerance (MARINTEK, 2015a).

$$\frac{|| \Delta \mathbf{r}_k^j ||}{|| \mathbf{r}_k^j ||} = \frac{|| \mathbf{r}_k^j || - || \mathbf{r}_k^{j-1} ||}{|| \mathbf{r}_k^j ||} < \epsilon \tag{3.38}$$

The increment steps must be small, and the analysis can therefore be time consuming because equation 3.35 must be updated for each step. The efficiency can be increased with modified Newton-Raphson method, where equation 3.35 is either updated after first iteration or never updated (Moan, 2003).

Flexcom solves the static analysis the same way as RIFLEX. Loads and displacement are divided into increments, and are increased linearly to their full value over n steps. Convergence to equilibrium is obtained by iteration to another fixed point in order to account for the nonlinearities. This is done by updating the global rigid body vector D_{rb} on the convected axis. The global rigid body vector is obtained from the global rigid body translation vector U_{rb}. The global rigid body translation vector U_{rb} is added to the global displacement vector U_{def}, which gives the translation deformation components U. The translation deformation of a material point is shown in figure 3.12.

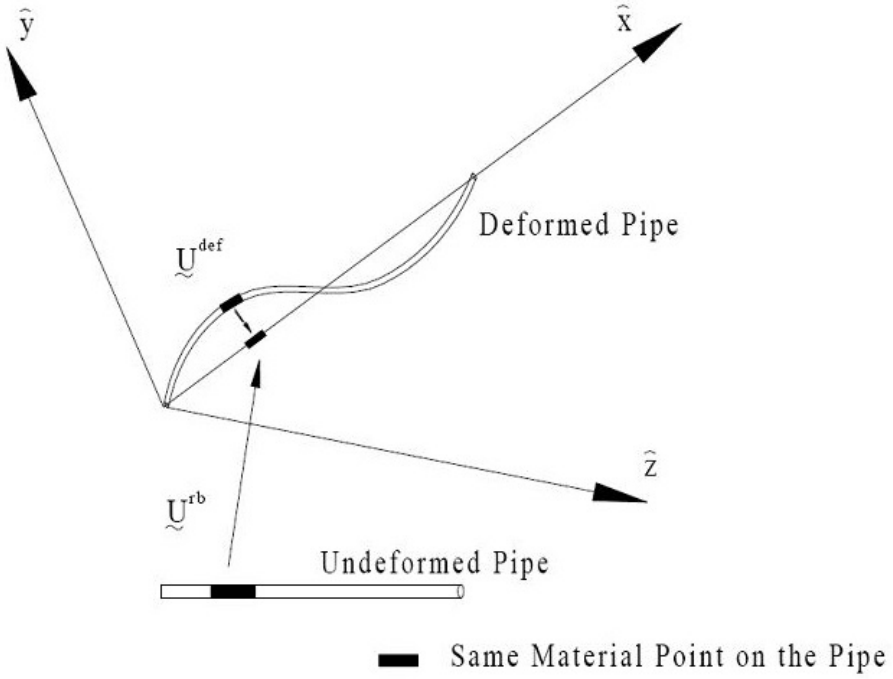

Figure 3.12: Translation deformation of a point in the material (Wood Group Kenny, 2015)

The total nodal solution vector is obtained from this, and is a sum of the global nodal solution vector D^{def} and the global rigid body vector D_{rb} from the transformation of the local equilibrium equations from the local convected axis to the global axis. By updating the global rigid body vector D_{rb}, the geometric nonlinearities form large deflections are taken into account (Wood Group Kenny, 2015).

3.2.2 Eigenvalue analysis

In order to obtain the natural frequencies and mode shapes of the structure, an eigenvalue analysis is conducted. The result from an eigenvalue analysis will give an indication on how the structure will behave when it is exposed to dynamic loading (DNV, 2010a).

An eigenvalue analysis in RIFLEX is derived from the dynamic equilibrium equation given in equation 3.39.

$$\mathbf{M}\ddot{r} + \mathbf{C}\dot{r} + \mathbf{K}r = \mathbf{Q}(t) \tag{3.39}$$

The damping matrix and the load for a free undamped vibration is set equal to 0, and the dynamic equilibrium equation is reduced to equation 3.40.

$$\mathbf{M}\ddot{r} + \mathbf{K}r = 0 \tag{3.40}$$

Since the vibration is harmonic, the displacement can be expressed as shown in equation 3.41.

$$r = \phi sin(\omega t) \tag{3.41}$$

When inserting the equation for displacement, r, into the dynamic equilibrium equation, the general eigenvalue problem is obtained, as shown in equation 3.42, where ϕ is the eigenvector, ω is the eigenfrequency, K is the stiffness matrix and M is the mass matrix.

$$(\mathbf{K} - \omega^2\mathbf{M})\phi = 0 \tag{3.42}$$

The stiffness matrix is symmetric and banded. The mass matrix is also symmetric, however it can be either banded or diagonal, depending on whether the mass is consistent of concentrated.

An important property of the eigenvectors is that they are linearly independent. This means that the displacement can be expressed as a linear combination of mode shapes, as shown in equation 3.43, where ϕ are the mode shapes and y is the displacement amplitudes. This is convenient because the total solution can then be found by modal superposition.

$$\mathbf{r} = \sum_{i=1}^{n} \phi_i y_i(t) = \phi \mathbf{y} \tag{3.43}$$

In order to use superposition principles, a modal equation of motion must be found for each mode shape. This can be found by transforming the coupled dynamic equilibrium equation into an uncoupled set of equations. The set of equations are expressed with generalized quantities, which are derived by using orthogonality properties. The properties are shown in equation 3.44 an 3.45. The same properties are also assumed for the damping matrix (Langen & Sibjørnsson, 1979)

$$\phi_i^T \mathbf{K} \phi_j = 0, \quad \text{when} \quad i \neq j \tag{3.44}$$

$$\phi_i^T \mathbf{M} \phi_j = 0, \quad \text{when} \quad i \neq j \tag{3.45}$$

Flexcom solves the eigenvalue analysis the same way as RIFLEX, by solving for equation 3.42 (Wood Group Kenny, 2015).

3.2.3 Dynamic analysis

A dynamic analysis is conducted in order to investigate how the structure behaves when exposed to dynamic loading. The system becomes nonlinear because the inertia and damping forces depends on the displacement, and because the internal force vector and the external force vector depend on the displacement vector. In addition, the external force vector also depends on the velocity. The dynamic equilibrium equation in RIFLEX is given in equation 3.46.

$$\mathbf{R}^I(r,\ddot{r},t)+\mathbf{R}^D(r,\dot{r},t)+\mathbf{R}^S(r,t)=\mathbf{R}^E(r,\dot{r},t) \tag{3.46}$$

The inertia force vector, R^I, consist of mass from fluid, structural mass and hydrodynamic mass. The damping force vector, R^D, consist of structural and hydrodynamic damping, in addition to discrete dashpot dampers.

There are three possible analysis methods; nonlinear time domain analysis, linearized time domain analysis and frequency domain analysis. The nonlinearities accounted for in these analysis are the geometric stiffness, contact problems, nonlinear material, load integration to the exact surface and hydrodynamic loading when relative velocity is accounted for. The nonlinear time domain analysis is a numerical integration procedure of the incremental dynamic equilibrium equation. The procedure is based on Newton-Raphson, and is time consuming because the mass, damping and stiffness matrices must be updated for each step. In order to decrease computational time, a linearized time domain analysis is a possibility. The method is based on constant system matrices, expect for hydrodynamic loading, which is updated for each step. The third option is the frequency domain analysis, where all the system matrices are linearized at static equilibrium (MARINTEK, 2015a). According to DNV standards it is common to conduct a time domain analysis for marine risers(DNV, 2010a)

The dynamic equilibrium equation is solved based on Newmark β -family and Wilson θ -method, shown in equation 3.47 and 3.48.

$$\dot{\mathbf{r}}_{t+\Delta\tau}=\dot{\mathbf{r}}_t+(1-\gamma)\ddot{\mathbf{r}}_t\Delta\tau+\gamma\ddot{\mathbf{r}}_{t+\Delta\tau}\Delta\tau \tag{3.47}$$

$$\mathbf{r}_{t+\Delta\tau} = \mathbf{r}_t + \dot{\mathbf{r}}_t \Delta\tau + (\frac{1}{2} - \beta)\ddot{\mathbf{r}}_t (\Delta\tau)^2 + \beta\ddot{\mathbf{r}}_{t+\Delta\tau}(\Delta\tau)^2 \tag{3.48}$$

From these equations the displacement and velocity are found, as shown in figure 3.13.

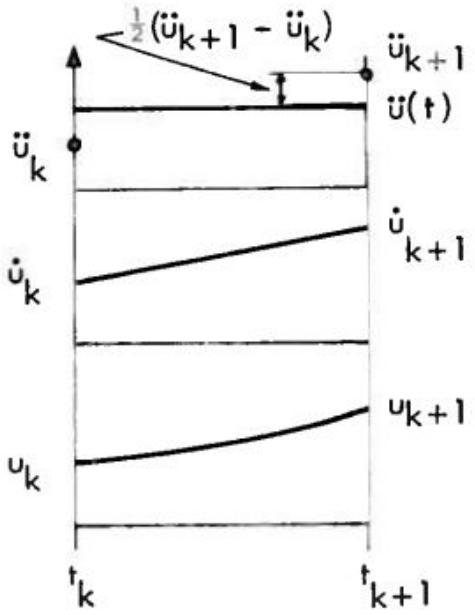

Figure 3.13: Constant average acceleration (Langen & Sibjørnsson, 1979)

From Wilson- method, the acceleration is interpolated between time t and t+ Δ t, as shown in equation 3.49, where θ is equal to 1.

$$\ddot{\mathbf{r}}_{t+\Delta\tau} = \ddot{\mathbf{r}}_t + \frac{1}{\theta}(\ddot{\mathbf{r}}_{t+\Delta\tau} - \ddot{\mathbf{r}}_t) \tag{3.49}$$

The γ value describes a system with or without artificial damping. If there are no artificial damping, the value is equal to 1/2. When the acceleration is assumed constant over each time step, β is equal to $\frac{1}{4}$. The time domain analysis is performed by using Newton-Raphson iteration, which integrates the incremental dynamic equilibrium equations. In the equations, tangential mass, damping and stiffness matrices are used in the beginning of the increment, in order to linearize the equation. The tangential stiffness matrix can be established as a linear combination. The equation is given by the global Rayleigh damping model. The model gives the overall damping

level, and is shown in equation 3.50.

$$\mathbf{C} = \alpha_1 \mathbf{M} + \alpha_2 \mathbf{K} \tag{3.50}$$

An important aspect with this model is that the damping matrix is orthogonal to the eigenvectors. With this property, the modal damping for a linear system can be expressed as shown in equation 3.51, where ω is the eigenfrequency.

$$\lambda_i = \frac{1}{2}\left[\frac{\alpha_1}{\omega_i} + \alpha_2 \omega_i\right] \tag{3.51}$$

At the end step of the iterations, the dynamic equilibrium equation is not satisfied. This must be corrected by iteration. A modified Newton-Raphson procedure can be applied in order to decrease computational time.

The loads acting on the system comes from weight and inertia, hydrostatic forces, hydrodynamic forces and forced motion of line.

Hydrostatic pressure

The beam elements have pressure independent cross-section properties in the analysis, and the equilibrium conditions will therefore not be affected by the hydrostatic pressure level. The result of this is that the structure can be analyzed with a volume force model, which use vertical, conservative forces to represent the hydrostatic effects. Since the forces are in equilibrium with the effective tension, the axial force is left out when calculating the equilibrium for one iteration.

The hydrostatic pressure is therefore determined based on the effective weight and effective tension defined in equation 3.52 and 3.53 respectively.

$$w = m_p g - A_e \rho g + A_i \rho_i g \tag{3.52}$$

The mass in the equation is the mass of the pipe per unit length.

$$T = T_p - A_e P_e - A_i P_i - \rho_i A_i v_i^2 \tag{3.53}$$

The index notations refer to internal area and pressure, i.e. A_i and P_i, and the external area and pressure, i.e. A_e and P_e. The tension in the pipe wall, which comes from the normal stresses, are given as T_p in the equation and the v_i is the velocity of the internal fluid (MARINTEK, 2015a).

Hydrodynamic pressure

A generalized Morison's equation is used to calculate the hydrodynamic forces for an element dx in three directions, as shown in equation 3.54.

$$F_R = dx[(\rho A + m_a^R)\dot{u}_x^I - m_a^R \ddot{r}_R + C_D^R \mid U_R^c + u_R^I - \dot{r}_R \mid (U_R^c + u_R^I - \dot{r}_R) + C_{DL}^R (U_R^c + u_R^I - \dot{r}_R)] \tag{3.54}$$

The directions are denoted R in the equation, and represent the x, y and z-direction. The parameter r is the displacement component of the structure, ρ the water density, m_a the added mass in 2D, C_D the quadratic drag coefficient, C_{DL} the linear drag coefficient, U^c the current velocity component and u^I the velocity component (MARINTEK, 2015a). According to DNV rules, the added mass coefficients should be 2, and the drag coefficient between 0.7 and 1.0 (DNV, 2010a).

The dynamic analysis in Flexcom is found by solving for the equilibrium equations at discrete time steps. The discretization of the equations are solved with the Hilber-Hughes-Taylor method, which is a special case of the Generalised-α-method. The variation of displacement, velocity and acceleration for each time interval is solved by implicit integration which means that equations of motion are solved for each solution time. In other words, the solution at time $t + \Delta t$ is based on the condition at time $t + \Delta t$, and not at t, which is for explicit integration. In order to ensure that the equilibrium equations are solved at any time of the solution, the steps must be small enough. The velocity and the acceleration are found by solving the equations for the Generalised-α-method by setting α_m =0. The damping model used in the analysis is the Rayleigh damping model. This is the same model which is used in RIFLEX. The stiffness component in the damping model includes both the geometric and the structural stiffness. The hydrodynamic forces are calculated with Morison's equation (Wood Group Kenny, 2015).

3.2.4 Fatigue analysis

Fatigue crack growth for welded joints goes through three stages, initiation phase, fatigue crack growth phase and final failure phase. Phase one is often dominating in machined components with smooth surface. The initiation phase is modeled based on cyclic strain. For low cyclic strain the plastic strain is the governing, but for high cyclic strain, the elastic strain is governing. The fatigue crack growth is dominating in phase 2. The reason behind this is because of defects due to the choice of material, welding procedure and other factors. The crack growth is due to cyclic stresses/strains at the crack tip. The stresses are often below yield at this stage, which makes it possible to apply linear elastic fracture mechanics. The stress/strain field is characterized by the stress intensity factor K, which is related to the cyclic stress intensity factor ΔK. The crack growth rate is given by the Paris-Erdogan crack growth relation $\frac{da}{dn} = C(\Delta K)^m$, where C and m are fitting parameters. In the last phase the crack growth rate will increase significantly and lead to failure. The crack growth curve is shown in figure 3.14.

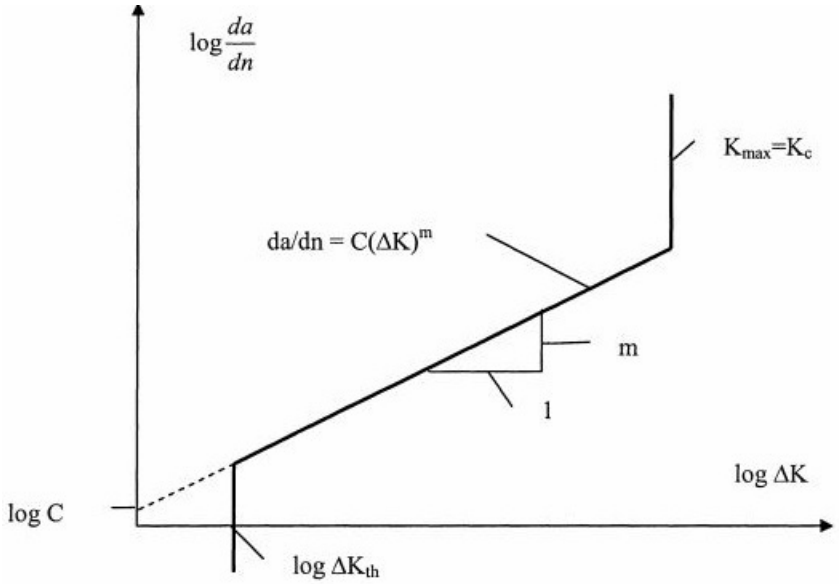

Figure 3.14: Crack growth curve (Berge, 2006)

The crack growth curve can be directly related to the S-N curve, where the exponent m of the Paris' law becomes the negative inverse slope of the S-N curve (Berge, 2006).

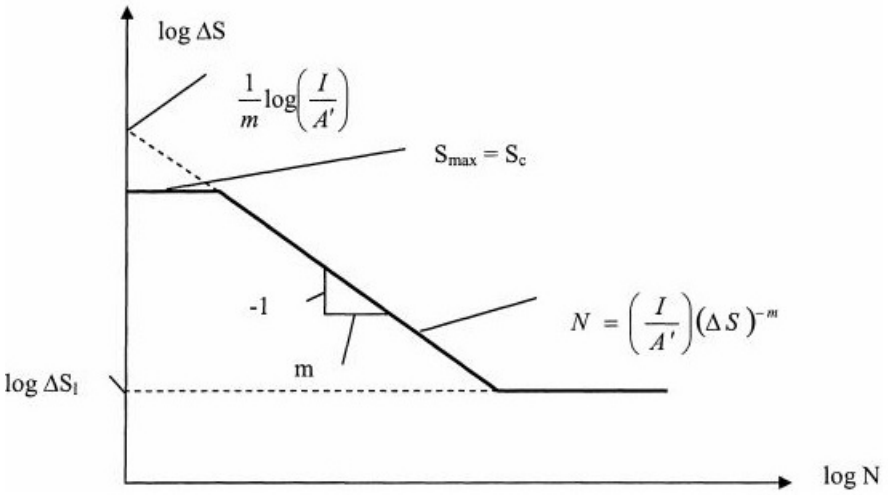

Figure 3.15: S-N curve relation to the crack growth curve (Berge, 2006)

The S-N curves are found experimentally and give the number of cycles to failure, N, for a given stress range, $\Delta\sigma$, as shown by equation 3.55. The parameter m is the negative inverse slope of the S-N curve and log ā represent the intercept of log N axis, given by equation 3.56.

$$logN = log\bar{a} - mlog\Delta\sigma \tag{3.55}$$

log a is the intercept of the log N axis with the mean S-N curve and $s_{\log N}$ is the standard deviation for log N (DNV, 2011a).

$$log\bar{a} = loga - 2s_{logN} \tag{3.56}$$

If the pipe thickness is larger than 25 mm, a thickness correction factor, which gives the ratio between the average pipe wall thickness and the reference wall thickness, is applied (DNV, 2010b). The S-N curve is then given by equation 3.57 (DNV, 2011a).

$$logN = log\bar{a} - mlog\left(\Delta\sigma\left(\frac{t}{t_{ref}}\right)^k\right) \tag{3.57}$$

Load-time histories can be obtained from the time domain analysis. The load-time histories have a variable amplitude loading, because the structure is affected by waves, wind and current. There are particular events which can be found in an irregular load-time history. These events are listed below and defined in the load-time history in figure 3.16 (Berge, 2006).

- Reversal is the event where the first derivative changes sign
- Peak is the event where the first derivative changes from being positive to negative
- Valley is the event where the first derivative changes from being negative to positive
- Range can either be positive or negative. A positive range is the difference between a valley and peak, while a negative range is the difference between a peak and valley.
- Mean crossing is the total number of times the mean load level is crossed.

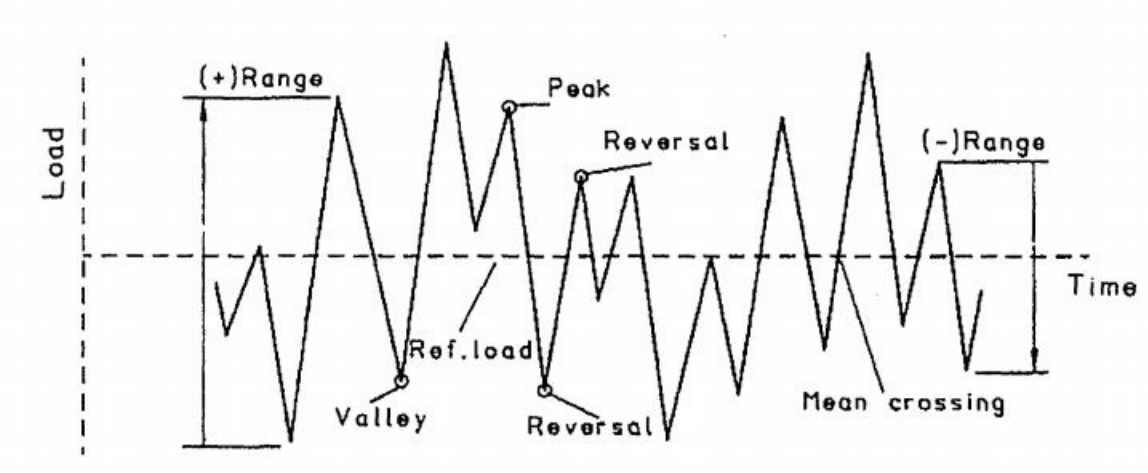

Figure 3.16: Load history (Berge, 2006)

The load-time histories can be transformed into stress-time histories. This is calculated based on equation 3.58 (MARINTEK, 2015b).

$$\sigma_{as} = \frac{T_w}{A} + \frac{M_y}{W} + \frac{M_z}{W} \tag{3.58}$$

The stress-time histories can then be divided into individual cycles. The cycles can be counted with different methods and the method which gives the most accurate representation of the fatigue process, should be selected in the analysis. Some examples of counting methods are peak counting, simple range counting, level crossing counting and rainflow counting. If the low-cycle fatigue is to be investigated, the recommended method is the rainflow counting method. Additionally, the bandwidth of loading is an important factor for selecting the correct counting method. If the loading is narrow-banded, all four methods can be used above. However, for wide-banded loading the recommended method is rainflow counting.

The Rainflow counting method counts the reversals in the load history, which is given by the stress-strain response of the material. The principle behind the method is shown in figure 3.17 and 3.18. The cycles are counted for each time the hysteresis loop is closed. The strain-stress history is unaffected by each of the cycles.

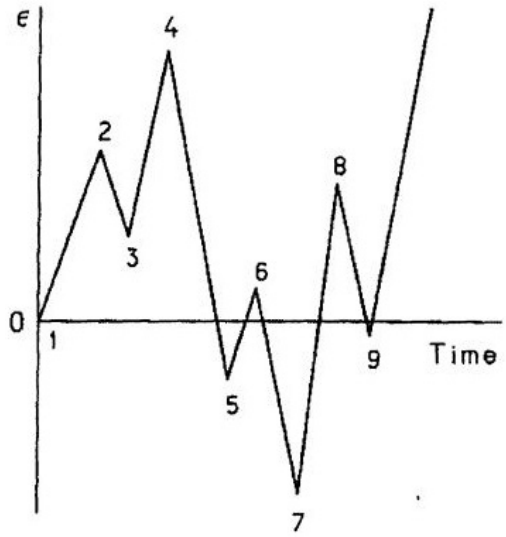

Figure 3.17: Strain history (Berge, 2006)

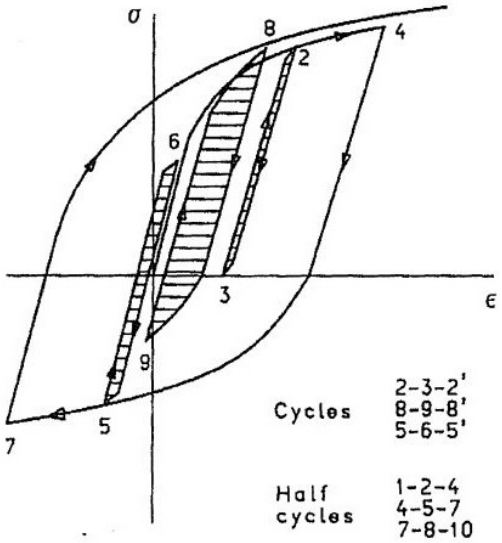

Figure 3.18: Stress-strain response (Berge, 2006)

The rainflow method comes from the pagoda roof analogy, shown in figure 3.19. The counting is performed in the three steps listed below the figure.

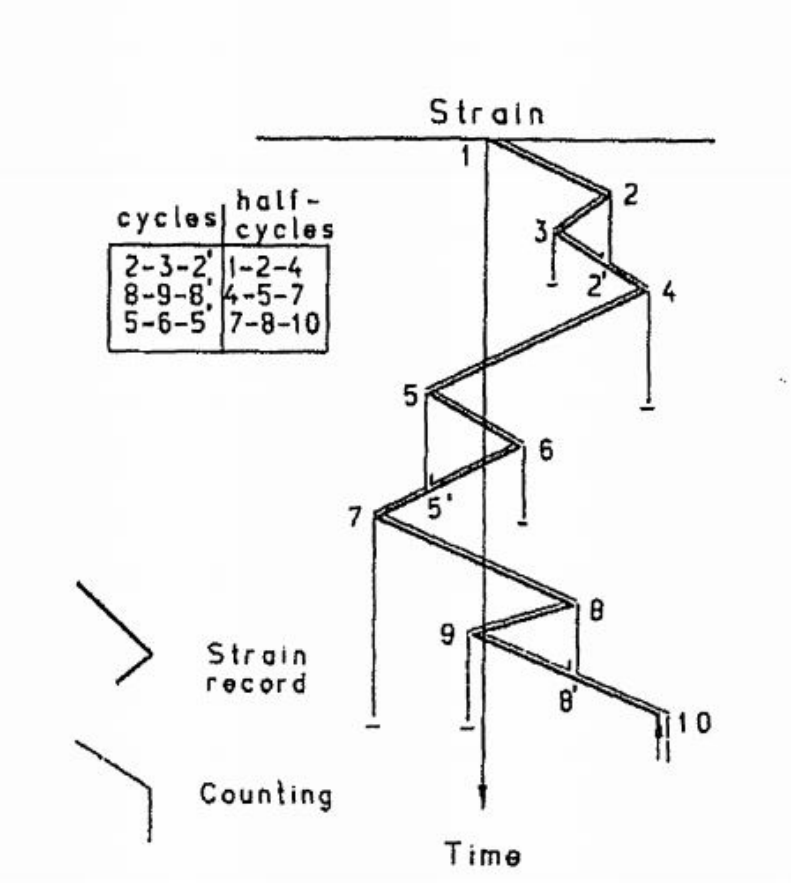

Figure 3.19: Pagoda roof rainflow analogy (Berge, 2006)

- From inside of each peak/valley, the rain will drop down from the roof till it hits the edge. Further will the rain drip from the edge of the roof.
- The cycle is completed when the rain meets another flow from above.
- If the flow starts from valley, the flow will stop when it comes opposite of another valley, if the valley has a higher negative value. If the flow starts from a peak, the flow will stop when it comes opposite of another peak, if the peak has a higher positive value.

The rainflow counting is performed for each load history representing a sea state. After counting all the cycles, the fatigue damage can be found by Miner-Palmgren summation (Berge, 2006). The Miner-Palmgren summation is quite simple, but has proven to give good accuracy. The theory behind the method assumes that the damage per load cycle at a given stress range is constant D = 1/N. In this equation the N represents the constant amplitude endurance, given at a certain stress range (Almar-Næss, 1985).

For a stress history, the Miner-Palmgren summation can be written as shown in equation 3.59. The numerator in the fraction is the number of stress cycles, n, for a given range S_i. The denominator is the total number of stress cycles to failure, which is expressed by the S-N curve in equation 3.55.

$$D = \sum_i \frac{n(S_i)}{N(S_i)} \tag{3.59}$$

The damage obtained from the summation must fulfill a given criterion, which is given in equation 3.60. The DFF is the design fatigue factor which is a safety factor which increases the probability. This factor is applied to avoid failure from fatigue (DNV, 2010b).

$$D \cdot DFF \leq 1 \tag{3.60}$$

3.2.5 Vortex induced vibration analysis

Slender structures are often influenced by vortex-induced vibrations. VIV are vibrations from vortices shed from a cylinder, when placed in an environment with current. Two vortices are shed for one cycle, and from this forces are developed. The forces are either in the in-line (IL) direction or the cross-flow (CF) direction. The IL-force have twice the vortex shedding frequency, while the CF-force have the same frequency as the vortex shedding frequency. The force that cause the CF vibrations is the lift force, and the force that cause the IL vibrations is the drag force. The latter force is greatly affected by VIV. When VIV increases the drag force increases too. This means that VIV will influence the static deformation.

The vortex shedding frequency is defined in equation 3.61, where St is the Strouhals number, U is the flow speed and D is the diameter of the cylinder.

$$f_v = \frac{St \cdot U}{D} \tag{3.61}$$

The Strouhals number is a function of the Reynolds number, which defines the vortex shedding pattern behind a cylinder. However, for Reynold numbers between 300 and 300000 the Strouhals number is close to 0.2 and the vortex shedding process is close to constant. Experimental test are often conducted in this regime, but full-scale structures will experience much higher Reynolds numbers than the ones in the sub-critical regime. It is, however, been decided that one can use the data from the sub-critical regime for the full-scale structures, and still have a conservative analysis. In the latest publications there have been results showing that the Reynolds number has a certain effect which leads to a higher Reynolds number, and therefore affects the response. However, the results show great uncertainty and more data should be gathered for further investigation of this effect.

When the velocity of the incoming flow increase the frequency increase as well. This means that the IL response will be at a lower velocity oppose to the CF. This can observed in figure 3.20.

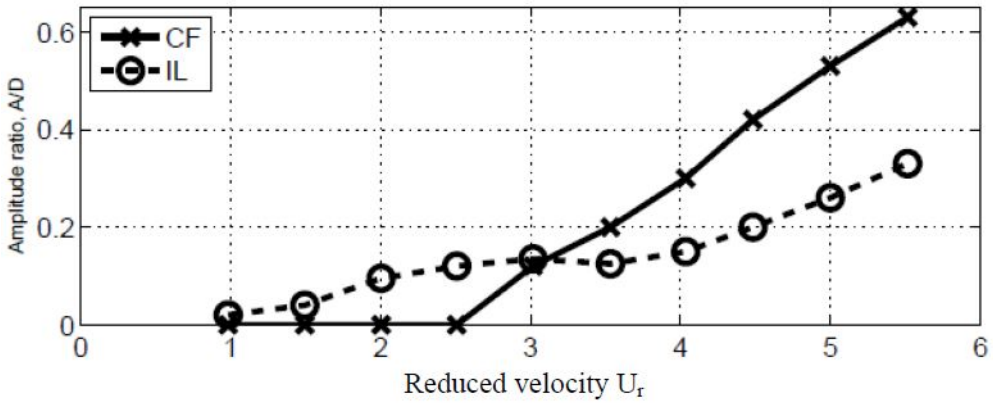

Figure 3.20: Response amplitude and reduced velocity for IL and CF respons (Larsen, 2011)

If a cylinder oscillates freely, a phenomenon called lock-in can occur. This means that the oscillation frequency controls the vortex shedding frequency, and changes its frequency. The oscillation frequency is defined in equation 3.62.

$$f_{osc} = \frac{1}{2\pi}\sqrt{\frac{k}{m+m_a}} \tag{3.62}$$

The oscillation frequency is different from the eigenfrequency because added mass changes. The eigenfrequency is given in equation 3.63.

$$f_o = \frac{1}{2\pi}\sqrt{\frac{k}{m+m_{a0}}} \tag{3.63}$$

How much the eigenfrequency will be affected by the added mass, depends on the amount of dry mass of the cylinder. Therefore, a heavy or light cylinder will have different responses since for a light cylinder the added mass is more able to change the eigenfrequency. This means that for a given velocity range, a light cylinder will vibrate for longer time. The vibrations depends on the response amplitude. The ratio A/D must be less than 1.2, otherwise damping will occur. An illustration of three different cylinders response to reduced velocity and flow speed is shown in figure 3.21 and figure 3.22 respectively.

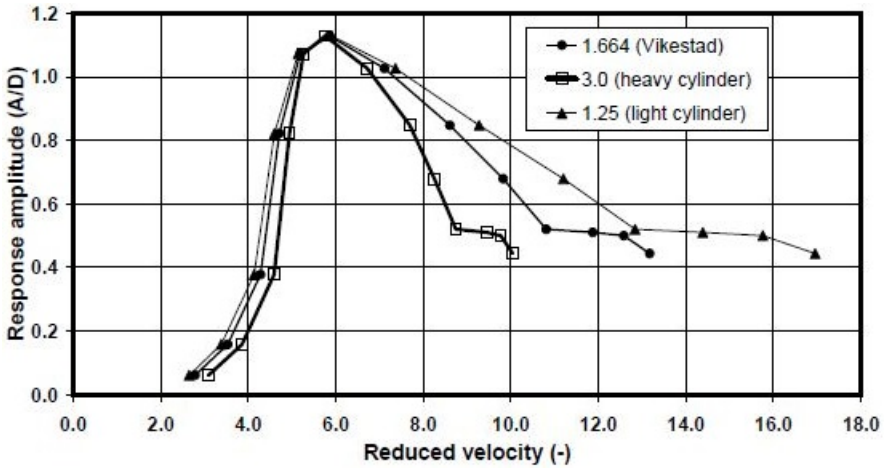

Figure 3.21: Response amplitude and reduced velocity for different cylinders (Larsen, 2011)

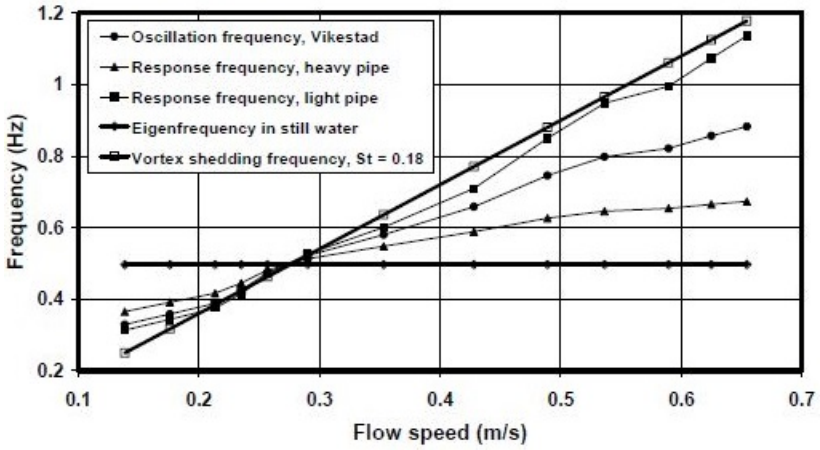

Figure 3.22: Frequency and flow speed for different cylinders (Larsen, 2011)

From a forced oscillation test the added mass, drag and lift force and force coefficients can be found. The oscillation pattern for the cylinder is harmonic and the added mass and the force coefficients are plotted in contour plots, one for each of the response. Since the CF response will always occur with the IL response, as shown in figure 3.20, the combined response coefficients must be found. However, the result from investigating this shows that the coefficients are greatly affected by small changes of the phase angles. In addition, the forces found from harmonic motions in CF and IL direction, are influenced significantly by higher order harmonic components (Larsen, 2011).

There have been several investigations of VIV and fatigue and several experimental tests have

been conducted. From the tests it has been shown that the IL vibrations can lead to fatigue damage. This is because of the high number of cycles. CF vibrations can also lead to fatigue. This is because of the high vibration amplitudes (Suzuki et al., 2015).

3.3 Stochastic theory

3.3.1 Regular wave environment

The regular wave environment can be modeled with Airy linear wave theory or with Stoke's fifth order wave theory. The two methods differ from where the boundary condition pressure is defined. For Airy linear wave theory, the pressure is defined at the mean water level (MWL). This means that the theory is only valid for infinitesimal amplitudes. For Stoke's fifth order wave theory the pressure is approximated at the MWL. This means the wave has a finite height and describes therefore well the accelerations and wave induced velocities in the wave crest. Figure 3.23 illustrates the two wave theories (MARINTEK, 2015a).

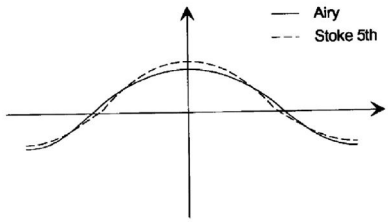

Figure 3.23: Airy linear wave and Stoke's 5th wave profile (MARINTEK, 2015a)

3.3.2 Irregular wave environment

The wave elevation of the irregular wave environment is created by summation of wave components, as shown in equation 3.64. The amplitude, A_j, is given in equation 3.65.

$$\psi = \sum_{j=1}^{N} A_j sin(\omega_j t - k_j x + \epsilon_j) \tag{3.64}$$

$$\frac{1}{2}A_j^2 = S(\omega_j)\Delta\omega \tag{3.65}$$

The circular frequency, ω_j, and the wave number, k_j, are given by the dispersion relation and the random phase angle, ϵ_j, is uniformly distributed between 0 and 2π. The Gaussian distribution represent the instantaneous wave elevation. This distribution has properties resulting in a zero mean value and a variance which can be shown to be equal to equation 3.66 (Faltinsen, 1998).

$$\sigma^2 = \int_0^\infty S(\omega)d\omega \tag{3.66}$$

The wave spectrum used in the analysis is 3-parameter JONSWAP spectrum. The spectrum is developed for the North Sea area, and is limited to fully developed sea states (Myrhaug, 2007). The spectrum is calculated according to equation 3.67, where $\sigma = 0.07$ if $\omega \geqslant \omega_p$ and $\sigma = 0.09$ if $\omega_p \geqslant \omega$ (MARINTEK, 2013).

$$S_\eta(\omega) = \frac{5}{31\pi}H_s^2 T_p \left(\frac{\omega_p}{\omega}\right)^5 exp\left(\frac{5}{4}\left(\frac{\omega_p}{\omega}\right)^4\right)(1-0.287lny)\gamma^{exp\left[\frac{\left(\frac{\omega}{\omega p}-1\right)}{2\sigma^2}\right]} \tag{3.67}$$

The γ is called the peakedness parameter and is calculated according to "Prediction of characteristic response for design purposes" by Statoil shown in equation 3.68 (Haver, 2013).

$$\gamma = 42.2\left(\frac{2\pi H_s}{gT_p^2}\right)^{6/7} \tag{3.68}$$

Chapter 4

Rules and standards

The relevant standards for marine drilling risers are *DNV-OS-F201-Dynamic risers* (DNV, 2010a) and *Design of Offshore Steel Structures, General-LRFD Method* (DNV GL, 2015). The relevant recommended practices are *DNV-RP-C203-Fatigue Design of Offshore Steel Structures* (DNV, 2011a), *DNV-RP-F204-Riser Fatigue* (DNV, 2010b), *API-RP-16Q-Design, Selection, Operation and Maintenance of Marine Drilling Riser Systems* (API, 2010a) and *API-16R-Specification for Marine Drilling Riser Couplings* (API, 2010b). The standards and recommended practises presented in this chapter are given for the marine drilling riser and the components used in the analysis in Flexcom.

4.1 Limit states

Marine riser systems are designed after four limit states, ultimate limit state (ULS), fatigue limit state (FLS), serviceability limit state (SLS) and accidental limit state (ALS). ULS requires that the riser has strength and stability to resist loads with 10^{-2} annual exceedance probability. ALS is a limit state based on ULS, but considers accidental loads instead. FLS is also based on ULS, but considers fatigue from cycle loads. SLS requires that the structure must be able to operate.

The loads acting in the system are pressure loads, functional loads, environmental loads and accidental loads. The pressure loads come from the internal and external hydrostatic pressures.

The functional loads come from the weight of the internal fluid, the weight and buoyancy of the riser, marine growth, applied tension, thermal loads etc. Environmental loads come from waves, current, ice, earthquake and floater motions. Accidental loads come from fire, explosions, collisions, etc.

The design loads are defined by multiplying the load with a load factor. The design bending moment is given in equation 4.1 and the design effective tension is given in equation 4.2. The index, F, represents the functional loads, E, the environmental and A, the accidental loads.

$$M_d = \gamma_F \cdot M_F + \gamma_E \cdot M_E + \gamma_A \cdot M_A \tag{4.1}$$

$$T_{ed} = \gamma_F \cdot T_{eF} + \gamma_E \cdot T_{eE} + \gamma_A \cdot T_{eA} \tag{4.2}$$

The load effect factors differ for each type of limit state. An overview of the load factors are given in table 4.1 (DNV, 2010a).

Limit state	γ_F	γ_E	γ_A
ULS	1.1	1.3	NA
FLS	1.0	1.0	NA
ALS/SLS	1.0	1.0	1.0

Table 4.1: Load factors for limit states

The ULS limit state can additionally be divided into two different load cases, as shown in table 4.2. Both cases must be considered in the design phase, and the condition which gives the most unfavorable outcome should be selected.

ULS	Permanent	Variable	Environmental	Deformation
A	1.3	1.3	0.7	1.0
B	1.0	1.0	1.3	1.0

Table 4.2: Load factors for ULS

The structure is considered safe if the design load effect, S_d is smaller or equal to the design resistance, R_d, as shown in equation 4.3.

$$S_d \leq R_d \tag{4.3}$$

The design resistance is defined as the product between the characteristic resistance and the resistance factor. The resistance factor is defined as one over the material factor (DNV GL, 2015). The material resistance factor is equal to 1.15 for ULS/ALS and 1.0 for FLS/SLS) (DNV, 2010a).

4.2 Drilling riser and components

4.2.1 Connections

The couplings can either be designed as dog-type, flange-type, collet-type, breech-block or threaded coupling. The dog-type coupling is a coupling with wedges between the pin and the box. The flanged type has flanged connections with bolts, and the collet-type a cylinder which connects the coupling members with each other. The breech-block coupling has a design which rotates slightly into another member, and the threaded coupling threads with a matching member.

The connector is designed according to a rated load, which is determined based on application of loads. The stresses are measured and calculated in the connection, and must not exceed the allowable stress limit. There are six classes of rated loads. These are 1.0, 1.25, 1.5, 2.0, 2.5 million pounds. The size of the riser couplings are based on the size of the main tube, and the main tube is often determined by the size of the BOP stack (API, 2010b).

4.2.2 Joints

The size of the joints are based on the size of the BOP, as mentioned above. The combinations of outer diameter and BOP stack are presented in table 4.3 (API, 2010b).

Main tube [inch]	BOP [inch]
16	13.5/8
18.5/8	16.3/4
20/21	18.3/4
22/24	20.3/4
24	21.1/4

Table 4.3: Tube and BOP dimensions

It is the diameter, thickness and strength of steel that determines the strength of the joint, and the stiffness properties are therefore found by only taking the steel part into consideration. The materials are usually X-52, X-65 and X-80. The numbers 52, 65 and 80 represent the yield strength in kilo pound per square inch. The length of the riser joints are often between 50 to 70 feet. The weight of the joint should include the weight of the main tube, choke, kill and auxiliary lines, couplings and brackets in the model (API, 2010a).

4.2.3 Buoyancy modules

The buoyancy modules are often made of syntactic foam from composites, and are often needed when the water depth becomes exceeds 2000 feet. The diameter of the foam is determined based on the density, which is depended on the water depth. In addition, the diameter is also depended on the required buoyancy and the bore of the diverter housing. The modules have geometry shape as a half circle, which is connected with another half circle by straps around the joint. The buoyancy joint has many modules along the total length of the joint (API, 2010a).

4.2.4 Flex joint

Flex joints are usually located at the bottom of the riser, but can also be found at the top and in the middle of the riser. The characteristics of the flex joint is given by the angle of rotation. The angle determines the rotation stiffness and varies between 10000 and 30000 foot-pounds per degree of rotation. When the joint is exposed to different loads, it is important that it remain its pressure integrity (API, 2010a).

4.2.5 Minimum tension

In order for the riser to be stable, the effective tension must be positive at all times. In order to ensure this, the top tension must be above a minimum criteria given by equation 4.4.

$$T_{min} = \frac{T_{SRmin} \cdot N}{R_f \cdot (N - n)} \tag{4.4}$$

T_{SRmin} is the minimum slip ring tension, and N is the number of tensioners while n is the number of failed tensioners. The factor R_f is between 0.9-0.95 and accounts for fleet angle and efficiency.

The effective tension is given by equation 4.5.

$$T_e = T_{real} - P_i A_i + P_o A_o \tag{4.5}$$

T_{real} is the axial pipe wall tension and the internal and external pressure,P, and area,A, are indicated with i for internal and o for external (API, 2010a).

4.2.6 Boundary conditions

The boundary conditions at the top of the riser includes the vessel motion and top tension. In addition to this, it is often common to apply a flex joint to the top of the riser, to account for the displacement of the rig. The bottom boundary conditions have usually a lower flex joint. If the casing and LMRP, BOP and wellhead are part of the model, an additional spring for the soil interaction should be modeled (API, 2010a).

4.3 Methodology

The methodology for the mechanical assessment of marine riser joints includes a global load analysis, a fatigue analysis and a VIV analysis. The methodologies suggested by standards and recommended practices, are given below.

4.3.1 Global analysis

A global riser analysis is performed in order to find the static and dynamic behavior of the structure. In the modeling phase, all components of the system must be included for correct solution of the system matrices. It is important that the discretization of the structure is thorough, in order properly represent environmental loads.

The first step in a global analysis is to perform a static analysis. The analysis is performed using a nonlinear approach, where the purpose of this analysis is to establish a static equilibrium configuration, by iteration from load increments due to weight, buoyancy, top tension and current. The next step is to perform an eigenvalue analysis and then a dynamic analysis. The reason for conducting an eigenvalue analysis before the dynamic analysis, is because the results will give an indication on how the structure will respond to dynamic loading. By investigating the response from the eigenvalue analysis, it is possible to discover situations were resonance could be present. In the dynamic analysis, the nonlinearities from the static analysis can be treated in three different ways, depending on the type of analysis. The different types are nonlinear time domain analysis, linearized time domain analysis and frequency domain analysis. The time domain analysis is the most common method, and is performed with Newton-Raphson equilibrium iteration. The hydrodynamic loads are calculated according to modified Morison equation, which accounts for relative velocity and acceleration. Loading from external and internal pressure is given by effective tension and weight. The damping is expressed by the Rayleigh damping model. (DNV, 2010a).

4.3.2 Fatigue analysis

A fatigue analysis must include wave induced cycles, low frequency cycles and vortex-induced cycles. A general approach for calculating the wave induced and low frequency induced damage, is to divide the scatter diagram into blocks. The probability of occurrence can then be found for all the sea states in the block, and one sea state is selected to represent the block. This means that the total probability is concentrated into the selected sea state. In order to calculate the fatigue damage for the selected sea state, the stress cycle distributions must be found in order to calculate the fatigue damage with a weighted fatigue damage accumulation, as expressed in equation 4.6. In the equation, P is the sea state probability and D is the short term fatigue damage (DNV, 2010a).

$$D_{fat} = \sum_{i=1}^{N_s} D_i P_i \tag{4.6}$$

It is the low and moderate sea states, with high probability of occurrence, that contribute most to the fatigue damage (DNV, 2010b). The S-N curves for different welded joints are found in *DNV-RP-C203-Fatigue Design of Offshore Steel Structures* (DNV, 2011a).

Marine risers have usually not narrow-banded nor wide-banded stress responses. If the narrow-banded assumption is valid, the stress cycles can be found from the stress maxima, and the zero-crossing frequency gives directly the number of cycles per unit time. If the wide-banded assumptions is valid, the distribution of the stress cycles can't be found from the distribution of the stress maximas. If both wave frequency and low frequency excitation are present, the response will be normally wide-banded. The damage must then be found with cycle counting, if a global time domain analysis is conducted. Rainflow counting is the recommended method for finding the damage (DNV, 2010a).

4.3.3 VIV analysis

The effect of VIV can contribute significantly to fatigue damage, and it is particularly important for drilling risers. VIV are divided into CF vibrations, CF induced IL vibrations and pure IL vibrations. The latter is usually not considered, which means the response will be non-conservative. Additionally, the axial stress from the CF vibration is not included, which also limits the results (DNV, 2010b).

A VIV analysis can be performed with four steps. The three last steps are required if more detailed analysis is needed (DNV, 2010a).

- Simplified analysis
- Multi-modal response analysis
- Computational fluid dynamics
- Testing

The simplified analysis is estimated with current and no waves. The steps in the analysis are listed below.

1. Use numerical finite element analysis (FEA) or analytical models to find mode shapes and natural frequencies in CF and IL direction

2. Find effective velocity and excitation length

3. Define the vortex shedding frequency as a function of effective velocity, hydrodynamic diameter and effective Strouhals number

4. Find the CF and IL frequency band for the excited modes

5. Find the amplitude for each mode from the excitation length for CF direction and from the mode number for CF response for the IL direction.

6. Calculate the stress standard deviation and use S-N curves to find the fatigue damage

The requirements for using this method are that the structure must have an uniform cross-section and the current must be unidirectional (DNV, 2010b).

Chapter 5

Method of analysis

The method is based on a simplified model that can easily be adapted to other riser designs. If the model can be applied to other riser configurations, the method can be verified and possibly be used in a standard.

The original plan was to create a fully parametric model, but was more difficult than anticipated. The reasons for this is because another software had to be introduced in order to properly describe the response of the drilling vessel. Further explanations of this are given later in the chapter. The geometry and the application of structural loads, are very simplified. The location of the riser is Gulf of Mexico, and the environmental loads corresponds to the metocean from this area.

Due to time limitations, one case-study has been investigated in the different analysis. Future studies will involve performing the methodology for several cases, where the input data will be selected based on the technical documentation presented in chapter 2.4 and the standards presented in chapter 4. The input data for the selected case are based on the information given in these chapters, and information from projects at Bureau Veritas given by Catalin Toderan (Toderan, 2016).

5.1 Geometry and design

The interface in SIMA/RIFLEX is similar to Flexcom. The marine drilling riser is built up by nodes and lines. The lines give information about the topology of the system and can be divided into segments. Each section is defined with a length and total number of elements per segment, as shown in figure 5.1. Cross-section dimensions, mass, hydrodynamic- and stiffness properties are defined for each segment of the line.

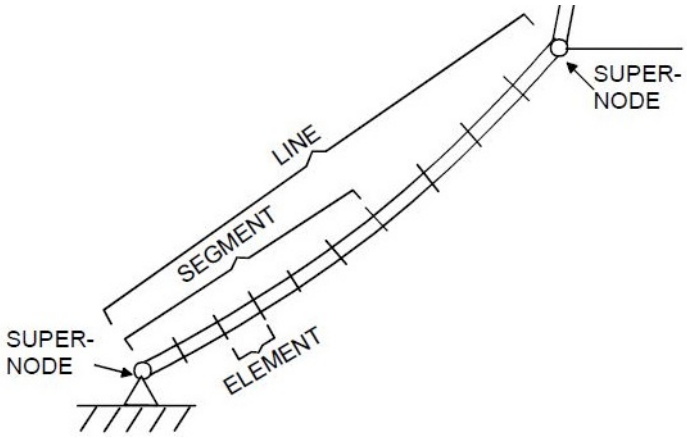

Figure 5.1: Riser set-up in SIMA/RIFLEX (MARINTEK, 2013)

The drilling riser in Flexcom is designed with one main line, which is divided into six different sections, as shown in table 5.1. The first column from the left indicates the order of the segments from the seabed to the water surface. The well is at the bottom of the seabed, and the telescopic joint at the water surface.

Order	Section	Length [m]
1	Well	2
2	BOP	15
3	LMRP	10
4	LFJ	2
5	Buoyancy joint	1978
6	Telescopic joint	3

Table 5.1: Topology of the riser and section lengths

The element length is defined with a minimum length and maximum length. The minimum and maximum lengths are set equal to 1m for all of the sections, expect for the buoyancy joint.

For the buoyancy joint the maximum element length is equal to 4.6m. This has been done in order to decrease the computational time in the different analysis. It is important to consider that the stiffness transition from one element in one segment, to an element in another segment when deciding the number of elements for each segment. In order to avoid numerical errors, the stiffness transition should not be larger than a factor of 2 (Sævik, 2016).

The coordinate system is defined in figure 5.2. Information from the other softwares used in this thesis, i.e. Arian, must correspond to the coordinate system in Flexcom. This has been verified before conducting the different analysis.

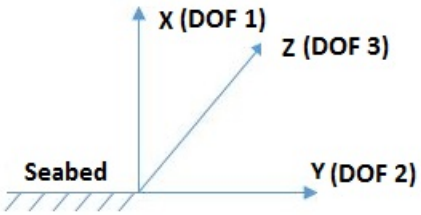

Figure 5.2: Coordinate system in Flexcom

5.1.1 Riser joints

Due to the increasing demand of deeper drilling operations, the length of the marine drilling riser is set equal to 2000m. The analysis in Flexcom is performed in sea water, with density of 1025kg/m^3. The buoyancy section is the longest section, and is the main focus in the global load, fatigue and VIV analysis. From the documentation in chapter 2.4, the best suited joint for deep water conditions is the LoadKing riser, designed by Cameron. The length of the joints are taken from API's recommended practice 16Q, which suggest lengths between 50ft to 75ft (API, 2010a). This is approximately 15m to 23m in the metric system. In order to select the proper length in this interval, the buckling phenomena has been considered.

The critical load of a member is defined in equation 5.1.

$$N_{cr} = \frac{\pi^2 EI}{l_e^2} \tag{5.1}$$

The effective length of the joint is proportional to the product of the actual length and a factor, K. The factor is based on the the boundary conditions of the member, as shown in figure 5.3.

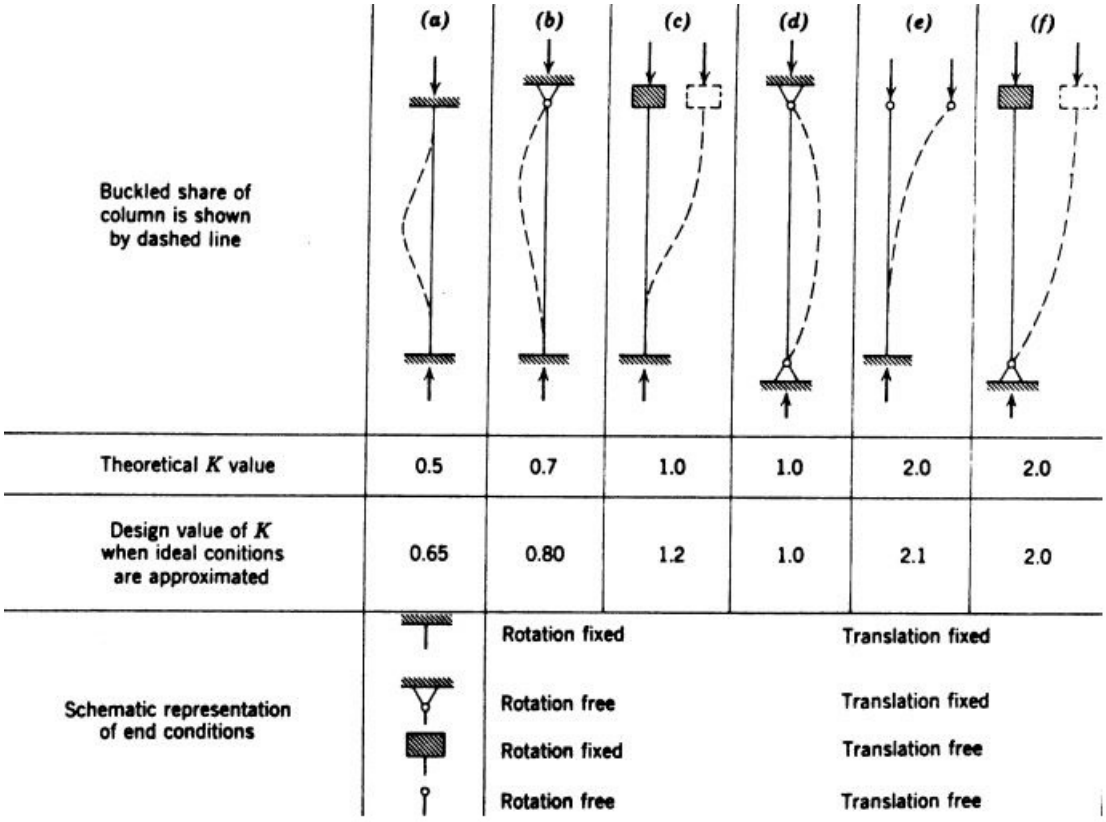

Figure 5.3: Effective length factor (Amdahl, J., 2014)

If the length increases, the effective length increases too. This will result in a lower critical load of the member, as shown in equation 5.1. Therefore, a conservative choice is to select the longest length in the interval presented in API RP 16Q (Amdahl, J., 2014). The buoyancy joints are therefore 23m long.

5.1.2 Cross-section properties

The cross-section dimensions for the buoyancy joint are shown in figure 5.4. An important consideration when selecting the dimensions of the main tube, is how the drill string will behave when the riser experience large displacements. In order to ensure that the drill string don't touch the tube, the inner diameter must be large enough. The inner diameter is therefore equal to 540mm and the outer diameter is 560mm. The buoyancy module thickness is 150mm, with foam density equal to 800 kg/m^3 (Toderan, 2016). The buoyancy modules are considered in Flexcom by the definition of the buoyancy diameter and the increase in the total mass from the foam mass.

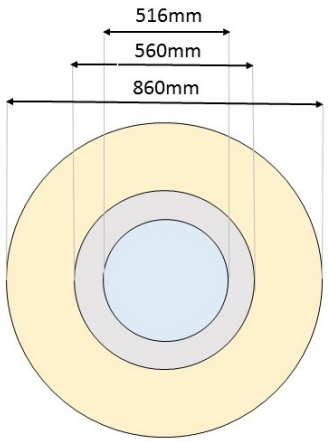

Figure 5.4: Cross-section dimensions

The buoyant joint is designed as a continuous joint with buoyancy modules attached to the main tube. In reality, the buoyancy modules are discrete parts attached to the riser joints, but a continuous module has been selected, since the model should be simplified. Information about foam densities from the industry are usually difficult to find. From the research of existing technology in chapter 2.4, Matrix Composites and Engineering provided more detailed information compared to the other companies. From table 2.1, the densities were between 400kg/m^3 and 500kg/m^3 for 2000m water depths. However, as mentioned in the chapter, these densities seems to be based on 75 inch joints and are therefore not applicable since the modules are continuous in Flexcom.

The cross-section is designed to accommodate four lines, which contributes to the total mass

with approximately 18.6% of the weight of the main tube. The connections contribute to 5% of the weight of the main tube and the lines, and is calculated based on 10% of the length of the joint (Toderan, 2016). Due to deep water conditions and the location of the riser, the HMF connection has been chosen to represent the connections in the model. The connections are added on one side of the joint, and are connected with pin/box flanges. The four lines are not visually designed in the model, but taken into account by the increase of weight per unit length. The connections are designed with point masses at every 23m of the buoyancy joint. The mass per unit length is the sum of the mass of the main tube, lines and buoyancy module, but not the drilling fluid. The drilling fluid is taken separately into account in Flexcom. The mass per unit length is in total 613kg/m. The buoyancy modules cover only the submerged part of the riser, which is 85 joints and partly the last joint. The weight of the buoyancy module for the last joint is 4283 kg. The mass calculations are shown in table 5.2.

Component	M air [kg]	M air w/fluid [kg]	Buoyancy [kg]
1 Joint (Main tube)	6714	12726	
4 Lines	1248	1248	
1 Buoyancy module	6156	6156	
Total (86 joints)	1214148	1726897	1173516

Table 5.2: Mass data for the marine drilling riser

5.1.3 Stiffness properties

The stiffness properties for the buoyancy joints are calculate based on the dimensions of the joint and the material properties for structural steel. The stiffness properties are shown in table 5.3.

Axial stif.[N]	Bending stif. [N/m^2]	Torsion stif.[Nm^2/rad]
7808617036	282992090	17007807

Table 5.3: Stiffness properties for the marine drilling riser

5.1.4 Riser components

A well, BOP and LMRP are located at the bottom part of the riser. The stiffness for these components are infinite, because the main focus is the buoyancy joint. The stiffness properties for the well, BOP and LMRP, are selected based on the stiffness of the buoyancy joint, multiplied with a factor of 1000. In order to validate that the components are infinite stiff, the bottom of the riser can be compared to a cantilever beam with a concentrated force at the end. If the displacement is close or equal to zero, the stiffness is assumed infinite.

A lower flex joint (LFJ) is located between the LMRP and the buoyant joint. The rotational stiffness of the joint is based on one the example model in Flexcom, which is 40675Nm/deg (Wood Group Kenny, 2015). Information about the rotational stiffness is very difficult to find from company sites. From the research of the existing technology in chapter 2.4, the angular deflection was often limited to ten degrees. The riser is however, often disconnected after two degrees because the drilling string will touch the inner wall of the riser tube and damage the tube (Toderan, 2016).

The telescopic joint is also designed with infinite stiffness for the same reason as explained for the well, BOP and LMRP. As mentioned in chapter 2.2, the purpose of the telescopic joint is to prevent damage of the riser when heave motions are present. The telescopic joint is usually modeled with an inner barrel and an outer barrel. The inner barrel has a low axial stiffness in order to for it to move inside the outer barrel (Sævik, 2016). The effect of the telescopic joint is not modeled in the simplified model. The reason for this is because the top tension is set so high that the riser will never be in compression. The effect of the heave motion of the ship will therefore be compressed by the high tension, and there is no need to model the effect. Since the telescopic joint is designed as a rigid element, there are possibilities that large moments will occur at the top of the riser. If this is the case, an upper flex joint (UFJ) should be considered in order to minimize the moment. The reason for creating a model with no UFJ, is because there exist configurations that don't have this component (Toderan, 2016). Figure 5.5 shows to the left the simplified model analyzed in Flexcom, and to the right a complex design of a marine drilling riser.

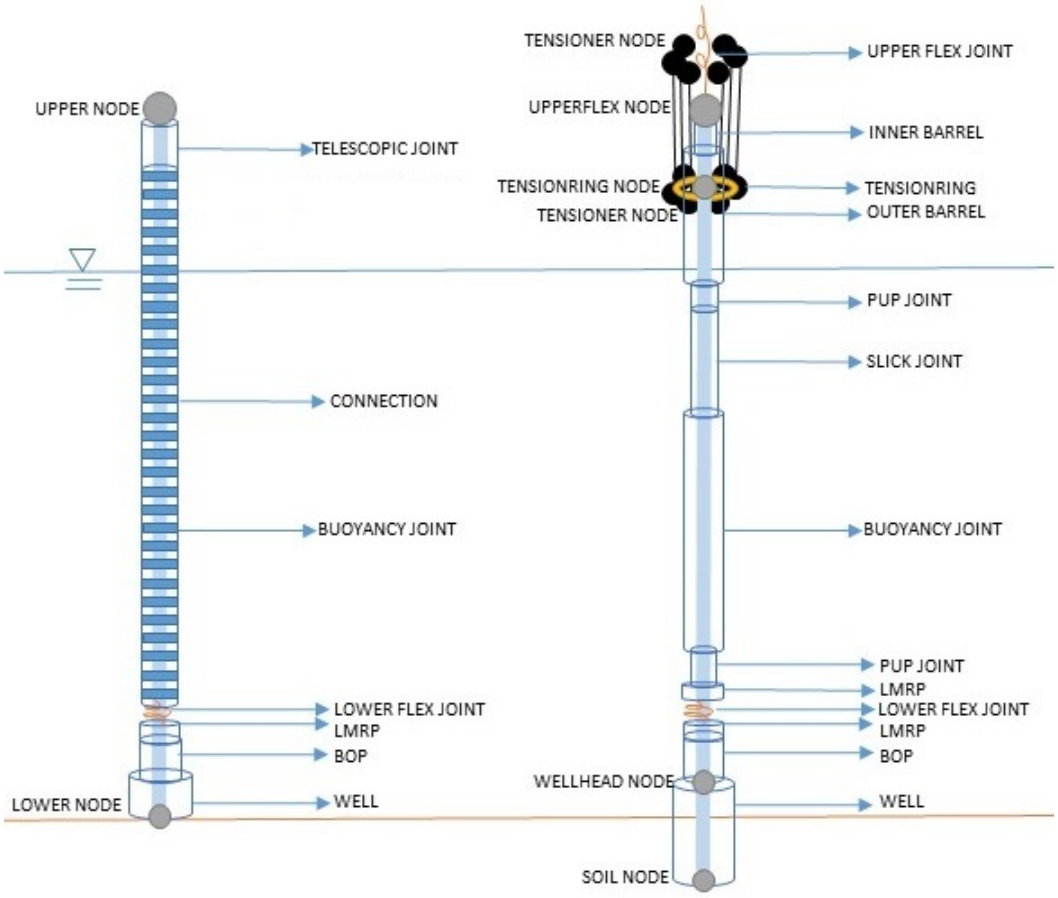

Figure 5.5: The marine drilling riser analyzed in Flexcom

The boundary conditions applied to the model, have been discussed and investigated in the analysis. Since the main focus is the buoyancy joint, the riser is fixed in all translations and rotations at the seabed. According the *Report for JIP structural well integrity* from DNV, the boundary conditions should be designed with a beam and a spring with non-linear stiffness at the seabed. The soil node should have pinned boundary conditions (DNV, 2011b). Figure 5.6, shows the suggested design. This model has not been considered, as it is developed for wellhead fatigue. However, according to the rules, presented in chapter 4, if the BOP, LMRP and wellhead are part of the model, a rotational spring from soil interaction should be modeled. The topic is however debatable, because the casing is not included, and the standard suggest these boundary conditions when the casing is included (API, 2010a).

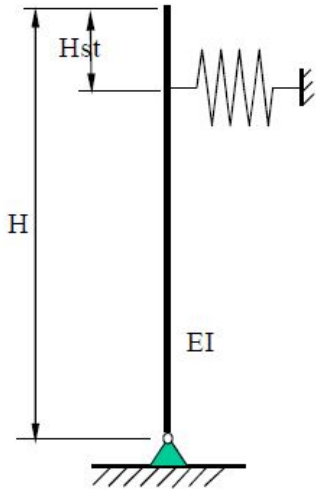

Figure 5.6: Boundary conditions at the seabed (DNV, 2011b)

The boundary conditions at the top of the riser were more challenging to define. The reason for this is because the tensioner system allows some displacement of the riser, but since it is not designed in the model the effect must be considered somewhere else. One option of adding three springs, each representing one translation, was considered. This became however challenging, because the riser would then have a relative velocity to the vessel. The displacements from the tensioner system were therefore neglected. The assumption is possibly correct, because the vessel has a dynamic positioning system (DP) that contributes more to the displacements than the tensioner system. The boundary conditions at the top of the riser included therefore the second order vessel motions from the DP system. Further discussions about the top boundary conditions and the final design, can be found in chapter 5.3and chapter 6.

5.1.5 Hydrodynamic properties

The hydrodynamic force coefficients for the marine drilling riser are found in the *Report for JIP structural well integrity* and are equal to 1.0 for the drag 2.0 for the inertia for all the components of the riser (DNV, 2011b). The coefficients are added to the entire riser, but they only affect the submerged part of the structure.

5.1.6 Top tension

Tension in the drilling riser is necessary in order to avoid buckling. The top tension is usually applied through the tenisoner lines in the tensioner system, but since the model is simplified the system has not been designed. The top tension has been applied by a concentrated force at the top of the riser head in the vertical direction.

In order to find the necessary top tension, the total weight of the riser, including the weight of the connections, choke- and kill lines, buoyancy modules and drilling fluid, have been added together. The drilling fluid can either water based or oil based, but in order to represent the worst case, the fluid that contributed most to the weight was selected in the analysis. The worst case was the water based fluid. The total buoyancy has been calculated and equilibrium between the total weight, buoyancy and applied top tension, was found.

The different lengths of the riser components and joints are given in table 5.1. The submerged length of the total buoyancy joint is 1971 m, which is 85,7 number of joints. This means that 16 m of the last buoyancy joint, of 86 joints in total, is submerged. The remaining part is not submerged, and has therefore, not been taken into account in the total buoyancy force.

The top tension applied to the model was selected from standardized values, and the necessary top tension was found through an iteration process. When the riser experienced compression, the top tension was increased. Another option was considered before increasing the top tension, and that was to reduce the diameter and thickness. However, since the risk of damage would be high because the drill string could touch the inner wall of the pipe, the top tension was increased instead.

The initial top tension applied to the model, was 250 tonnes. This gave a large compression force at the bottom of the riser. In order to find where the compression occurred, a new iteration process was conducted. By calculating the force joint by joint, it was discovered that compression occurred at the 47,51 joint from the LFJ. This is equivalent to 1093m. This resulted in a critical load equal to 2339N. By taking the average of the compression force at the bottom, the Euler buckling force was equal to 1499903N. Calculations from the iteration process and buckling problem are given in appendix B. The results from the buckling calculations showed clearly that the member would buckle. A new top tension was therefore applied in order to avoid buckling. The top tension was increased to 600 tonnes. Even though the required top tension for obtaining equilibrium at the bottom of the buoyancy joint was smaller than 600 tonnes, a top tension of 600 tonnes was selected because standardized values was required. The second choice of top tension resulted in a positive force at the bottom of the buoyancy joint, equal to 44 tonnes. The top tension calculations can be found in appendix A.

5.2 Environment

The Gulf of Mexico was selected for the the location of the riser. GoM has experienced large environmental changes over the years, which has made it challenging to design and operate offshore structures.

5.2.1 Gulf of Mexico

In the 1940s, there were few regulations and no API guidance on how to design structures in the GoM. There were only small hurricanes in the area until the Freeport platform was hit by almost 40ft waves, in 1949. Almost ten years later, new storms developed and became more sudden compared to previous storms.

Over the next decade GoM was mostly affected by tropical storms, an one of them, hurricane Hilda, destroyed 13 oil platforms in 1964. One year later, hurricane Betsy destroyed additionally eight more platforms. This led to a committee that began to collect ocean data to calibrate

hindcast models, and in 1969 the first API offshore standard was issued. Over the following years more hurricanes in larger dimensions appeared, which led to improvements of the standard.

In the beginning of 2000 hurricane Ivan, Katrina and Rita appeared in the GoM from loop currents and eddies. This discovery led to a division of the Gulf, as shown in figure 5.7 (Berek, 2016).

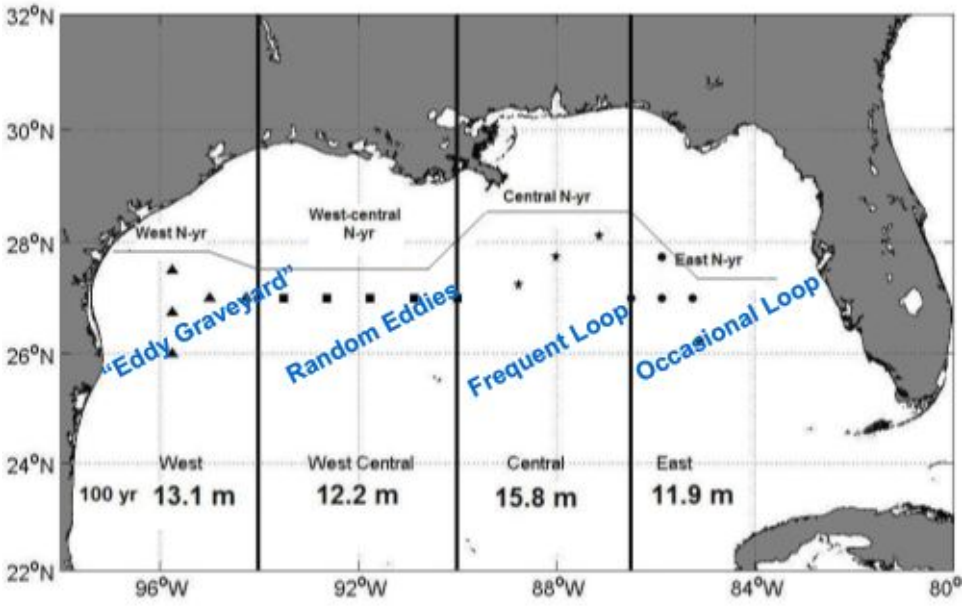

Figure 5.7: Regions in the GoM (Berek, 2016)

Due to the unpredictable changes in the GoM, it is difficult to create standards for the area. It is therefore of interest to locate the riser in this area, in order to create a methodology than can hopefully minimize the damage to the structure.

5.2.2 Support vessel

Two choices were considered when selecting the drilling vessel, a semi-submersible and a drilling ship. Since part of the analysis was conducted in Ariane, and data for a semi-submersible from HydroStar was available, the semi-submersible was selected to represent the drilling vessel in the analysis. First order wave motions for the vessel, are given by response amplitude operators (RAO). The vessel has a dynamic positioning system with a limiting condition of 20 m offset. The vessel is therefore allowed some displacement, which is transferred over to the riser head. The displacement from the DP system is assumed to have an impact on the fatigue life of the riser, and the second order drift motions from the vessel, are therefore considered in the analysis. The riser's effect on the vessel is neglected.

In order to take the DP system into account in Flexcom, the displacement from the vessel, due to low frequency motions, have been calculated with Ariane. Ariane is a mooring software, developed by Bureau Veritas, which performs static and time domain simulations on the mooring system. The Ariane software has in earlier versions, only been used for mooring lines. However, in the version released in October 2015, a DP module was added in the software (Bureau Veritas, 2015a). Because of this there has been limited of time to gain experience with this module, and the methodology had to be developed during this thesis. Mooring engineer, Martin Dumont, from the marine and offshore division at Bureau Veritas, performed the calculations in Ariane and developed the methodology for the DP system. The general outline of the methodology is presented below.

The DP module is based on a basic diagram of operating DP systems however, only a few components are implemented in the software and these are listed below.

- GPS & gyro: Measurement device for the vessel's position
- Anemometer: Measurement device for the vessel's wind speed by use of wind models
- Model algorithm: Gives the low-frequency (LF) positions and speeds of the vessel and calculates the LF forces. The required inputs are the hydrodynamic model and global vessel position, including both wave frequencies (WF) and LF.
- Control method: Determines the control demand for obtaining zero deviation from the

position of the vessel and the setpoint. The setpoint is the desired location of the vessel during DP operations. The required input is the model algorithm.

- Thruster allocation algorithm: Determines the angle and force needed to fulfill the control demand. The required inputs are the control demand and thruster configuration.

The DP control panel from Ariane is shown in figure 5.8. The figure shows the DP system parameters tab. Additionally, there are two more tabs called setpoint and thrusters arrangement. The "Ariane simulator" gives the true behavior of the system when the DP system is in operation, and the "Update time step factor" multiplies the time step in Ariane with the time step from the DP, in order to get the correct time step when performing time domain simulations.

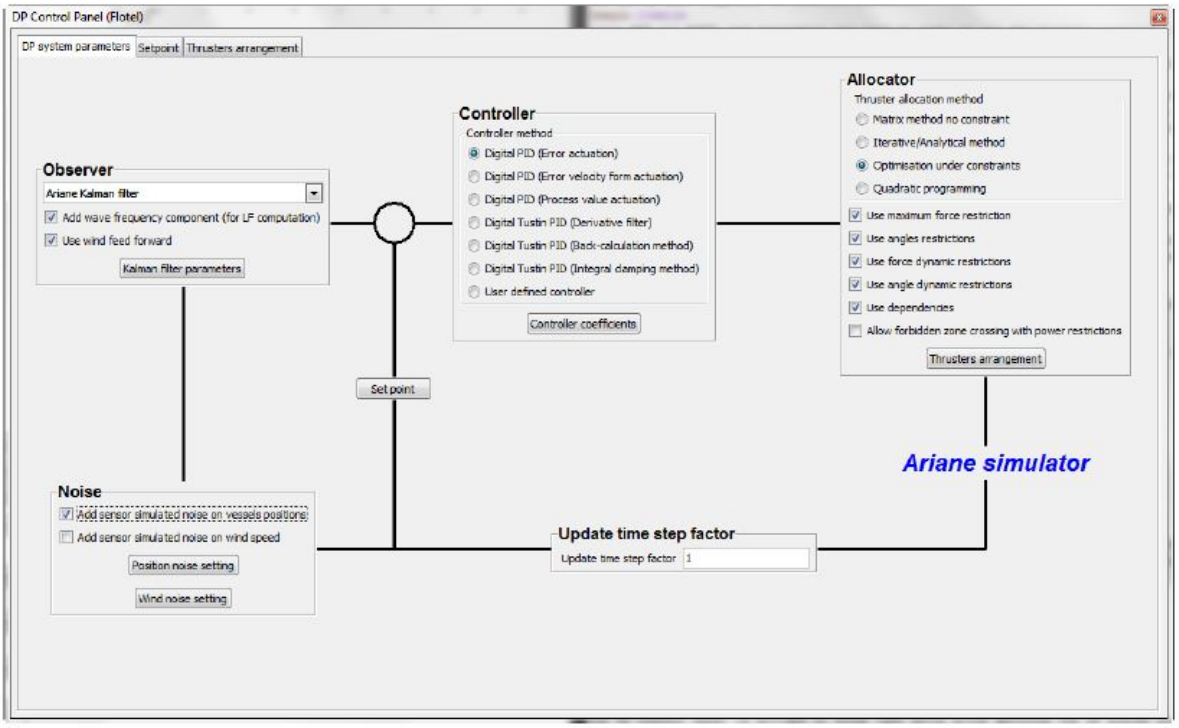

Figure 5.8: DP control panel in Ariane (Bureau Veritas, 2015a)

The parameters tab shows two calculation loops, but only the right sided loop was used to obtain the time series from the LF motions. The controller calculates the required thrust to get to the setpoint with one of seven different methods. In order to tune the DP, so that it fulfilled the limiting condition of 20m offset, an iteration process was performed for the "Error actuation method". This included changing the controller coefficients, shown in figure 5.9.

The allocator distributes the control demand for each thruster with one of four methods, and six thruster constraints. The "Optimization under constraints" was used with five constraints in order to tune the DP system. This included restricting the maximum force and angle for the thrusters, restricting the force dynamic rates and angle dynamic rates and including dependencies between the thrusters.

Figure 5.9 shows the controller coefficients from the controller option in the loop. These parameters were the only variables in the iteration process for tuning the DP system (Bureau Veritas, 2015a).

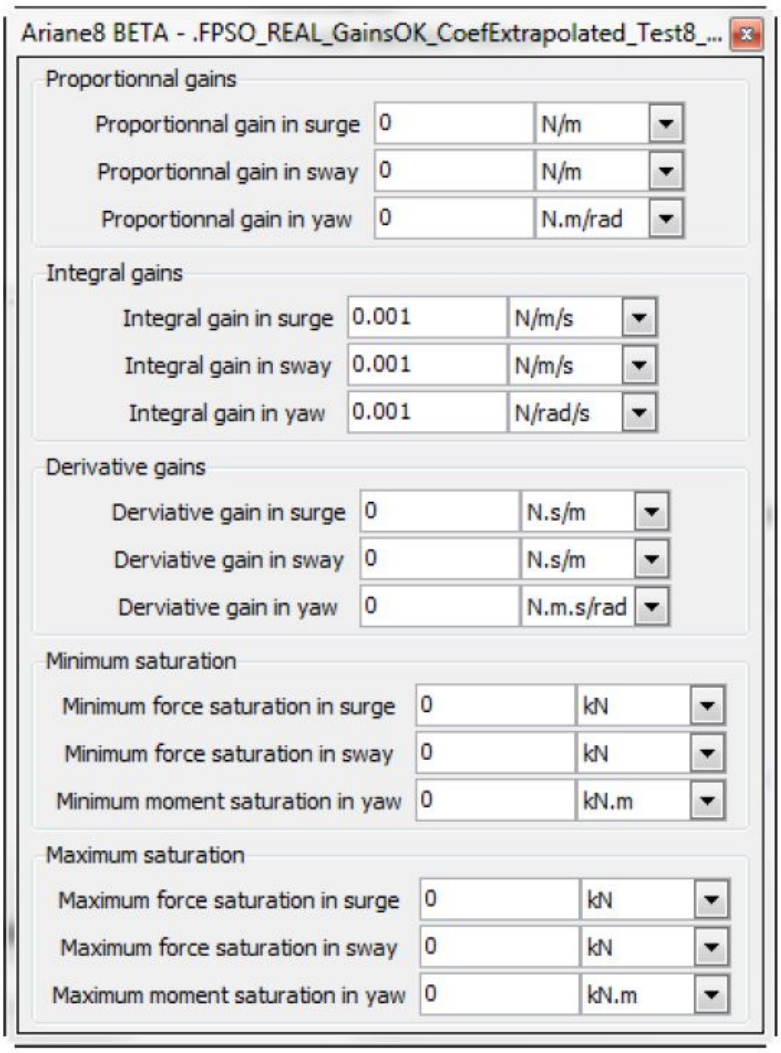

Figure 5.9: Controller coefficients in Ariane (Bureau Veritas, 2015a)

The input data in Ariane were obtained from another software from Bureau Veritas, called HydroStar. HydroStar is a seakeeping software that evaluates responses of the vessel, first-order solutions, added mass and damping matrix, diffraction forces and Froude-Krylov loads, LF loads, wave fields and pressure distributions around the ship. It also takes forward speed into account. In order to solve the hydrodynamics problem, i.e. calculate the added mass, radiation damping and diffraction forces, input data of the frequencies, headings, water depth and speed must be given. The hydrodynamics problem is solved by dividing it into a radiation problem and a diffraction problem. The radiation problem is defined by a moving body in still water, while the diffraction problem is defined by a fixed body in waves. When the hydrodynamics problem is solved, the motion equation can be solved. The solution of the equation of motion gives the RAOs. In addition to first order loads, Hydrostar also calculates second order loads. The second order loads consist of drift forces, QTF in mode summation and QTF in mode difference (Monroy, 2015). QTF stands for quadratic transfer function (Faltinsen, 1998). Sine a semi-submersible was selected for the analysis, and a DP system was selected for the mooring system, the natural period is long, which means that the drift forces and QTF in mode difference are the relevant forces to consider in the analysis in Ariane. The results obtained with HydroStar are the input values in Ariane.

In addition to the information from Hydrostar, the environmental data had to be defined in Ariane. The environmental data were defined in a batch script, shown in figure 5.10. The column from left in figure 5.10, gives the peakedness parameter. The following columns gives the standard deviation, significant wave height, peak period, minimum frequency and maximum frequency, wave heading, seed, harmonic waves, wind surface speed, wind heading, current surface velocity and current heading. The parameters are discussed in chapter 5.2.3, 5.2.4 and 5.2.5.

```
wavemodel:
Jonswap
windmodel:
Constant
currentmodel:
Constant
batch:
gamma   sigma   sigma   Hs      Tp      min fq  max fq         wave    seed     #      wind  wind    current  current
3.3     0.07    0.09    6.0     3.5     0.01    0.286479        0       0       200     22.5    0       1.13    0
3.3     0.07    0.09    6.0     4.5     0.01    0.286479        0       0       200     22.5    0       1.13    0
3.3     0.07    0.09    6.0     5.5     0.01    0.286479        0       0       200     22.5    0       1.13    0
3.3     0.07    0.09    6.0     6.5     0.01    0.286479        0       0       200     22.5    0       1.13    0
3.3     0.07    0.09    6.0     7.5     0.01    0.286479        0       0       200     22.5    0       1.13    0
3.3     0.07    0.09    6.0     8.5     0.01    0.286479        0       0       200     22.5    0       1.13    0
3.3     0.07    0.09    6.0     9.5     0.01    0.286479        0       0       200     22.5    0       1.13    0
3.3     0.07    0.09    6.0     10.5    0.01    0.286479        0       0       200     22.5    0       1.13    0
3.3     0.07    0.09    6.0     11.5    0.01    0.286479        0       0       200     22.5    0       1.13    0
3.3     0.07    0.09    6.0     13.5    0.01    0.286479        0       0       200     22.5    0       1.13    0
3.3     0.07    0.09    6.0     14.5    0.01    0.286479        0       0       200     22.5    0       1.13    0
3.3     0.07    0.09    6.0     15.5    0.01    0.286479        0       0       200     22.5    0       1.13    0
3.3     0.07    0.09    6.0     16.5    0.01    0.286479        0       0       200     22.5    0       1.13    0
3.3     0.07    0.09    4.0     3.5     0.01    0.286479        0       0       200     22.5    0       1.13    0
3.3     0.07    0.09    4.0     4.5     0.01    0.286479        0       0       200     22.5    0       1.13    0
3.3     0.07    0.09    4.0     5.5     0.01    0.286479        0       0       200     22.5    0       1.13    0
3.3     0.07    0.09    4.0     6.5     0.01    0.286479        0       0       200     22.5    0       1.13    0
3.3     0.07    0.09    4.0     7.5     0.01    0.286479        0       0       200     22.5    0       1.13    0
3.3     0.07    0.09    4.0     8.5     0.01    0.286479        0       0       200     22.5    0       1.13    0
3.3     0.07    0.09    4.0     9.5     0.01    0.286479        0       0       200     22.5    0       1.13    0
3.3     0.07    0.09    4.0     10.5    0.01    0.286479        0       0       200     22.5    0       1.13    0
3.3     0.07    0.09    4.0     11.5    0.01    0.286479        0       0       200     22.5    0       1.13    0
3.3     0.07    0.09    4.0     12.5    0.01    0.286479        0       0       200     22.5    0       1.13    0
3.3     0.07    0.09    2.0     2.5     0.01    0.286479        0       0       200     22.5    0       1.13    0
3.3     0.07    0.09    2.0     3.5     0.01    0.286479        0       0       200     22.5    0       1.13    0
3.3     0.07    0.09    2.0     4.5     0.01    0.286479        0       0       200     22.5    0       1.13    0
3.3     0.07    0.09    2.0     5.5     0.01    0.286479        0       0       200     22.5    0       1.13    0
3.3     0.07    0.09    2.0     6.5     0.01    0.286479        0       0       200     22.5    0       1.13    0
3.3     0.07    0.09    2.0     7.5     0.01    0.286479        0       0       200     22.5    0       1.13    0
3.3     0.07    0.09    2.0     8.5     0.01    0.286479        0       0       200     22.5    0       1.13    0
3.3     0.07    0.09    2.0     9.5     0.01    0.286479        0       0       200     22.5    0       1.13    0
3.3     0.07    0.09    2.0     10.5    0.01    0.286479        0       0       200     22.5    0       1.13    0
```

Figure 5.10: BATCH script

Three combinations of headings were considered in the script, i.e. 0, 45 and 90 degrees. The type of headings were wind, wave and current. The batch script in figure 5.10, shows one combination of headings, where the wave, wind and current are applied in the same direction, 0 degrees. Since it is difficult to predict the combination that contribute most to the fatigue damage, all combinations should be investigated in the different analysis. For future studies, more directions could also be investigated in order to cover all possible outcome.

Each line in the script represents one case, and each case is described with a time history from Ariane. In total, the batch script gives more than 500 time histories. The time histories are given in scripts, and contain displacements in three DOFs relating to a specific time. These scripts must be edited in order for Flexcom to read them. This includes removing all information which is not relevant to Flexcom. In addition, the vertical DOF can be removed, because it is assumed that the top tension is large enough to prevent vertical displacement of the riser.

5.2.3 Wave

The irregular wave environment is created with 200 harmonics from a frequency range between 0.01 and 0.29 from a 3-parameter JONSWAP spectrum. The reason for selecting this frequency range is because it ensures that all relevant frequencies are taken into account from 5% of the spectrum's left side, and 95% of the spectrum's right side. The number of harmonics must be large enough in order to create a fully irregular environment. A total number of 200 harmonic waves has proven to be sufficient enough for achieving this. If the amount of harmonics are more than 200, the computational time will increase (Dumont, 2016). The seed number is set equal to zero for all sea states. This means that for each simulation, the wave time series will vary. If the seed number is larger than zero, the time series would be reproduced from each simulation (Bureau Veritas, 2015a).

The spectrum is defined by a significant wave height, peak period and a spectral peakedness parameter. The standard deviation depends on whether the peak wave frequency is smaller or larger than the wave frequency, as explained in chapter 3.3.2. The definition of the peakedness parameter is given in equation 3.68, and varies with the significant wave height and the peak period. In the analysis, the parameter is set constant to 3.3 for all sea states because the change in the parameter from sea state to sea state is assumed to have no effect on the result (Dumont, 2016).

The scatter diagram is given by Bureau Veritas and represent extreme conditions for the GoM (Bureau Veritas, 2016a). The drilling operation is limited by 6m significant wave heights because the riser could be damaged if the wave height becomes higher (Toderan, 2016). When the waves are higher than 6m, the riser will disconnect from the vessel and the drilling operation will stop. The sea states below this limit are selected from the scatter diagram, and used in the analysis in Ariane. Table 5.4, gives an overview of the selected sea states. The total probability of occurrence is 86.4%, and the probability for each sea state is calculated based on total number of waves, 254232.

Sea state	Hs [m]	Tp [s]	Probability	# waves
0	6	3.5	0.00009	23
1	6	4.5	0.00249	632
2	6	5.5	0.05630	14312
3	6	6.5	0.08579	21811
4	6	7.5	0.04746	12066
5	6	8.5	0.00613	1558
6	6	9.5	0.00057	145
7	6	10.5	0.00015	39
8	6	11.5	0.00006	14
9	6	13.5	0.00001	2
10	6	14.5	0.00001	3
11	6	15.5	0.00001	2
12	6	16.5	0.000004	1
13	4	3.5	0.01635	4157
14	4	4.5	0.12587	32001
15	4	5.5	0.22149	56309
16	4	6.5	0.08610	21889
17	4	7.5	0.01585	4029
18	4	8.5	0.00583	1483
19	4	9.5	0.00190	482
20	4	10.5	0.00033	83
21	4	11.5	0.00006	14
22	4	12.5	0.000004	1
23	2	2.5	0.00136	347
24	2	3.5	0.04767	12119
25	2	4.5	0.07084	18010
26	2	5.5	0.04427	11254
27	2.5	6.5	0.00489	1244
28	2	7.5	0.01466	3726
29	2	8.5	0.00649	1651
30	2	9.5	0.00114	291
31	2	10.5	0.00007	19

Table 5.4: Sea states below the limiting condition

5.2.4 Wind

A wind spectrum must be defined for the analysis in Ariane. The reason for this is because the vessel is affected by the wind, which challenges the DP system to stay in position. The wind spectrum is constant with surface velocity of 22.5m/s. The combinations of the wind in the batch script were considered to be removed for the analysis in Flexcom. The reason for this was because wind is less important since the main focus is the submerged structure. If the wind

combinations were to be removed, there would be several cases with the same combination of wave and current headings. By removing these cases, the total computational time would decrease significantly. However, the time series from Ariane would not be the same for these cases, because the wind would change the time series. In order to investigate all possibilities, the time series, which also include the wind combinations, should be considered in the analysis in Flexcom.

5.2.5 Current

The current is based on a combination of the metocean report given by Bureau Veritas (Bureau Veritas, 2016a), and the API standard *Interim Guidance on Hurricane Conditions in the Gulf of Mexico* (API, 2007). The current velocity at the surface in the metocean report, is for extreme conditions, and gives a surface velocity 1.5m/s (Bureau Veritas, 2016a). This velocity is too high for drilling operations, and the riser would disconnect from the vessel (Toderan, 2016). The API standard is also for extreme conditions, but the surface velocity is instead 1.13 m/s (API, 2007). This velocity is more reasonable for drilling operations, and is therefore used in the analysis (Toderan, 2016). The current profile is selected from the metocean report and is given in table 5.5. The profile is for 1000m, which means that the current at 2000m will zero.

Depth [m]	Current [m/s]
0	1.130
25	1.130
50	1.125
75	1.027
100	0.871
125	0.768
200	0.572
300	0.403
400	0.311
500	0.245
600	0.197
700	0.170
750	0.158
800	0.137
900	0.071
1000	0

Table 5.5: Current profile

5.3 Global load analysis

There are two types of analysis required in a global load analysis, a static analysis and a dynamic analysis. The methodology for the global load analysis in Flexcom is created through a series of steps. Each step is performed in order to investigate possible outcomes from theories and assumptions discussed during the master thesis work.

After creating the model according to the information given in chapter 5.1, the static analysis was set up. The example model in the Flexcom software was used as a reference model to check how the different analysis could be constructed. Each analysis consists of a pre-processor and a post-processor. The pre-processor for the static analysis consists of the defined parameters, the model and the different load cases. The loads include the boundary conditions and applied loads, such as the top tension, the point masses and the internal fluid. The type of analysis is defined at the same place as the loads. The static analysis is defined with a total analysis time of one second, with a fixed time step of 0.1.

A separate analysis was created for the current. The static analysis included originally the current, but this led to error messages, which was solved when the current was run in a separate analysis. The current analysis restarts from the static analysis and runs for one second with a time step of 0.01. The dynamic analysis restarts therefore from the current analysis, and has a variable time step with a minimum value of 0.0001 and maximum 0.2. The analysis must run long enough for the solution to reach steady-state. The fatigue analysis should therefore run for one hour (Sævik, 2016). The loads are normally transferred from the static analysis when the dynamic analysis restarts from the static. However, it was discovered that Flexcom sometimes disregarded some of the loads defined in the static analysis, i.e. top tension and boundary conditions. These loads were therefore redefined in the dynamic analysis.

The first step in the global load analysis was to investigate the response from a simplified representation of the displacement from the DP system. At the time it was unsure if it was possible to incorporate a DP system with limiting condition of 20m in Ariane. This was because the DP module in Ariane had recently been released, and the module had never been used at Bureau Veritas.

The simplified drift motions were represented by a harmonic motion in y-direction. This motion was added as a sinusoidal boundary condition at the top node of the riser. The harmonic motion should had been added in the z-direction in order to properly describe the second order drift motions from the vessel, but this would give a circular motion, or a motion in the same pattern as the sign infinity (∞), depending on the phase of the wave. It was therefore decided that only one harmonic motion should be added to the top node, and the translation in z-direction should be fixed. For the x-direction it was not possible to fix the translation in this direction, because of the applied top tension.

The rotational boundary conditions were investigated in fixed condition and in free condition. The reason for investigating the boundary conditions was because of the simplified tensioner system in the model. In reality, the tensioner system allows some rotation of the riser, and by fixing them the response would be incorrect. Freeing them would also be incorrect, because the tensioner system would prevent some of the rotation. In order to obtain the correct response, the tensioner system should be modeled. The results from the boundary condition check is given in chapter 6.1.

A harmonic motion is described with an amplitude, phase and frequency. Since the limiting condition of the DP system was 20m, the amplitude was set equal to 10m. The period was set equal to 100s in order to represent the slow drift motion (Sævik, 2016). The phase was set equal to zero. In addition to the harmonic motion, a current was applied to the model. The current was applied at 0 degrees, 45 degrees and 90 degrees. The purpose of adding a current was to investigate the critical spots on the riser. There were no waves added to the model in this analysis. The reason for this was because of problems with the phase angle between the harmonic motion and the waves. This is discussed more thoroughly later in the chapter. The results from the analysis with different current directions are presented in chapter 6.1.

After performing the two first checks, the harmonic motion was replaced with the time histories from Ariane. The motions were added in a file input option for the boundary conditions for the vessel. The input file consisted of displacement in three translations, but only the motion in z and y-direction, DOF 2 and 3, were added to the model. These motions consisted of both LF and WF motions. The results from this analysis are given in chapter 6.2.

In the previous analysis, loads from waves acting on the top part of the riser, were neglected. Wave frequencies were only considered as a motion at the top node of the riser. The reason for not taking waves into consideration was because it was assumed that they would have little effect on the riser because of the deep water depth. However, by neglecting the wave kinematics at the top part of the riser the result could be incorrect. The reason for this is because waves give velocities which is used in the Morison's equation to calculate the drag loads. Drag loads are particularly important for slender structures, and should therefore not be disregarded.

In order to investigate the importance of wave loads on the model, a regular wave was added to the model. The model had now contribution from LF and WF motions from Ariane, current loads and wave loads. The current was applied in the same direction as the direction which was used to obtain the time history from Ariane. Adding a regular wave to a model that have irregular motions from Ariane is however not correct. In addition, the phase angle between the wave frequency motion at the top node of the riser, and the regular wave would also not be correct. However, a regular wave was chosen because it has a higher amplitude, which makes it easier to see the contribution from the waves. The results from this analysis is shown in chapter 6.2.

From the results, it was decided that waves should be included in the analysis however, the waves had to be applied correct. Therefore, new time histories were obtained from Ariane which only included LF motions. The LF motions were added to the top node of the riser, and the wave kinematics were included by adding a JONSWAP 3-parameter spectrum in the analysis, and RAOs for the vessel. The motion from the time histories were added through a file input option for the drift motions. The motion was added to the second and third DOF, which represents the y and z-direction. In order for the riser to be attached to vessel and for the vessel to intake the motions, the displacement in the second and third DOF had to be fixed in the vessel boundary condition option.

Another option of the application of waves was also considered. This option included adding a separate input file from Ariane with just the WF time histories in Flexcom, in addition to the input file for the LF motions. The thought was that since the time series in Ariane were obtained by multiplication of the wave spectrum with the RAOs, the option of adding an input file

of the WF motions would be the equivalent to adding a wave spectrum and RAOs in Flexcom. However, after discussion with Yann Giorgiutti and Guillaume De Hauteclocque from Bureau Veritas, it was concluded that the time series from Ariane does not contain enough information for calculating the drag loads on the top part of riser. This method could therefor not be used.

By selecting the option of RAOs and wave spectrum, in addition to the drift motions from Ariane, the phase angles would still not be correct. From the discussion with Giorgiutti and and De Hauteclocque it it was concluded that the phase angles obtained from discretization of the JONSWAP spectrum in Flexcom would be different than the phase angles from the discretization of the spectrum in Ariane. This means that the phase between the WF motions from the combination of spectrum and RAOs in Flexcom, would not be coupled with the LF motions from Ariane. If the amplitudes and phases from discretization of the spectrum from Ariane could be inserted into the analysis in Flexcom, this issue could be solved. However, it was assumed that the contribution from the wave kinematics would impact more the fatigue life, and the phase problem has therefore been neglected.

Additionally, according to Bureau Veritas rules, the assumption of decoupled LF and WF motions can be justified if the mooring system's natural period is more than five times larger than the zero-upcrossing period (Bureau Veritas, 2015b). In order to check this, a small test has been conducted in the Ariane analysis. In the test the vessel was moved 40m from the initial position. By investigating how long time it took for the vessel to go back to the initial position, with no contribution from the environment, the natural period was found. The natural period can been seen from figure 5.11, obtained from the analysis in Ariane. The y-axes shows the offset of the vessel, and the x-axes shows the period. From the figure it can be observed that the system has little oscillation, and it is therefore a little challenging to find the exact period. The natural period for graph 0 is a little bit over 300s, and for graph 1 around 200s. The zero-upcrossing period is found from the scatter diagram, and is given in table 5.4. The highest period from the table is 16.5s, which gives 82.5s when it is multiplied with five. Since 85.5s is lower than both 200s and 300s, it can be concluded that the assumption regarding decoupled LF and WF motions is correct.

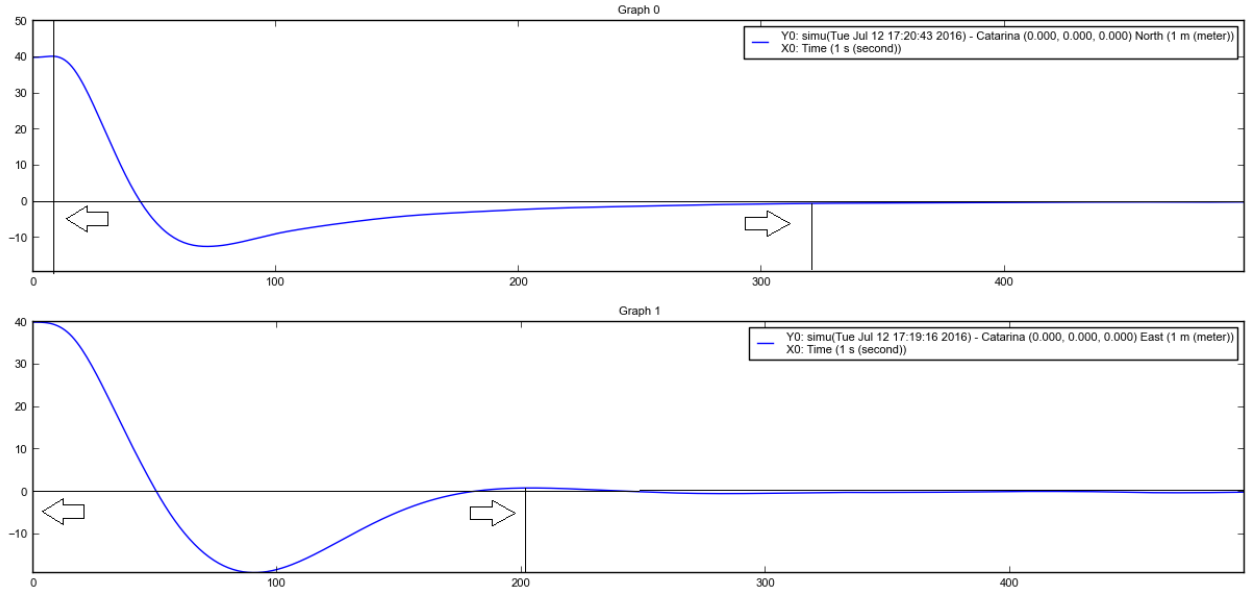

Figure 5.11: Natural period of the vessel with DP

The RAOs used in the Flexcom analysis needed to be converted in order for Flexcom to read them, and a lot of the time was used to convert these correctly for wave heading 0, 45 and 90. The example file and manual from Flexcom was used as reference for the conversions. Part of the RAOs from Ariane are shown in figure 5.12 and the format required in Flexcom is given below (Wood Group Kenny, 2015).

HEADING=Wave Heading

Wave Frequency

Heave RAO, Surge RAO, Sway RAO, Yaw RAO, Roll RAO, Pitch RAO

Heave Phase, Surge Phase, Sway Phase, Yaw Phase, Roll Phase, Pitch Phase

```
first_order_motions_data:
frequencies:
0.01    0.02    0.03    0.04    0.05    0.06    0.07    0.08    0.09    0.1     0.11    0.12
0.13    0.14    0.15    0.16    0.17    0.18    0.19    0.2     0.21    0.22    0.23    0.24
0.25    0.26    0.27    0.28    0.29    0.3     0.31    0.32    0.33    0.34    0.35    0.36
0.37    0.38    0.39    0.4     0.41    0.42    0.43    0.44    0.45    0.46    0.47    0.48
0.49    0.5     0.51    0.52    0.53    0.54    0.55    0.56    0.57    0.58    0.59    0.6
0.61    0.62    0.63    0.64    0.65    0.66    0.67    0.68    0.69    0.7     0.71    0.72
0.73    0.74    0.75    0.76    0.77    0.78    0.79    0.8     0.81    0.82    0.83    0.84
0.85    0.86    0.87    0.88    0.89    0.9     0.91    0.92    0.93    0.94    0.95    0.96
0.97    0.98    0.99    1.0     1.01    1.02    1.03    1.04    1.05    1.06    1.07    1.08
1.09    1.1     1.11    1.12    1.13    1.14    1.15    1.16    1.17    1.18    1.19    1.2
1.21    1.22    1.23    1.24    1.25    1.26    1.27    1.28    1.29    1.3     1.31    1.32
1.33    1.34    1.35    1.36    1.37    1.38    1.39    1.4     1.41    1.42    1.43    1.44
1.45    1.46    1.47    1.48    1.49    1.5     1.51    1.52    1.53    1.54    1.55    1.56
1.57    1.58    1.59    1.6     1.61    1.62    1.63    1.64    1.65    1.66    1.67    1.68
1.69    1.7     1.71    1.72    1.73    1.74    1.75    1.76    1.77    1.78    1.79    1.8

headings:
0.0     15.0    30.0    45.0    60.0    75.0    90.0    105.0   120.0   135.0   150.0   165.0
180.0   195.0   210.0   225.0   240.0   255.0   270.0   285.0   300.0   315.0   330.0   345.0
360.0

reference point:
cog

wave reference point:
cog

raos:

68.3283 270.0   0.0     0.0     0.9999  0.0     0.0     0.0     0.0399  270.0   0.0     0.0
34.1341 270.0   0.0     0.0     0.9997  0.0     0.0     0.0     0.0799  270.0   0.0     0.0
22.7226 270.0   0.0     0.0     0.9992  0.0     0.0     0.0     0.12    270.0   0.0     0.0
17.0069 270.0   0.0     0.0     0.9987  0.0     0.0     0.0     0.1603  270.0   0.0     0.0
```

Figure 5.12: RAOs from Ariane

The RAOs were first converted according to the example file in Flexcom. However, this resulted in non-converging analysis. Several checks were performed in order to find why the analysis did not converge. After thorough investigation, it was discovered that RAOs were defined incorrectly according to the Flexcom manual. Since the example model in Flexcom converged perfectly with the other definition of the RAOs, it was assumed that the RAOs for the model could be defined in the same way. However, after redefining the RAOs according to the manual, the analysis converged. Later in the fatigue analysis it was discovered that the frequencies from Ariane had a different unit than in Flexcom. The frequencies in Flexcom had to be defined in Hz, while in Ariane the frequencies were given in rad/s. The frequencies were then redefined and the correct response was obtained. The RAOs can be found in appendix D.

Because of limited time, all the sea states from the batch script could not be investigated. One combination of headings, 0 degrees for the wind, wave and current, was therefore selected for the analysis in Flexcom. The computational time was still long, even for one combination of headings. In order to reduce the time, the maximum element length was increased from 1m to

4.6m, as mentioned in chapter 5.1. By changing the maximum element length, the result would still not be affected by numerical errors because the software would use the smallest element length at the transition between the sections, and then increase the length for each element till a maximum length of 4.6m.

For the selected combination of headings, there were 31 different sea states to be investigated, and these were created through a code in Flexcom. The code was created with "Excel variations", which generates an analysis file for each sea state by using spread sheet. Part of the spreadsheet is shown in figure 5.13.

DriftFileName	Filename	Hs	Tp	Wave	Current
Displacement_LF_0.dat	0	6.0	3.5	0	0
Displacement_LF_1.dat	1	6.0	4.5	0	0
Displacement_LF_2.dat	2	6.0	5.5	0	0
Displacement_LF_3.dat	3	6.0	6.5	0	0

Figure 5.13: Inputfile for creating sea states with excel variations in Flexcom

Each line in the spreadsheet represents a load case. Flexcom calls the excel sheet by using the keyword "Excel variations", reads each line, and create load case variations using the defined parameters. The headings of each column in the excel sheet are defined as varying parameters, and the text/values under each heading are input values for these parameters. When Flexcom has found a new load case, it creates a new analysis keyword file. After creating a analysis file for all the load cases in the excel sheet, the analysis files must be manually started by the user. From figure 5.13, the first column consists the time history files from Ariane. The second column gives the filenumber id, which helps the user to keep an overview over the files. The following columns give the significant wave height, peak period, wave heading and current heading that corresponds to the same values used to obtain the time histories from Ariane.

Some of the sea states where excluded from the analysis because they exceeded the limiting condition of 20 meter offset. In order to find the sea states exceeding this limit, Arian was re-run in order to obtain a file which gave the mean, maximum and minimum position of the riser head. From the analysis with wind, wave and current heading in 0 degrees of freedom, it was discovered that sea state 9, 10, 11, 12 were exceeding the limiting condition. These were therefore excluded from the global load analysis and fatigue analysis. The limiting condition was

only checked for the LF motions, and not the combination of LF and HF. Since HF motions are present by the combination of RAOs and spectrum, there could be more sea states that exceeds the limiting condition. During this investigation of the exceeding sea states, it was discovered that the mean value of some of the sea state increased drastically. This was an odd behavior, and the analysis in Ariane was rerun. After the second rerun, the mean values were correct. A possible bug could therefore have occurred in the software.

In order to simplify the method, an analysis with no second order vessel motions was also investigated. The assumption was that an analysis without the second order vessel motions would be more conservative since the drift motions could perhaps contribute to damping of the system. A global load analysis and a fatigue analysis were therefore conducted with no drift motions. The results from this investigation are given in chapter 6.2.

5.4 Fatigue analysis

The drilling riser will experience fatigue damage in the installation phase, drilling phase and in the tripping phase. The tripping and installation phase is assumed to take one to four days. During the drilling phase, the riser is connected to the vessel, and the fatigue damage during this phase is calculated with Flexcom. The lifetime of the vessel is assumed to be 25 years (Toderan, 2016). According to Bureau Veritas rules, 2/3 of the lifetime should be calculated for fatigue damage (Bureau Veritas, 2016b).

A module called "LifeTime" in Flexcom has been used for calculations of the fatigue damage. This module performs a time domain fatigue analysis, which consist of three steps (Wood Group Kenny, 2015).

1. Perform time domain analysis and store time histories of y & z bending moment and axial force.
2. Specify stress concentration factor (SCF), S-N curve, probability density function (PDF), hot spots and thickness effects.
3. Run LifeTime with statistics, spectrum and rainflow method.

In order to calculate the fatigue life over the entire riser, a set of the hot spots were defined. The set consisted of all elements from the bottom of the riser to the top of the riser. Time histories from the first node of each element was stored from the time domain analysis, and the stress used in the analysis was calculated from the combination of bending moments and axial force. The SCF was set equal to one, and the S-N curve was taken from DNV standards, *DNV-RP-C203* (DNV, 2011a). The Rayleigh PDF was selected for the fatigue calculations, and no thickness effects were taken into account.

The S-N curve from DNV standards represents a seawater environment with cathodic protection. The curve selected for the analysis is the B2 curve, shown in figure 5.14. The data given for the curve is shown in figure 5.15. The B2 curve is for hollow sections with automatic longitudinal seam welds (DNV, 2011a).

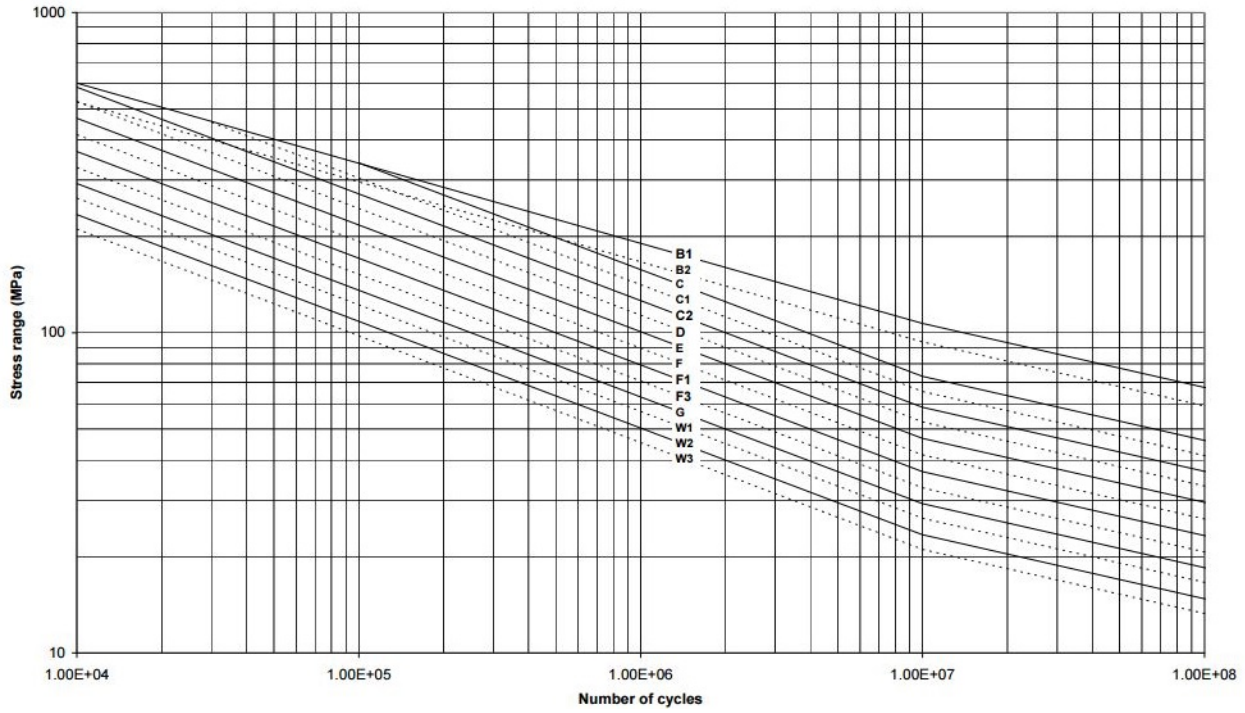

Figure 5.14: S-N curve in seawater with cathodic protection (DNV, 2011a)

Table 2-1 S-N curves in air

S-N curve	*$N \le 10^7$ cycles*		*$N > 10^7$ cycles*	*Fatigue limit at 10^7 cycles *)*	*Thickness exponent k*	*Structural stress concentration embedded in the detail (S-N class), ref. also equation (2.3.2)*
	m_1	$\log \bar{a}_1$	$\log \bar{a}_2$ $m_2 = 5.0$			
B1	4.0	15.117	17.146	106.97	0	
B2	4.0	14.885	16.856	93.59	0	
C	3.0	12.592	16.320	73.10	0.15	
C1	3.0	12.449	16.081	65.50	0.15	
C2	3.0	12.301	15.835	58.48	0.15	
D	3.0	12.164	15.606	52.63	0.20	1.00
E	3.0	12.010	15.350	46.78	0.20	1.13
F	3.0	11.855	15.091	41.52	0.25	1.27
F1	3.0	11.699	14.832	36.84	0.25	1.43
F3	3.0	11.546	14.576	32.75	0.25	1.61
G	3.0	11.398	14.330	29.24	0.25	1.80
W1	3.0	11.261	14.101	26.32	0.25	2.00
W2	3.0	11.107	13.845	23.39	0.25	2.25
W3	3.0	10.970	13.617	21.05	0.25	2.50
T	3.0	12.164	15.606	52.63	0.25 for SCF ≤ 10.0 0.30 for SCF >10.0	1.00

*) see also section 2.11

Figure 5.15: Input data for S-N curve in seawater with cathodic protection (DNV, 2011a)

The S-N curve was defined with two options in Flexcom, i.e data pairs and log-linear curve. The S-N curve defined with data pairs included three stress range values and the number of cycles cause to failure for each stress range. The S-N curve using a piecewise linear curve included two lines represented by the parameters m, $\bar{a}$, and the interval of N. The reason for trying both options of the S-N curve was because of the odd results from the fatigue analysis. It was assumed that the definition of the S-N curve in the software was the reason for odd results, but after trying both options the result remained the same.

The fatigue damage was calculated with three different methods, statistics, spectrum and rainflow (Wood Group Kenny, 2015).

- Statistics: Based on Rayleigh distributed stress peaks. Damage is found from standard deviation and mean zero up-crossing period from axial and bending stress.
- Spectrum: Based on Rayleigh distributed stress peaks. Damage is found from combined stress.
- Rainflow: Based in rainflow cycle counting technique. Damage is found directly from stress histories. The rainflow method gives the most accurate solution of the damage,

and is therefore the most important method (Sævik, 2016). More detailed explanation of the theory relating to this method is given in chapter 3.

According to *DNV-RP-F204*, a fatigue analysis should include the cyclic load effects from first order wave effects, second order floater motions, VIV, thermal and pressure induced stress cycles, collisions and floater hull VIV motions (DNV, 2010b). The time domain analysis had a simulation time of one hour, which is considered to be sufficient enough for fatigue calculations (Holm et al., 2013). In order for the fatigue analysis to calculate the damage, the result file from the time domain analysis had to be defined as an input file in the analysis. In addition, for each input file the probability of occurrence had to be defined. Due to the limiting condition of the significant wave height, only parts of the scatter diagram was used in the analysis in Ariane and Flexcom. These sea states gave a total probability of 86.4%. The Flexcom software requires that the total probability is 100% and therefore, in order to solve this issue one fatigue analysis was created for each sea state with 100% probability of occurrence. Each analysis were created with excel variations. Since the probability of occurrence was incorrect, the damage had to be multiplied with the true probability of occurrence for each respective sea state. The total damage was found by adding the damage from each sea state together. In order to calculate the correct lifetime, the damage should be multiplied with 2/3 of the total lifetime of 25 years. The results from the fatigue analysis are shown in chapter 6.3.

Since the fatigue analysis gave odd results, a number of sensitivity studies were conducted. The first check was to investigate the response from the time domain analysis. The resultant moment, standard deviation, effective tension and shear force were investigated for a 3-hour sea state. The results from the check are given in chapter 6.2. The second check was the definition of the S-N curve. The two options of how to define the curve was investigated, but the result remained unchanged. A small error was however discovered in the software. The input stress was required in Pa, but in the newest version of Flexcom the stress was required in MPa. This was corrected after verifying with Flexcom support that the stress should have been defined in MPa for version 8.4.1, which was used to generate the analysis. However, after correcting the stress, the results still remained unchanged. In addition to the two checks, another S-N curve was applied, in order to see if there were any damage. The S-N curve was taken from the exam-

ple model in Flexcom, and was defined with parameters m=2.5 and $\bar{a}$=10^8 (Wood Group Kenny, 2015). The results from using this S-N curve showed damage of the riser.

During the checks, it was discovered that the input files from Ariane were defined incorrect in Flexcom. The input files consisted of three columns, time, displacement in DOF 2 and displacement in DOF 3. However, after some investigation it was discovered that displacement for DOF 1, 4, 5 and 6 had to be defined in the input file, in order for Flexcom to read it correctly. The displacement for these DOFs would not be applied to the model either way, because they were not defined in the boundary condition option for the vessel. As mentioned in chapter 5.3, only the second and third DOF were defined in the boundary condition option for the vessel, and therefore only the displacement for these DOFs would be taken into account in the analysis. New input files were therefore created with zero displacement in the other DOFs.

After correcting both the RAOs and the input files, the result remained unchanged. A last check was performed, in order to see if the response was correct. A sensitivity test of the SCF was performed in order to see how when damage would occur. Three analysis with SCF 1, 10 and 20 were conducted. In addition, a fatigue analysis with no drift motions was performed in order to see if the riser would obtain more damage, since it was assumed that the drift motions would give damping to the system. The results from these investigation can be found in chapter 6.3.

5.5 VIV analysis

The VIV analysis is performed with Shear 7 and Flexcom. The program uses the eigenvalue solution, solved by Flexcom, and finds the fatigue damage caused by VIV by estimating which of the modes will coincide with the vortex shedding. The modes can be axial modes, torsional modes, bending modes or mixed modes, but it is the bending modes which are important for Shear7. Since the bending modes appear often in pairs, the eigenvalue analysis will identify the pairs and rename one the mode as unknown and the other bending mode. The bending modes are used in the Shear7 analysis (Wood Group Kenny, 2015). For most problems the vibration shape is determined by the lowest mode shapes. Higher mode shapes have often errors, and are therefore neglected in the analysis (Langen & Sibjørnsson, 1979). It is therefore important to not

select too many of the eigenmodes for the VIV analysis. A total number of 80 eigenpairs have been selected for the eigenvalue analysis and the convergence tolerance is set equal to 10^6. The eigenvalue analysis has been performed with and without current.

An important input in the eigenvalue analysis is to decide how many segments with equal lengths should be used in the Shear7 analysis. Even though the model is created with segments of different lengths, the eigenvalue analysis interpolates between the elements, and creates equally long elements that can be inserted in the Shear7 analysis. The number of segments should, according to the output file from the Shear7 analysis, be above 185. The number of segments selected in the analysis is therefore 400. This input changes however the fatigue damage, and the input should therefore be selected with care. Another important input is the number of modes to be considered in the Shear7 analysis. This number must be equal to the number of eigenpairs in order for the analysis to work.

After identifying the bending modes, the model is converted into the required format in the Shear7 analysis. The current is also redefined as well as the S-N curve. When redefining the current in the Shear7 analysis, one or a few extra lines with zero surface velocity should be defined. This is because Shear7 defines the current from the top of the riser, and not at the water line. The converted model contains information obtained from the eigenvalue analysis such as drag diameter, inner and outer diameter, internal fluid mass, unit mass, added mass, number of segments per element and the element length, the axial stiffness and the type of riser.

An important check in the VIV analysis is to ensure that all of the bending modes selected from the eigenvalue analysis, are in fact bending modes and not mixed modes. The mixed modes are created by combining the axial, torsion and bending modes. In order to check this, a graph of mode number with modal curvature, should be monotonically increasing. If some of mixed modes are present, the plot will be show local maximas (Wood Group Kenny, 2015).

The result from the eigenvalue analysis and the VIV analysis, both with and without current, can be found in chapter 6.4. A sensitivity analysis of the SCF is also carried out for the VIV analysis, with SCF equal to 1, 1.3 and 9. SCF 9 is the highest SCF value in Shear7.

Chapter 6

Results and discussion

The results from the different analysis in Flexcom are presented in this chapter. The x-axis in all the graphs are given from origo, which is located at the seabed.

Chapter 6.1 gives the results from the simplified representation of the second order vessel motions. In this analysis, steady state and effective tension have been investigated. In addition, the boundary conditions at the top and the current direction at 0,45 and 90 degrees, have also been investigated and compared. Chapter 6.2 gives the results from the application of the true second order vessel motions. Different types of applications of the vessel motion in the software have been investigated, in addition to the effect of waves. For the final analysis model, the response from 31 sea states have been investigated. The results from the worst sea states for a 3-hour sea state have been studied with respect to yield. Chapter 6.3 gives the results from the fatigue analysis for the 31 sea states from the time domain analysis. The analysis have been performed with SCF 1, 10 and 20, and no second order vessel motions. Chapter 6.4 gives the results from the VIV analysis. The analysis has been performed with SCF 1, 1.3 and 9. Chapter 6.5 presents the uncertainties in the methodology.

6.1 Simplified global load analysis

Steady state

The results from the simplified second order vessel motions, represented by a harmonic motion in y-direction, are presented below. The post-processing is performed at a user defined time, and it is therefore important to look at the load time history to see if the analysis has reached steady state. Figure 6.1 shows a snapshot of element 233. The graph shows great irregularities in the first 80s, but has reached steady state after 300s. The post-processing is therefore conducted at t=300s.

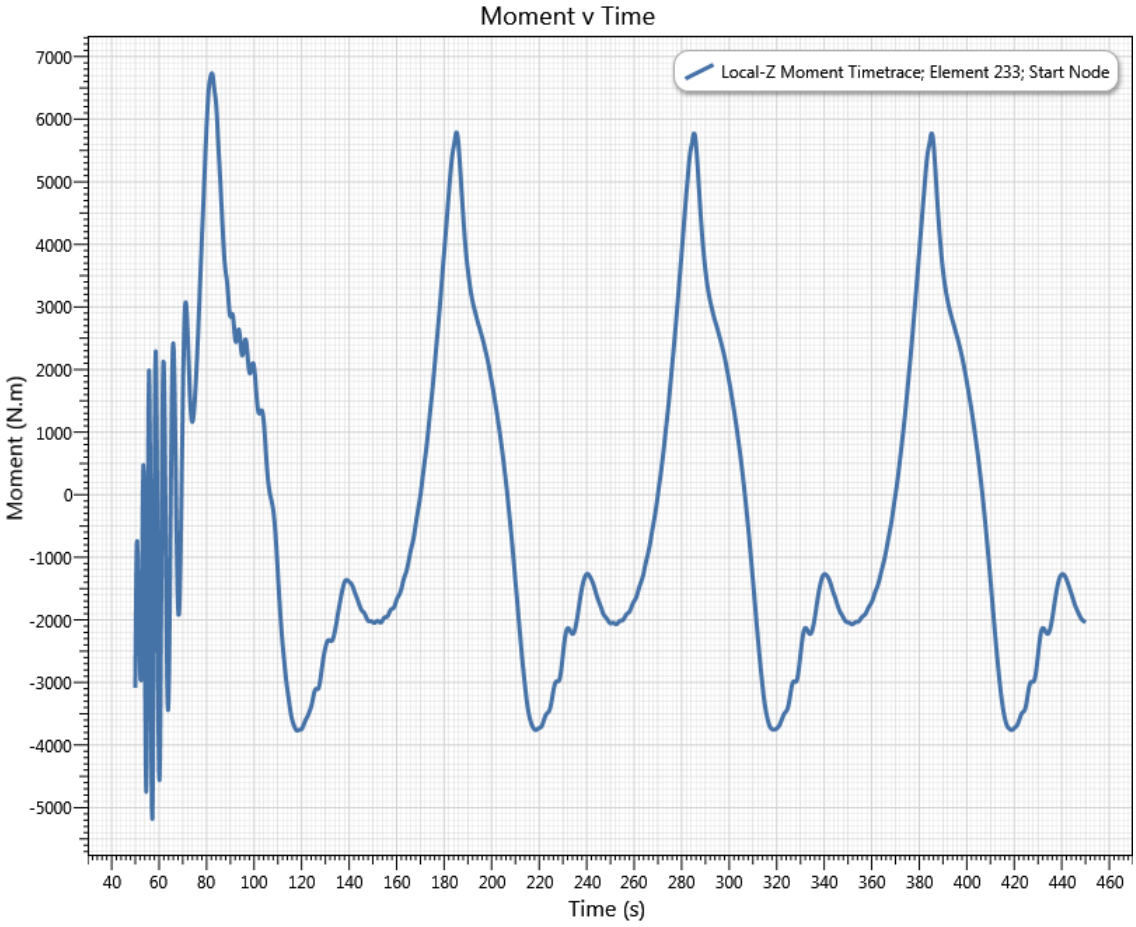

Figure 6.1: Time history of bending moment

Effective tension

Another plot of interest is the effective tension, shown in figure 6.2. In the Flexcom model, the hydrodynamic coefficients are applied over the entire riser. However, the top part of the riser is not submerged and should therefore not have the applied coefficients. The effective tension can be investigated in order to see if Flexcom applies these coefficients to the non-submerged part. If there is a change in the slope, the coefficients are not considered. There are two changes in the slope in figure 6.2, one at the bottom and one at the top. The change in the slope at the bottom is due to the flex joint in the model. At the top of the riser, the change in the slope occurs at the water line. This indicates that the coefficients are not taken into account when the riser is not submerged.

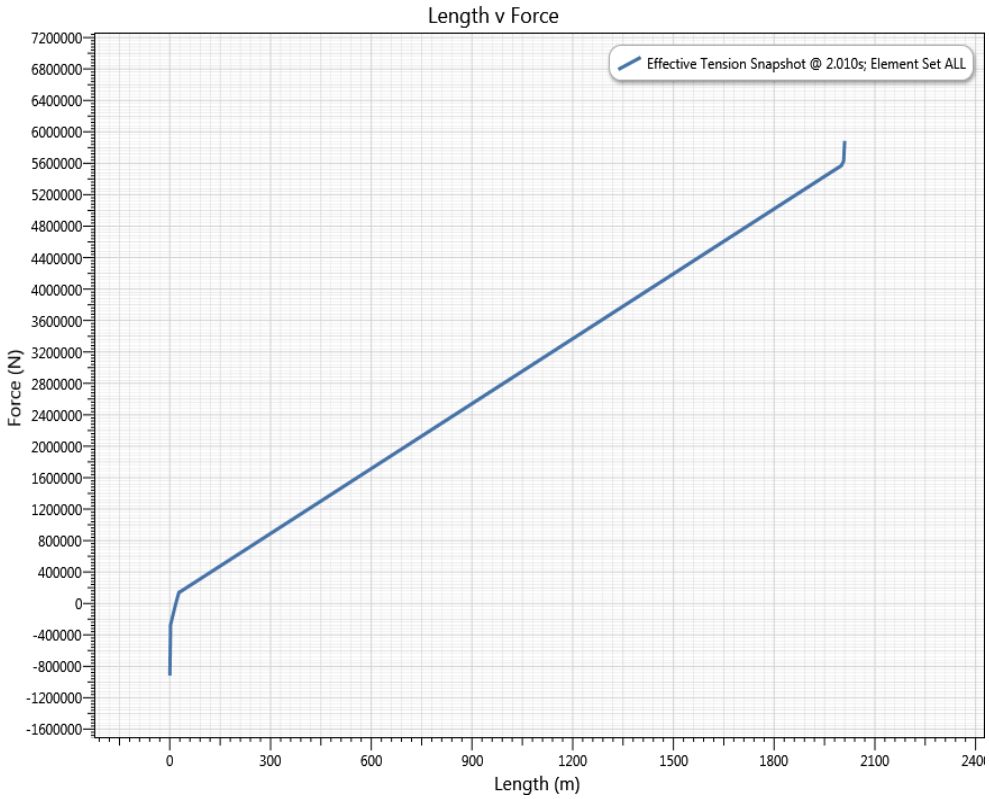

Figure 6.2: Effective tension, 600 tonnes top tension

As mentioned in chapter 3, the effective tension is defined as the difference between the total column tension and the tensile force in the displaced fluid column. The equation is given in 6.1. The external pressure represents the force which is in compression in the displacement fluid column. If this force is larger than the total column tension, the effective tension will become negative.

$$T_e = (T_{tw} - p_i Si) - (-p_e S_e) \tag{6.1}$$

The effective tension can be explained by Archimedes' law, which says that the weight of the displaced fluid is equal to the upthrust. The law can only be applied to closed pressure fields, and does not give any information about the stresses or the internal forces. When forces acts on a segment of the body, the pressure field will be open, and in order to use the law the pressure field must be closed. The problem is therefore divided into two parts, one part where the pressure field is closed and replaced by the upthrust, and another part with the true weight, W_{true}. The sum of these parts gives the segment's apparent weight, W_{a}. Since the pressure field was closed for the first part, and the force $P_e S_e$ was subtracted, the force must be added in the second part to the true tension T_{true}. The true tension and the force gives the effective tension T_{e}. Figure 6.3 shows the derivation of the problem.

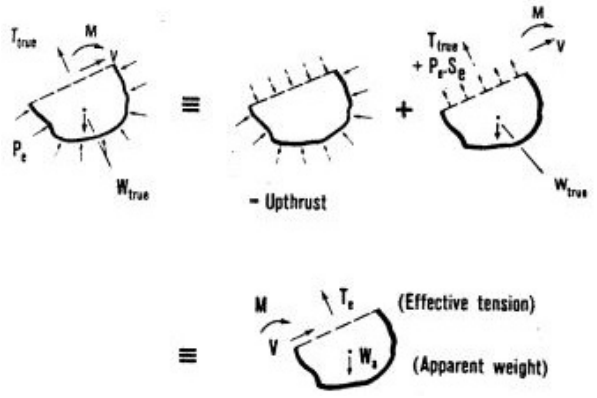

Figure 6.3: Derivation of effective tension (Sparks, 1984)

The internal pressure will also contribute when this is applied to a riser. An extra weight will then contribute to the true weight, and the equation becomes equal to equation 6.1 (Sparks, 1984).

If the external pressure becomes larger than the column tension, the riser will possibly buckle. It is therefore important that the effective tension is positive at all times. Figure 6.2 shows the effective tension of the riser when 600 tonnes are applied as top tension. The graph is negative at the very first part of the riser from the seabed, and the reason for this could be due to the high stiffness of the elements at the bottom part of the riser. In order for the effective tension to become positive, as possibility is to increase the top tension to 700 tonnes, as shown in figure 6.4. A top tension of 600 tonnes is however, assumed to be sufficient enough to prevent buckling as explained in 5.1.6 and appendix A and B.

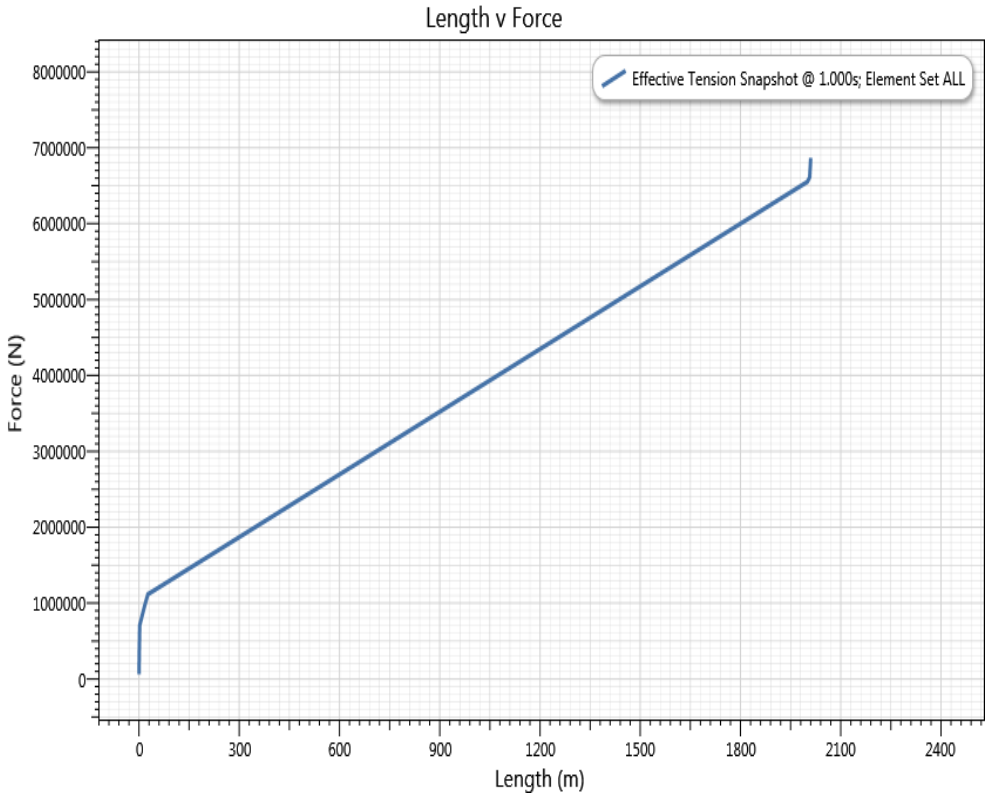

Figure 6.4: Effective tension, 700 tonnes top tension

Bending moments

Figure 6.5 shows the bending moment in z-direction and figure 6.6 shows the bending moment in y-direction. The moment is relatively large at the bottom of the riser. The reason for this is because of the defined boundary conditions, which are fixed in all translations and rotations. As mentioned in chapter 5.1, the wellhead connection to the seabed and the soil are usually designed with a spring at the seabed and pinned boundary conditions at the soilnode. If the bottom part of the riser was designed with a spring and pinned boundary conditions, the moment would probably be reduced. However, it is difficult to know how much the moment would be reduced, because the elements at the bottom of the riser have a high stiffness and therefore contributes also to the high increase of moment. At 27m from the bottom, a flex joint is added to the riser. The properties of the flex joint are demonstrated well in the figure, by reducing the moment significantly where it is applied. At the top of the riser, the moment increases, which could be due to the infinite stiffness of the telescopic joint. Another possibility could be due to the combination of the defined boundary conditions, where the translation in z-direction is fixed, and the motion from the second order vessel motions are applied in y-direction.

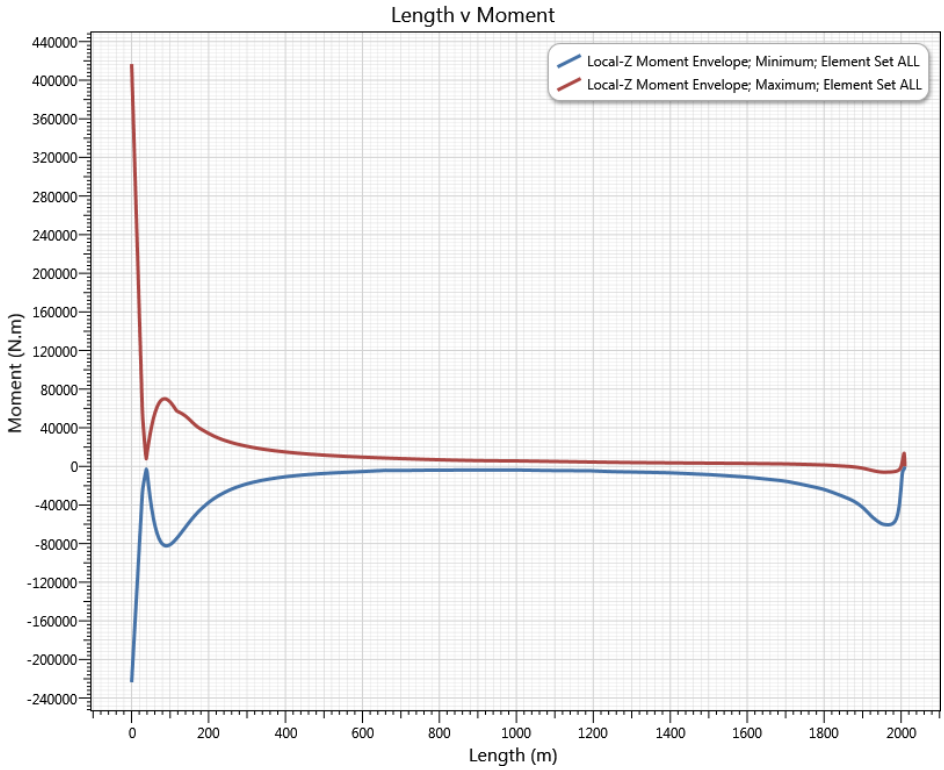

Figure 6.5: Local z-moment, free rotations, 0 degree current heading

Figure 6.6, shows no moment i the y-direction. The reason for this is because the model and the applied loads are symmetric about the axes. Both the second order vessel motions and the current are applied in y-direction, which gives zero torque and no moment.

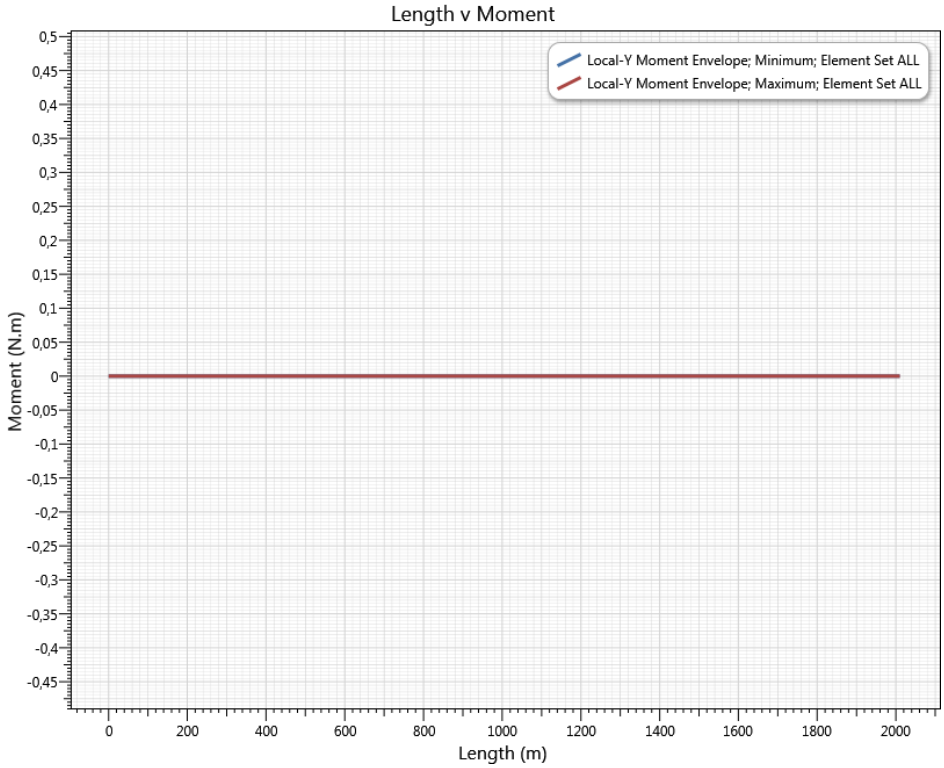

Figure 6.6: Local y-moment, free rotations, 0 degree current heading

Boundary conditions

The rotational boundary conditions were investigated in fixed and in free condition in order to find the design that represents best the properties of the tensioner system. The moment in z-direction with fixed boundary conditions is shown in figure 6.7, and in y-direction in figure 6.8. The current is applied at zero degrees for both the fixed and the free case. The local z-moment with fixed and free rotations show great differences in the moment at the top part of the riser. From figure 6.5, the maximum moment is equal to 60kNm, and in figure 6.7 it is 3MNm. The moment difference of 2.8MNm, and could possibly affect the lifetime of the riser and the vessel in the fatigue damage calculations. A possible solution to reduce this moment is to add an upper flex joint. Another possibility is to free the boundary conditions and neglect the rotational constraint from the tensioner system, as shown in figure 6.5. A third possibility is to design the tensioner system in more detail with tensioner lines. However, since the model should be as simplified as possible, it was decided that the rotations should not be constrained. Adding an upper flex joint is also a good solution, but since there exist designs without the flex joint it was preferred to design the riser without the joint.

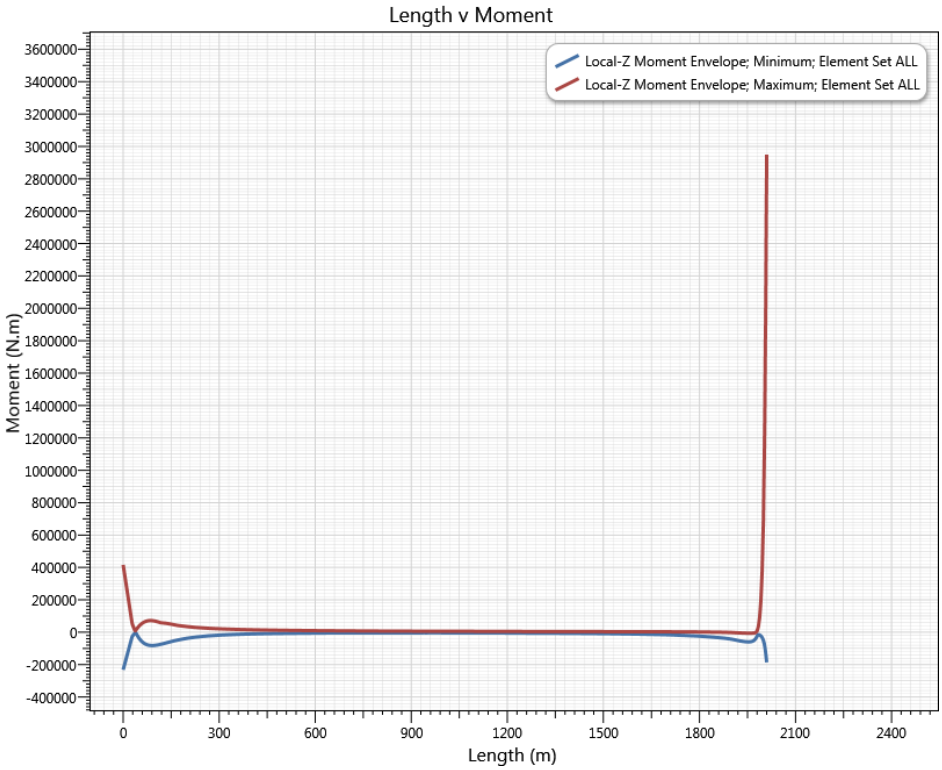

Figure 6.7: Local z-moment, fixed rotations, 0 degree current heading

Figure 6.8, shows no moment i y-direction. The reason for a zero moment is the same as for figure 6.6. The figure shows that the moment in y-direction at the top of the riser does not change when the rotations are free or fixed.

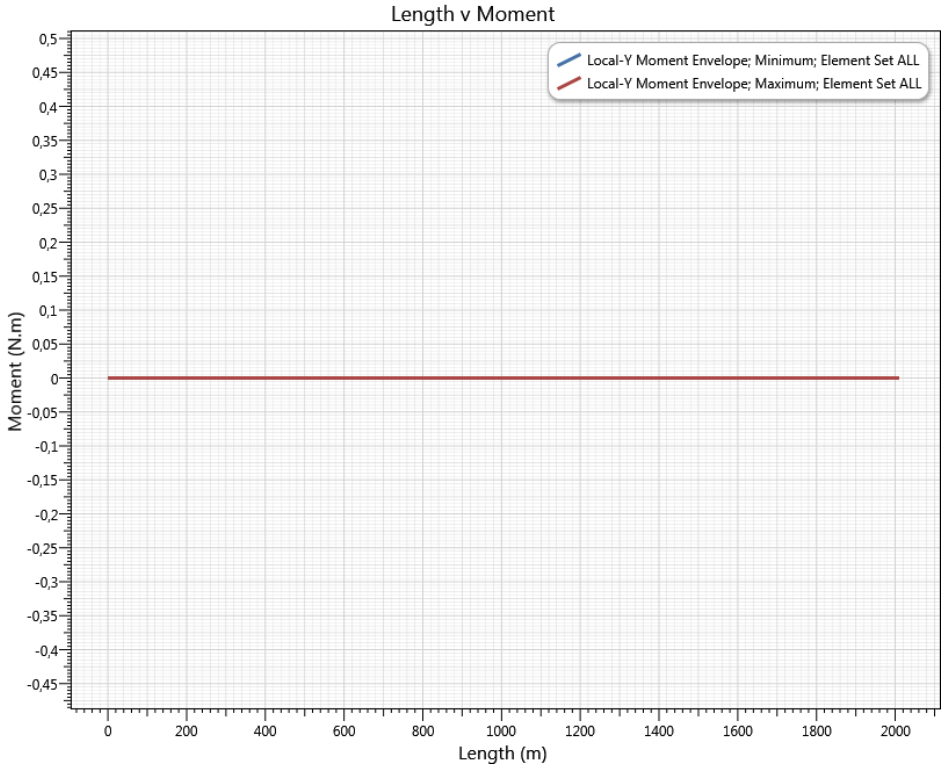

Figure 6.8: Local y-moment, fixed rotations, 0 degree current heading

Current direction

The current direction was also investigated. Figure 6.5 and figure 6.6 showed the moment when the current was applied at zero degrees, and figure 6.9 and figure 6.11 shows the moment when the current is applied at 45 degrees. Figure 6.10 and 6.12 shows the moment when the current is applied at 90 degrees. All figures show that the critical spots occur at the same locations on the riser. The highest moments are at the top and bottom, which is expected since the elements at the top and bottom have infinite stiffness and are also close to the boundaries. The moment over the buoyancy joint is relatively constant because the cross-section does not change.

From figure 6.5, when the current was applied at zero degrees, the maximum moment were at the bottom of the riser and equal to 440kNm. From figure 6.9, when the current is applied at 45 degrees, the maximum moment is equal to 400kNm. The moment at the top of the riser from when the current was applied at zero degrees was also larger than at 45 degrees. From figure 6.10, when the current is applied at 90 degrees, the maximum moment is lower than the two other cases. The magnitude is 340kNm at the bottom and 20kNm at the top. By comparing the moments from each case, the largest moment occur when the current is applied at zero degrees.

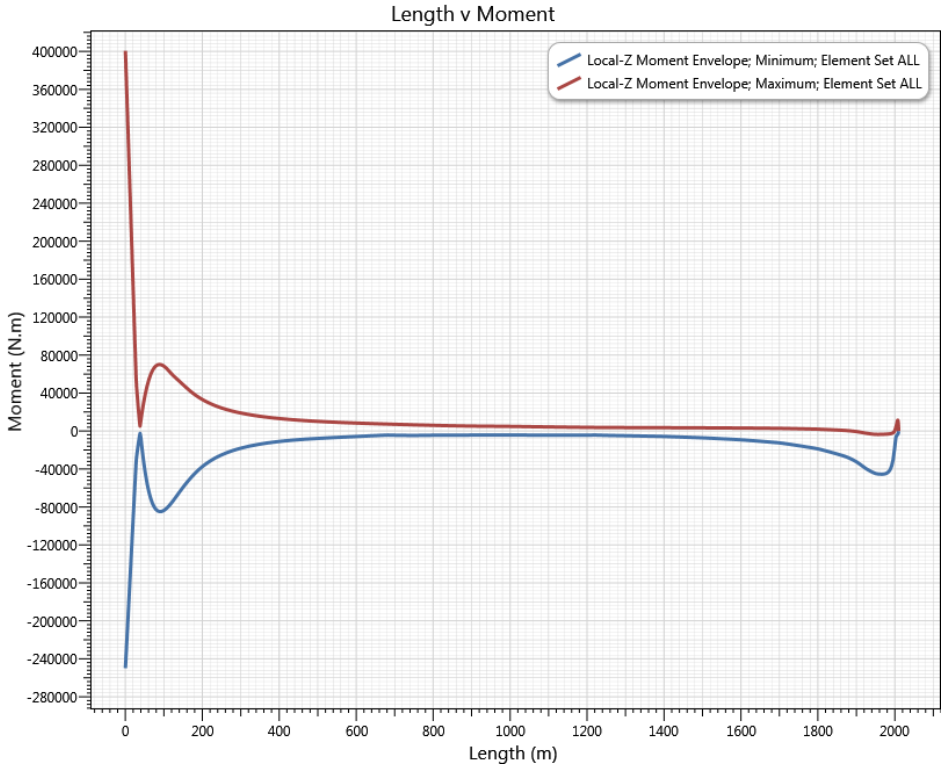

Figure 6.9: Local z-moment, free rotations, 45 degree current heading

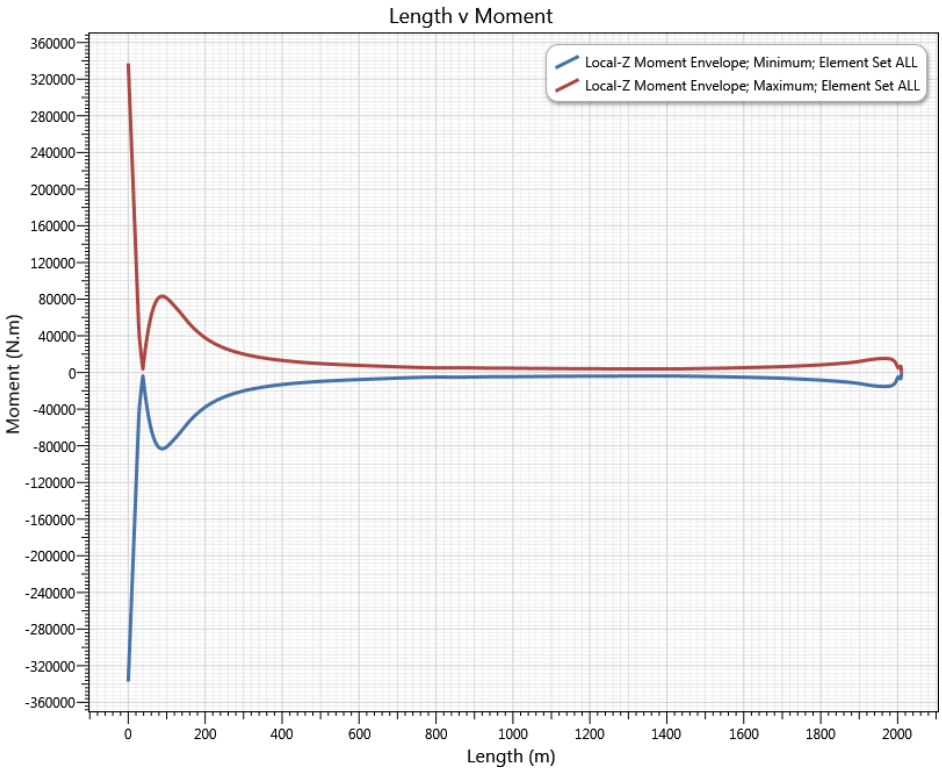

Figure 6.10: Local z-moment, free rotations, 90 degree current heading

The reason for a higher moment with current applied at zero degrees could be because the drift motions were added in y-direction, which is the same as zero degrees. From figure 6.6, when the current was applied at zero degrees, the moment was constant and equal to zero over the entire length of the riser. The moments from figure 6.11, when the current is applied at 45 degrees, and figure 6.12, when the current is applied at 90 degrees, are therefore compared instead.

From figure 6.11, the moment at the bottom of the riser has a max magnitude of 115kNm, while in figure 6.12 the max moment is 125kNm. The moment at the top from figure 6.11, is close to 25kNm, while in figure 6.12, the moment is 30kNm. The case which gives the highest moments is therefore the case when the current is applied at 90 degrees.

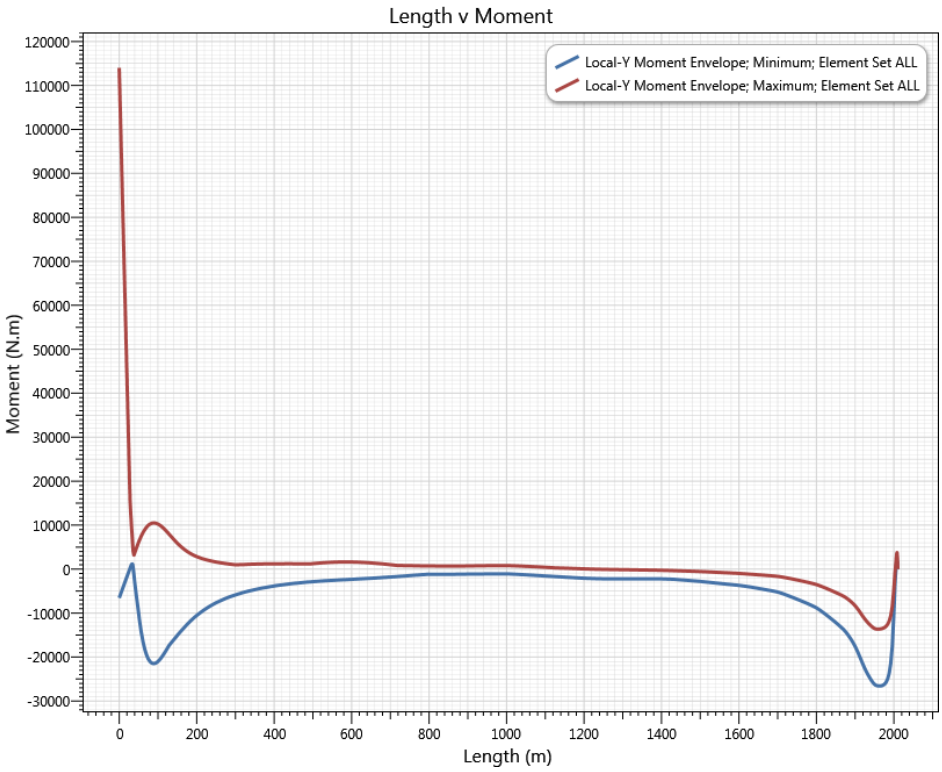

Figure 6.11: Local y-moment, free rotations, 45 degree current heading

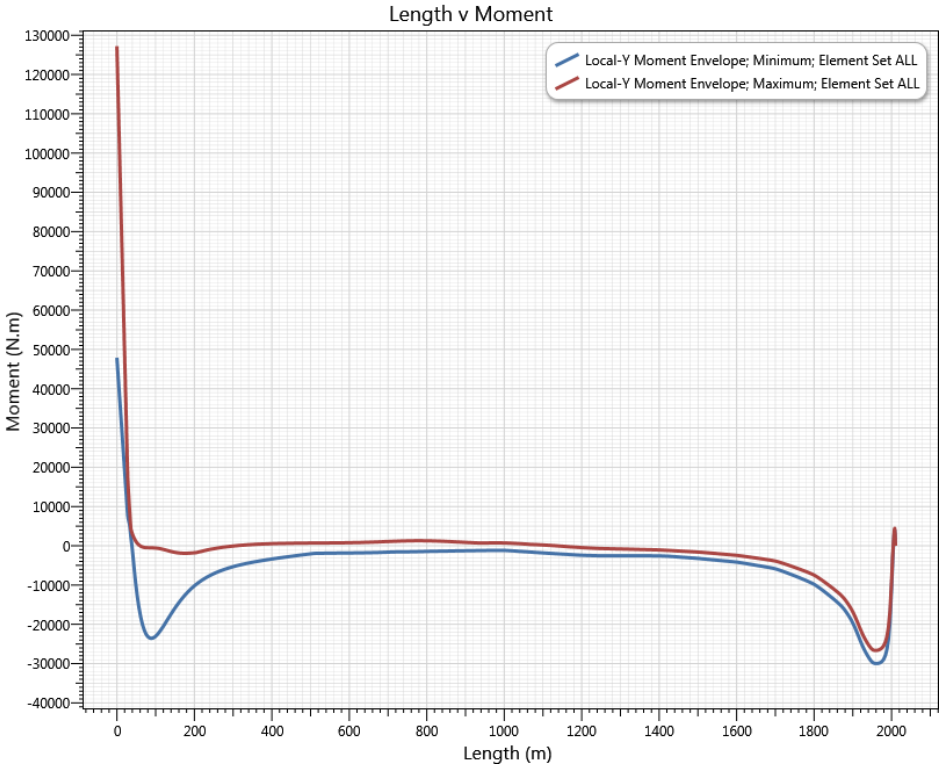

Figure 6.12: Local y-moment, free rotations, 90 degree current heading

6.2 Advanced global load analysis

Drift motions with WF and LF motions

Figure 6.13 and figure 6.14 shows the moment in z-direction and y-direction when the harmonic motion is replaced with the time histories from Ariane. The time histories consist of both LF and WF motions from the DP system. The time history representing sea state 0 is used, and the current, wind and wave are applied at zero degrees. The moments from the harmonic motion are quite different than the moments from the true motion. The maximum moment at the bottom of the riser from figure 6.5 was 400kNm, but close to 80kNm in figure 6.13. At the top of the riser, the moment from figure 6.6 was about 60kNm, while from figure 6.13 the moment is close to 25kNm. The moments from the harmonic motion shows therefore a more severe case with respect to yield, because the moment is higher. The moment in the simplified analysis was close to symmetric, while for the true second order vessel motions the moment is not symmetric because the motions are irregular.

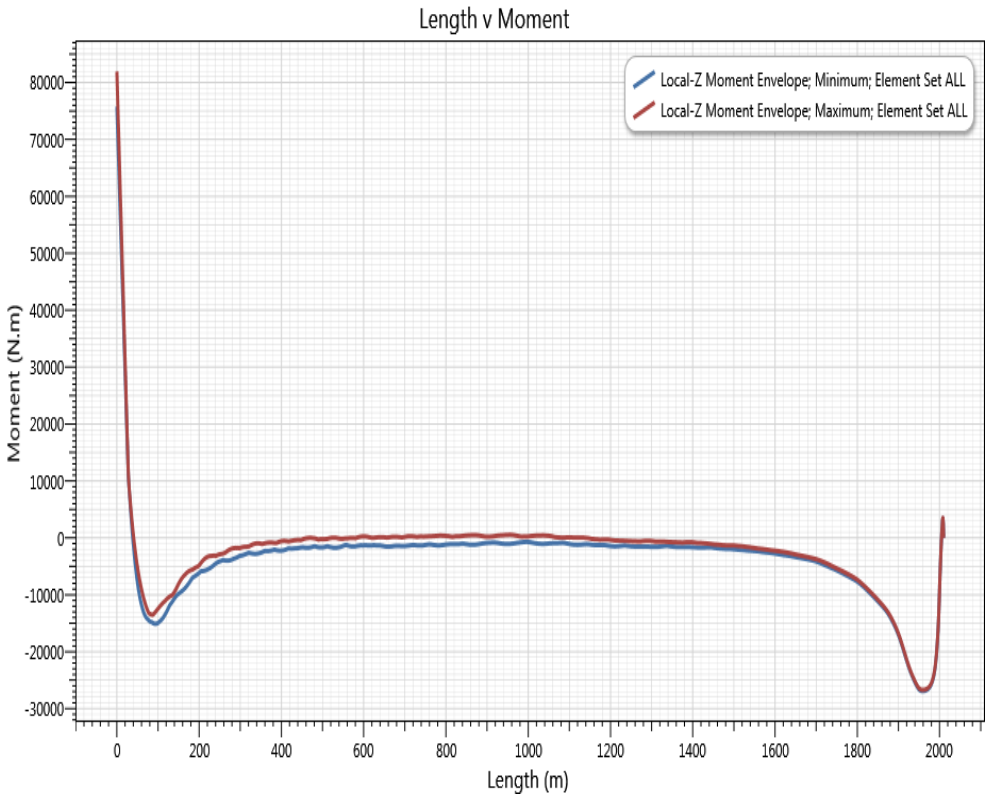

Figure 6.13: Local z-moment with WF and LF motions from the vessel

The moment in y-direction is also quite different. The motions from the simplified analysis were only applied in y-direction, while in the analysis with the true second order vessel motions, both y and z-direction had displacements from the vessel. This explains why there is a moment in y-direction in figure 6.14. The moment is close to symmetric about the axes, but since the motions are irregular, the moment will not become completely symmetric. The magnitude of the moment is close to 100kNm at the bottom and 10kNm at the top in figure 6.14.

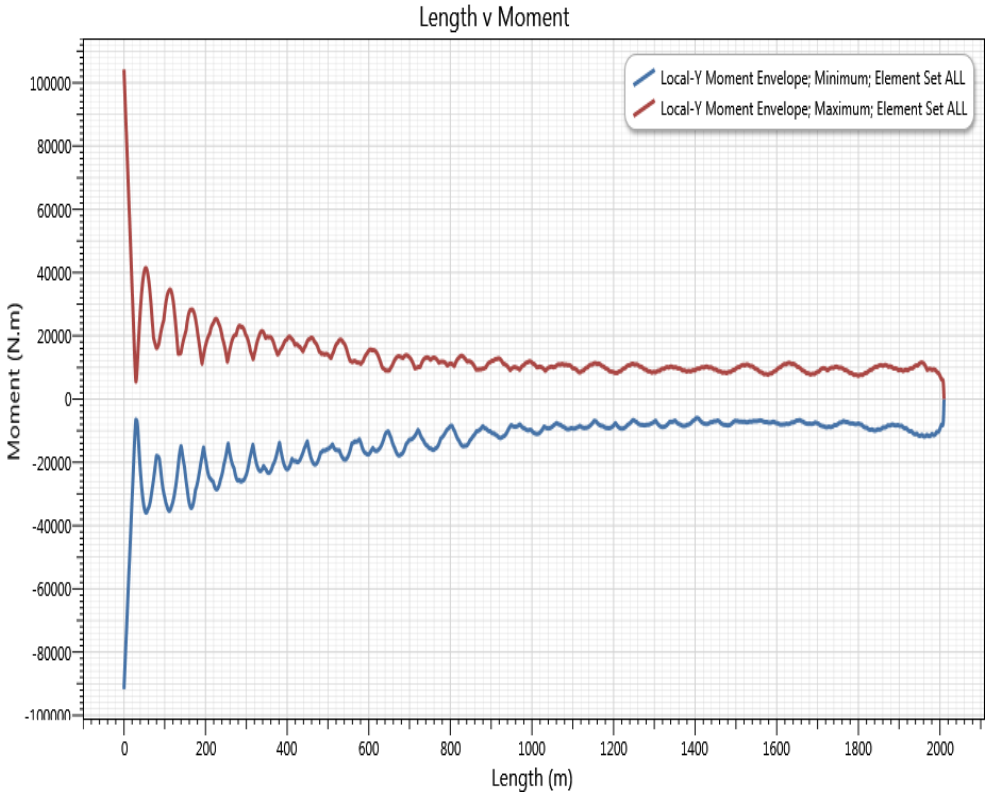

Figure 6.14: Local y-moment with WF and LF motions from the vessel

Wave effects

The effects from applying a regular wave to the riser is shown in figure 6.15 and figure 6.16. The model includes the second order vessel motions, both WF and LF motions, in addition to the regular wave and current. Figure 6.15 shows that the moment increases significantly at the top of the riser. This is because the waves decreases exponentially with the water depth. In deep water, when the water depth becomes more then $\lambda/2$, the waves will die out (Pettersen, 2007). As mentioned in 5.3, if neglecting the effects from the wave kinematics, the response would be non-conservative since the drag loads are not considered. Figure 6.15 shows that this effect should not be neglected since the moment increases significantly at the top of the riser. Waves should therefore be applied to the model in order to obtain a correct response.

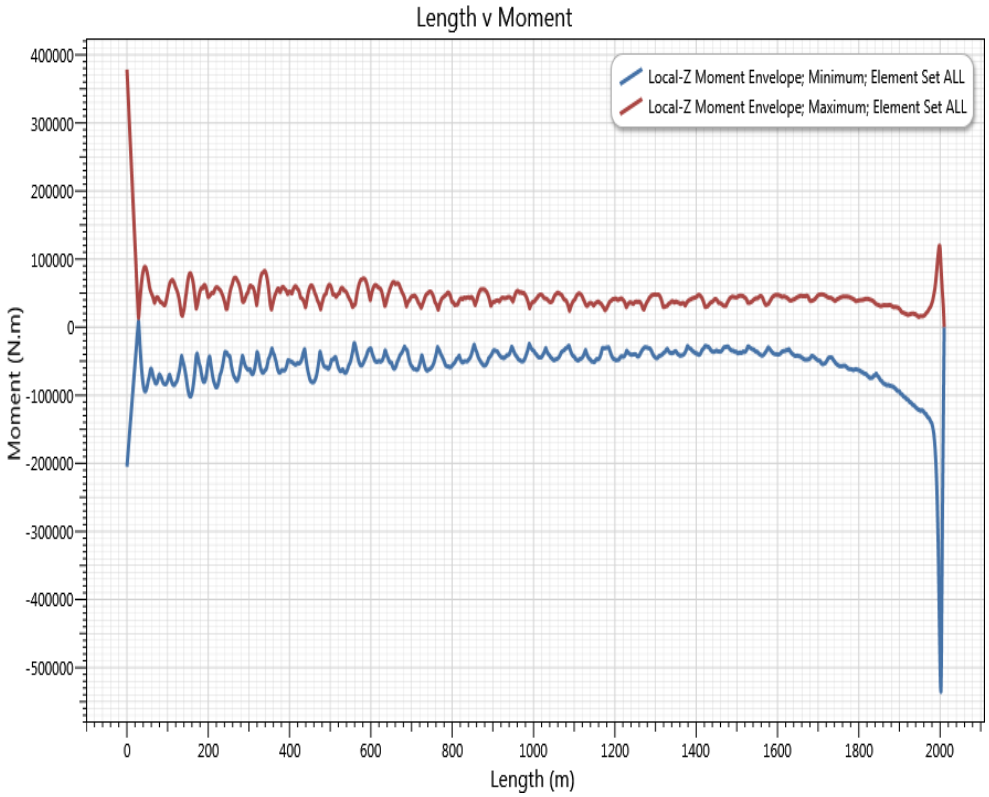

Figure 6.15: Local z-moment with regular wave

The moment in figure 6.16 is slightly reduced at the bottom of the riser, compared to the moment in figure 6.14. The magnitude at the bottom has a maximum value equal to 90kNm, while in figure 6.14 the magnitude is slightly above 100kNm. The moment at the top is also reduced by 10kNm compared to the moment at the top from figure 6.14. The reason for the decrease in moment could be due to the dominating moment in z-direction.

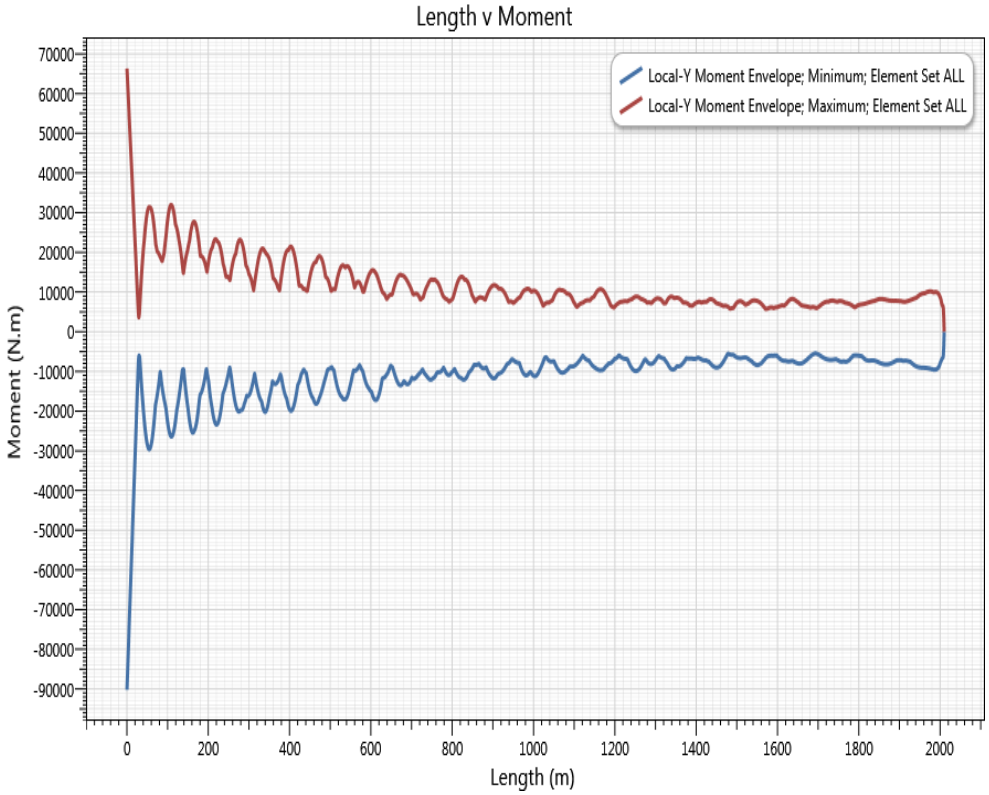

Figure 6.16: Local y-moment with regular wave

Final analysis model

The results below are given for one combination of headings when both waves and second order vessel motions are considered. The motions include the LF motions, and the wave kinematics are considered by adding RAOs and wave spectrum to the analysis. The current, wave and wind are applied at zero degrees. A total of 31 sea states have been investigated, but a selection of the worst sea states are presented and discussed in more details in this thesis.

Bending moments

Figure 6.17 is presenred in order to give an overview of the loads on the riser. The envelope curve shows the moment in z-direction for all of the sea state. The maximum moment occurs at the bottom of the riser, because of the boundary conditions and the high stiffness of the bottom elements. The increase in moment at the top of the riser shows the effect from the wave kinematics. The magnitude of the moment is close to the magnitude of the moment at the bottom of the riser. When comparing the moment from figure 6.15 with figure 6.17, it can be observed that the shape of the moment is quite similar, as well as the magnitude at the bottom of the riser. The magnitude of the moment at the top of the riser in figure 6.16 is however, larger than in figure 6.17. This could be because the WF are added to the drift motions at the top of the riser in figure 6.15, which gives a double effect of the wave kinematics at this location. It could also be because the wave is a regular wave and therefore has a higher amplitude than the irregular waves added in figure 6.17.

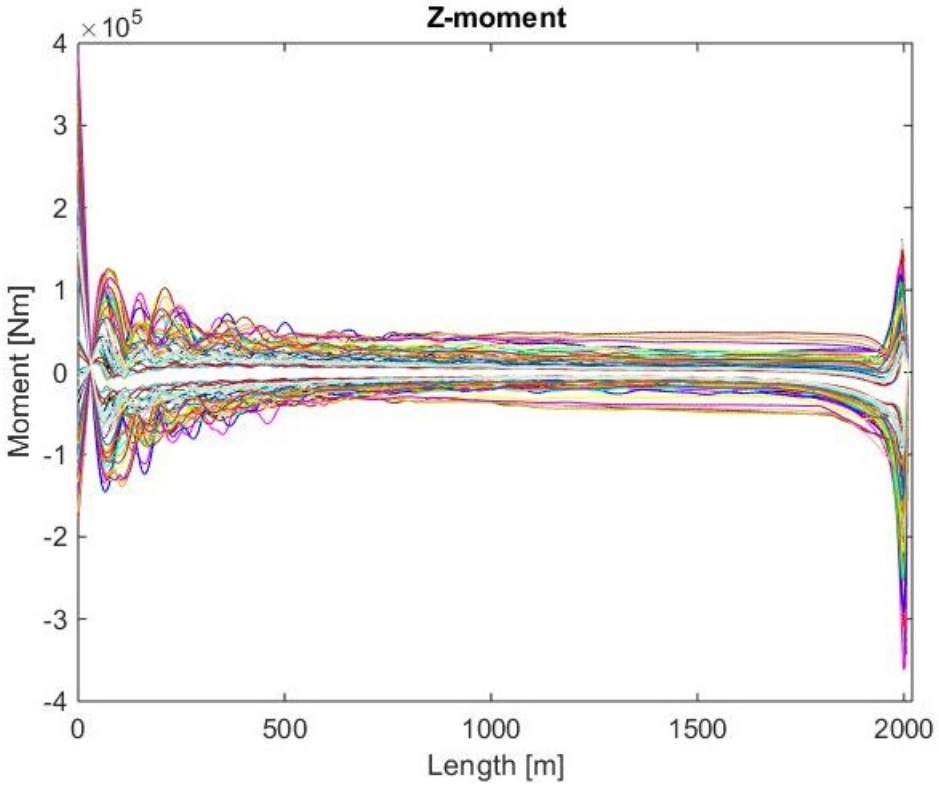

Figure 6.17: Z-moment for all sea states

The highest moments from figure 6.17 are shown in figure 6.18. Sea state 12, 11,10, 9, 8, 7, 6, 5, 4, 3 have the largest moments in the figure. As mentioned in the global analysis chapter 5.3, sea state 12, 11, 10 and 9 exceeds the limiting condition for the DP system, and should therefore not be considered in the analysis.

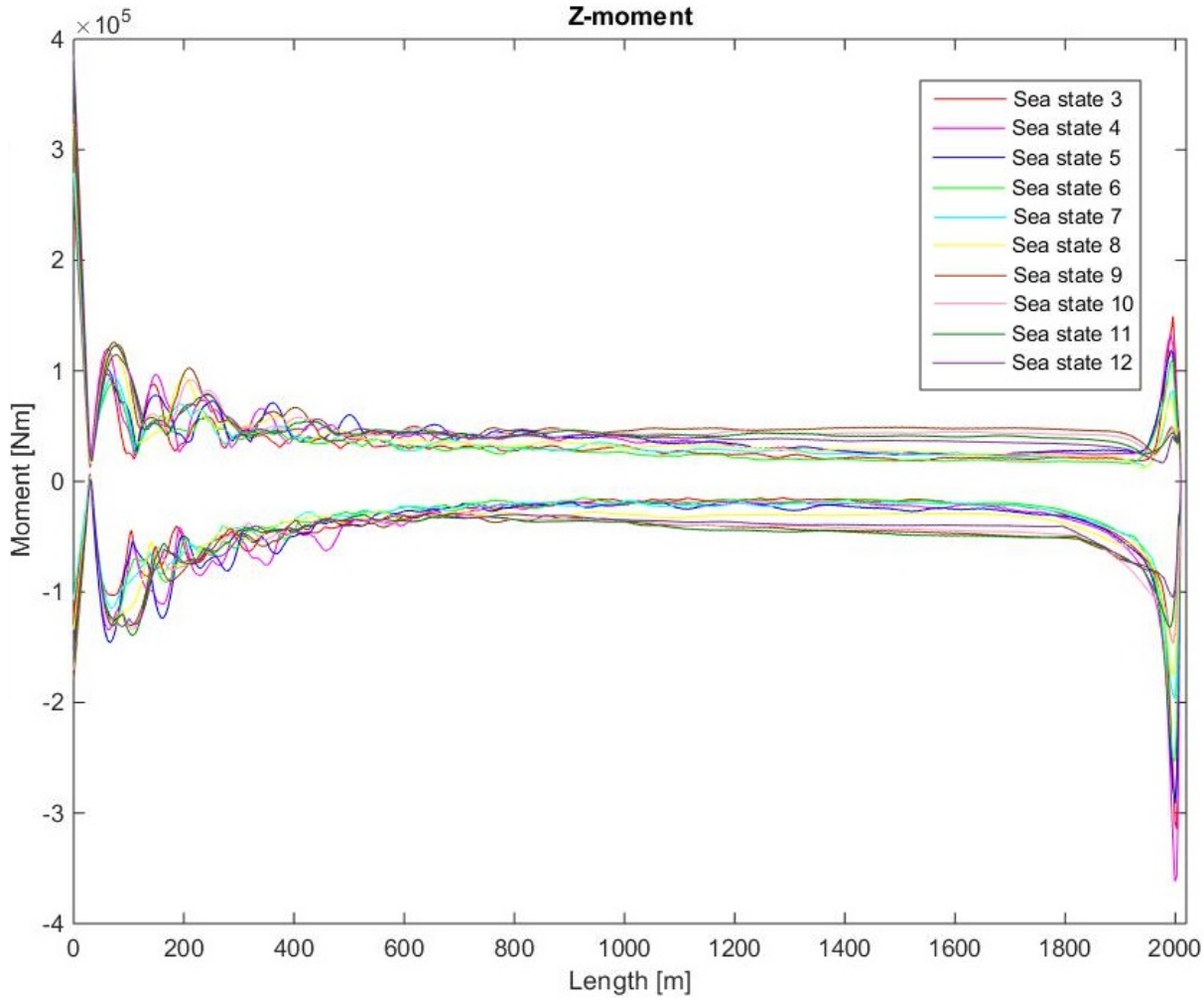

Figure 6.18: Z-moments for the worst sea states

The highest moments within the limiting condition of 20m offset, are shown in figure 6.19. The highest moments at the bottom of the riser comes from sea state 8, 7 and 6. The highest moments at the top of the riser comes from sea state 4, 3 and 5. The dominating moments are however, the moments at the bottom of the riser with magnitudes close to 300kNm.

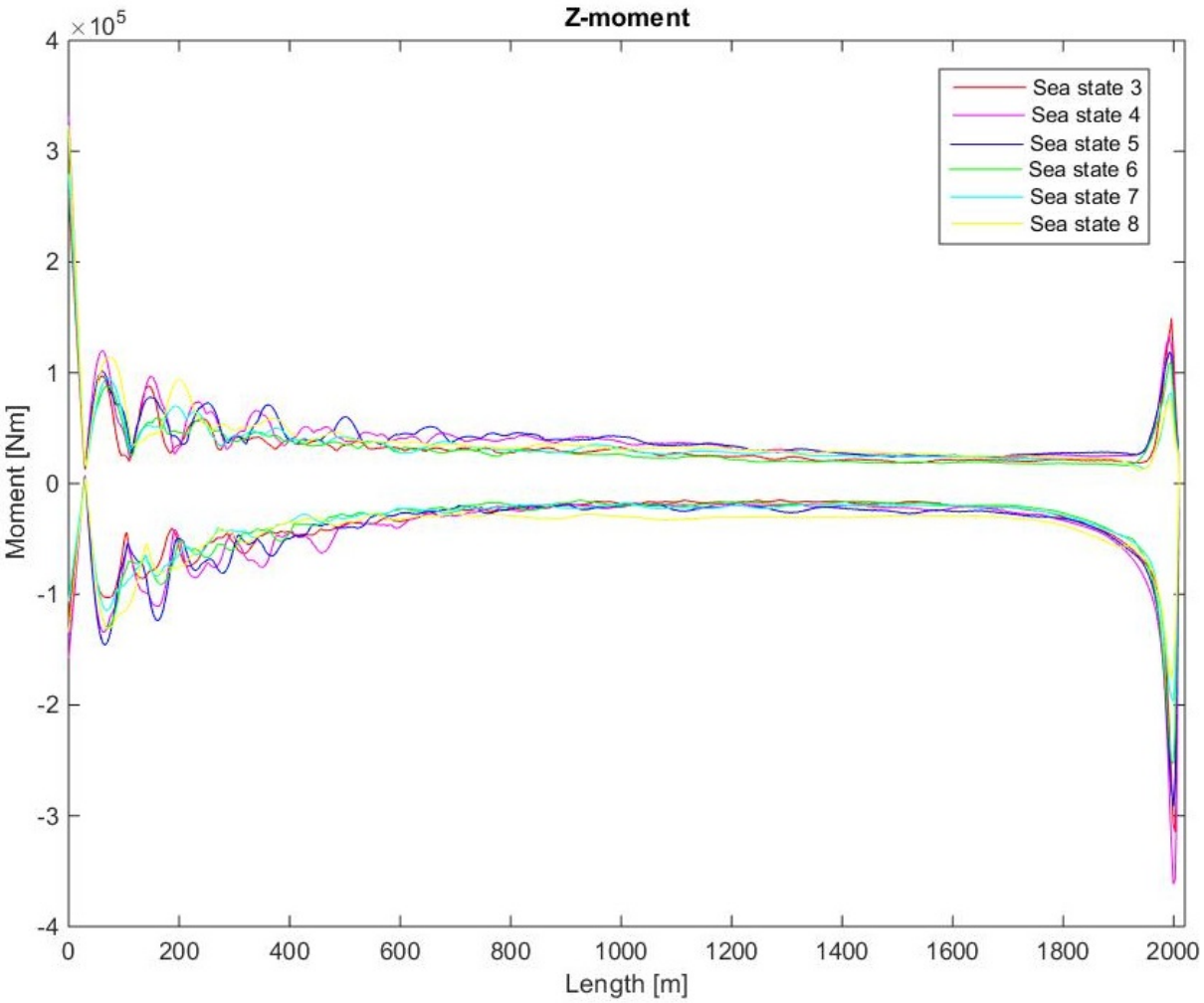

Figure 6.19: Z-moments for the worst sea states within limiting conditions

Figure 6.20 shows the moment in y-direction. The maximum moment occurs also at the bottom of the riser because of the boundary conditions and the stiff elements at the bottom. When comparing the moment from figure 6.16 with figure 6.20, it can be observed that the shape of the moment is somewhat similar, but the moment has less variation at the bottom part of the riser. The magnitude of the moment at the bottom is however, smaller in figure 6.16 than in figure 6.20.

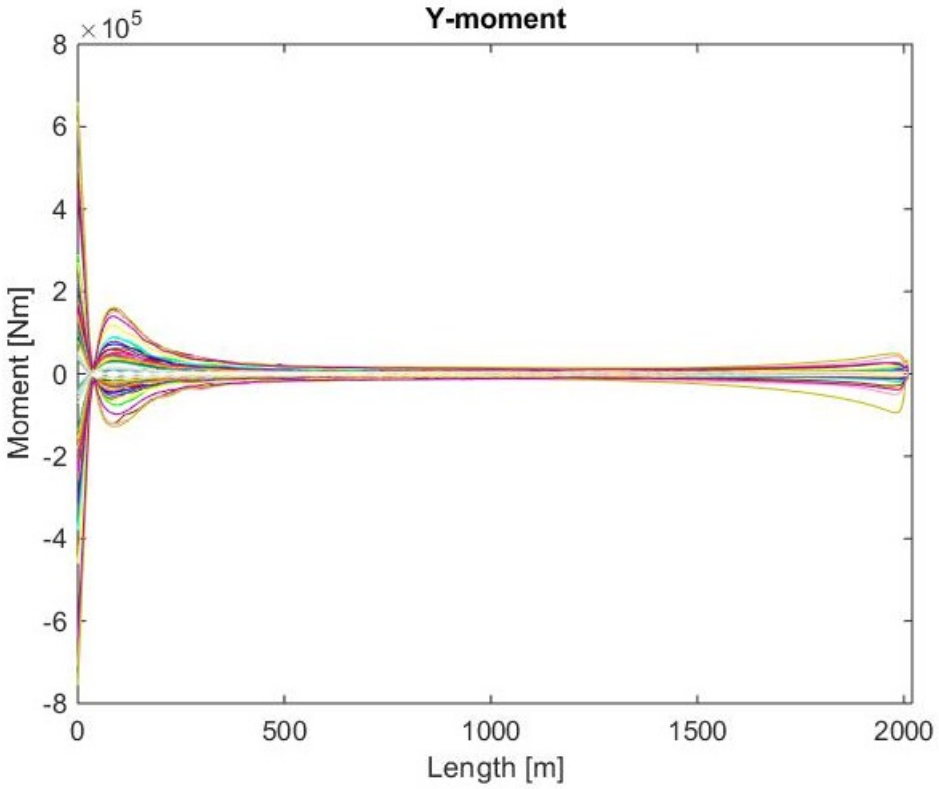

Figure 6.20: Y-moment for all sea states

The highest moments from figure 6.20 are shown in figure 6.21. Sea state 12, 11,10, 9, 8, 7, 6, 5, 4, 3 have the largest moments in the figure. Since sea state 12, 11, 10 and 9 exceeds the limiting condition, the sea states are removed from the results.

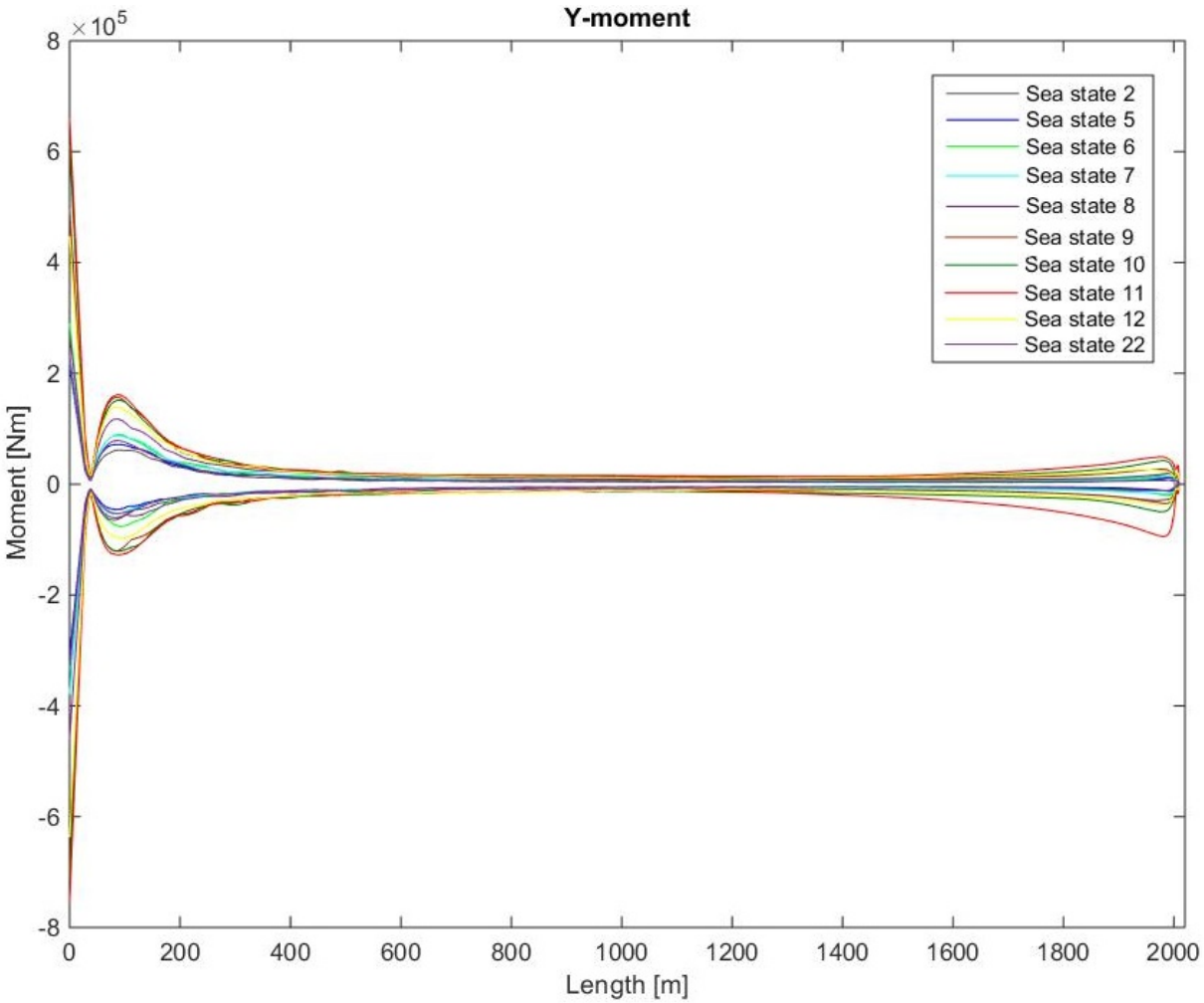

Figure 6.21: Y-moments for the worst sea states

The highest moments within the limiting condition are shown in figure 6.22. The highest moments at the bottom of the riser comes from sea state 8,7 and 6. The highest moments at the top of the riser comes from sea state 4,3 and 5. The dominating moments are however, at the bottom and have magnitude close to 450kNm.

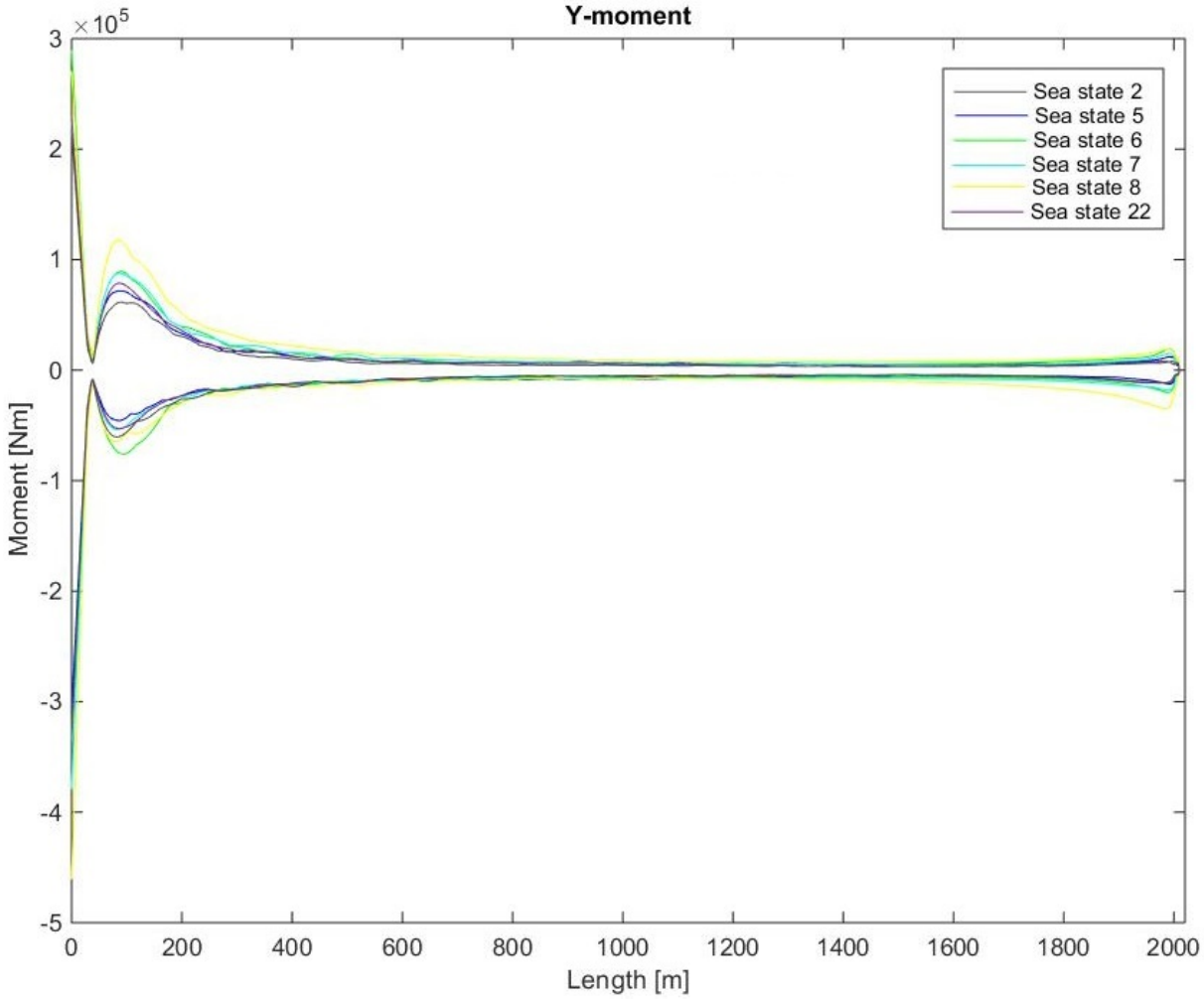

Figure 6.22: Y-moments for the worst sea states within limiting conditions

In order to investigate the moment diagrams with respect to yield, the resultant moment was studied and the worst sea states were selected. The resultant moment was however, obtained for a 1-hour sea state because the results were used in the fatigue analysis. Therefore, a new analysis was run for 3-hours for the three worst sea states from the resultant moment from a 1-hour sea state. The resultant moment for the three worst sea states from the 1-hour analysis are shown in figure 6.23.

The worst sea states from the resultant bending moment are sea state 6, 7 and 8. Sea state 8 gives the highest moment at the bottom of the riser, and sea state 6 gives the highest moment at the top of the riser from figure 6.23. The moment is maximum 475kNm at the bottom, and 250kNm at the top.

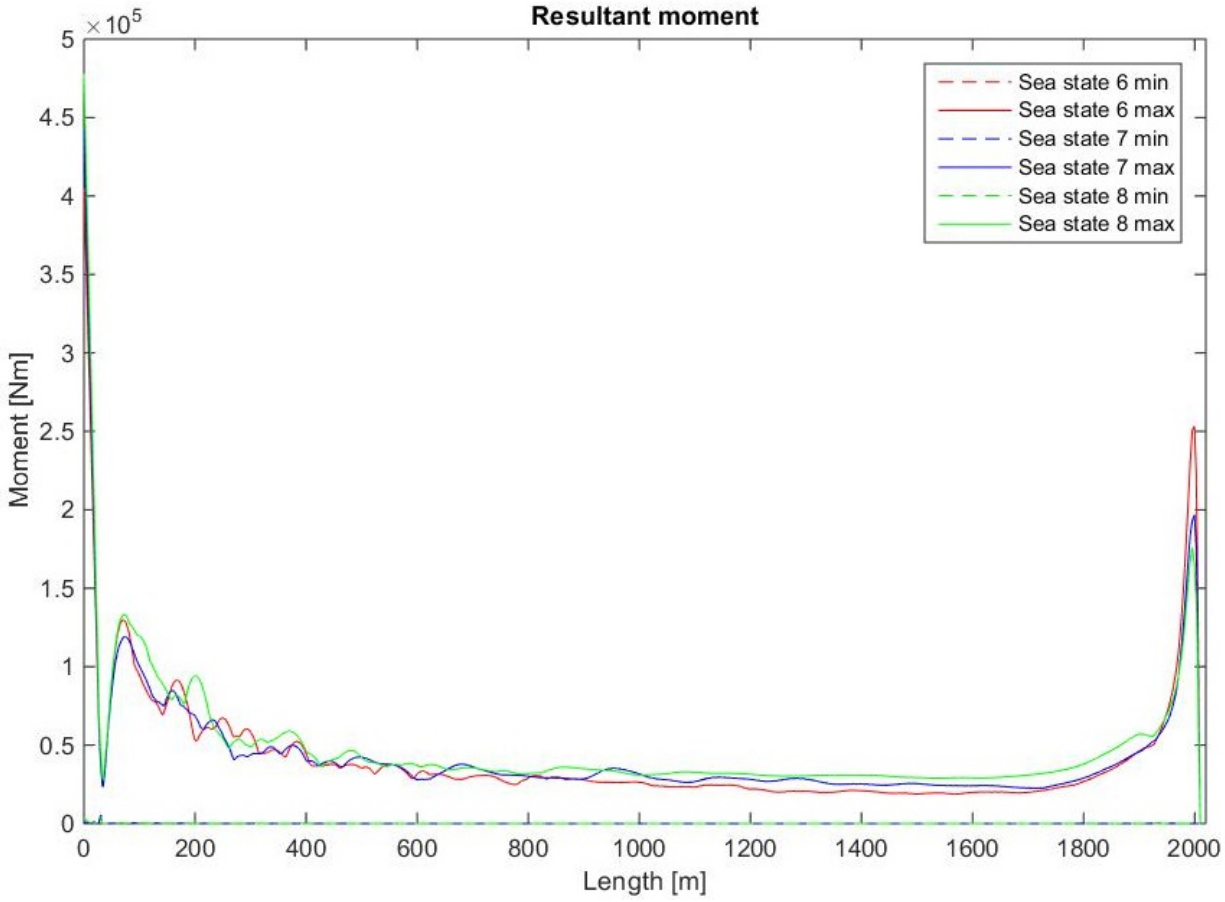

Figure 6.23: Resultant moment, 1-hour sea state

When comparing the moment from the 1-hour analysis with the moment from the 3-hour analysis, it can be observed that the magnitude increases slightly at the bottom for the 3-hour analysis, shown in figure 6.24. The moment increases from 475kNm to approximately 540kNm. At the top of the riser, the moment stays relatively the same.

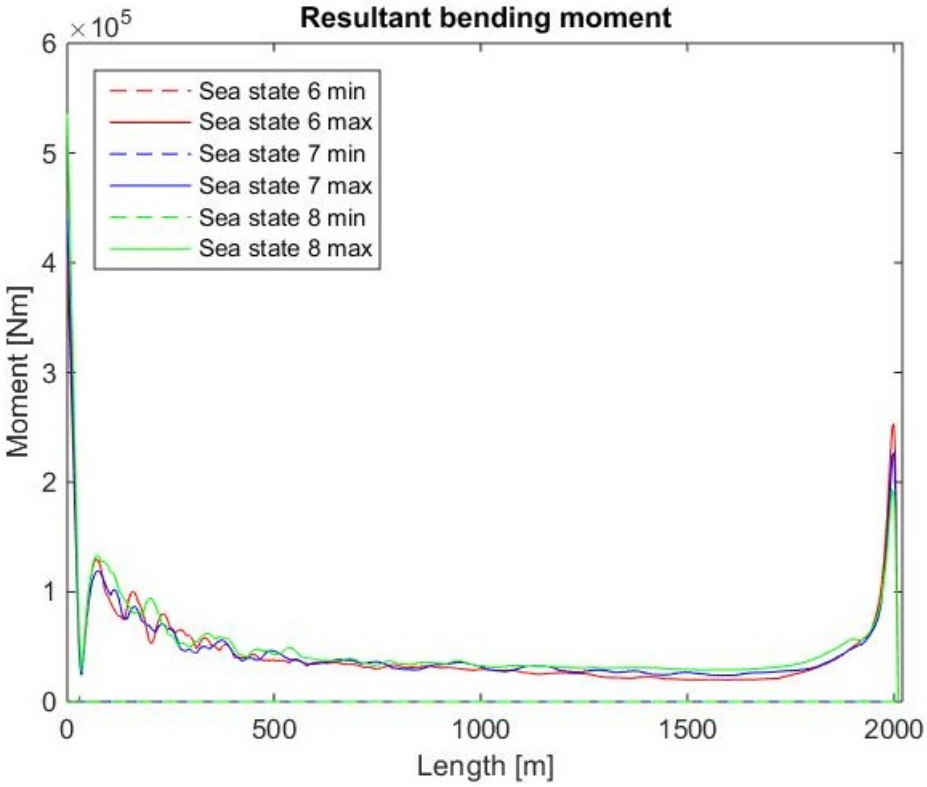

Figure 6.24: Resultant moment, 3-hour sea state

Standard deviation

The standard deviation of the bending moment shows the variation of the moment over the riser. The deviation is highest at the bottom of the riser. Over the length of the buoyancy joint, the deviation is lower, but increases at the end of the riser. Sea state 8 has the highest deviation at the bottom, with a magnitude close to 70kNm.

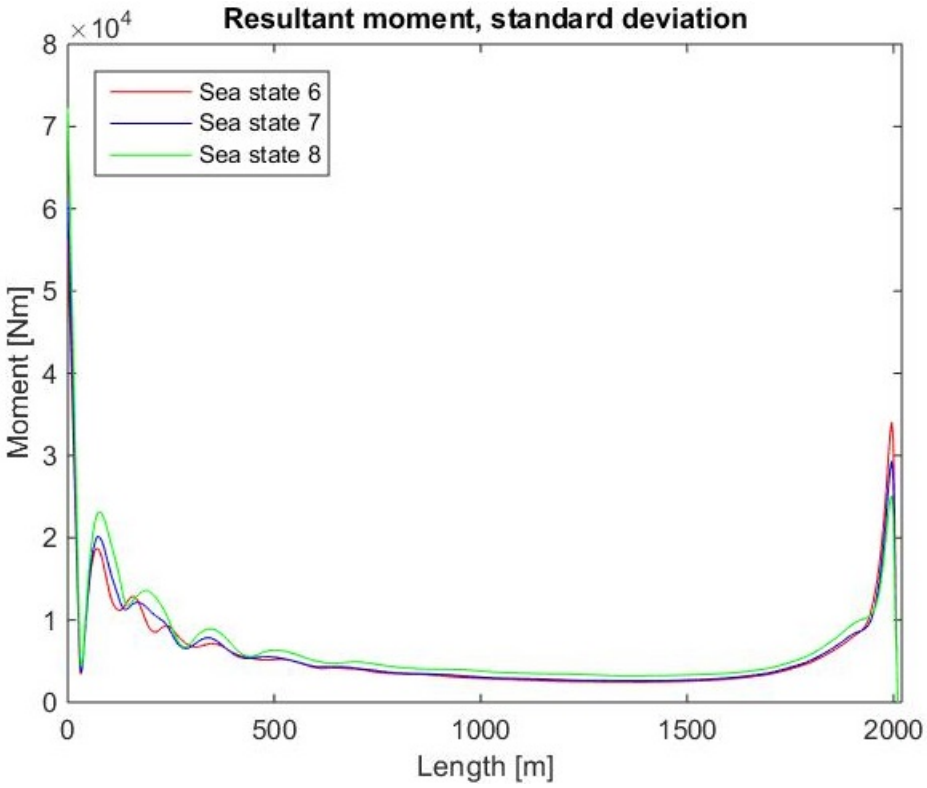

Figure 6.25: Standard deviation, 3-hour sea state

Effective tension

The effective tension increases drastically in the beginning of the riser towards 6MN. Similar to figure 6.2, the bottom of the riser is slightly negative due to the high stiffness of the bottom elements. The effective tension is the same for all of the sea states, but it can be observed that there is a small deviation from the minimum and maximum values for each sea state.

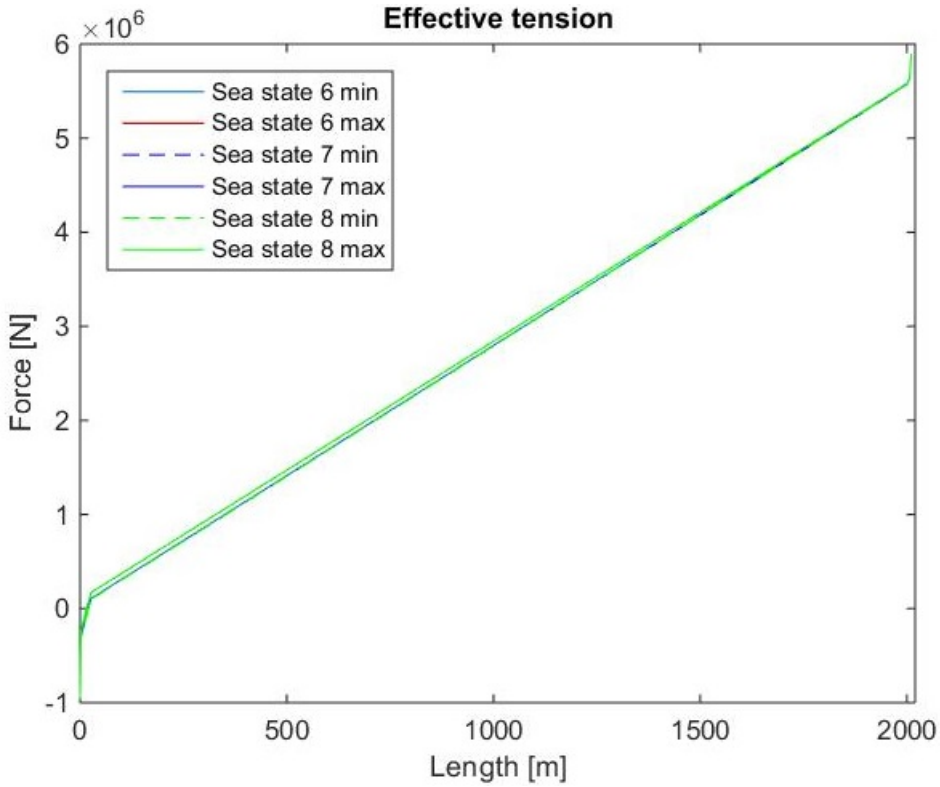

Figure 6.26: Effective tension, 3-hour sea state

Shear force

The shear force is the highest at the top of the riser. Sea state 6 has the highest shear force with a magnitude approximately equal to 40kNm. The shear force for sea state 7 is close to 3.7kNm, while sea state 8 has a shear force close to 3kNm. At the bottom of the riser, the shear force i highest for sea state 8, and is approximately equal to 17kNm.

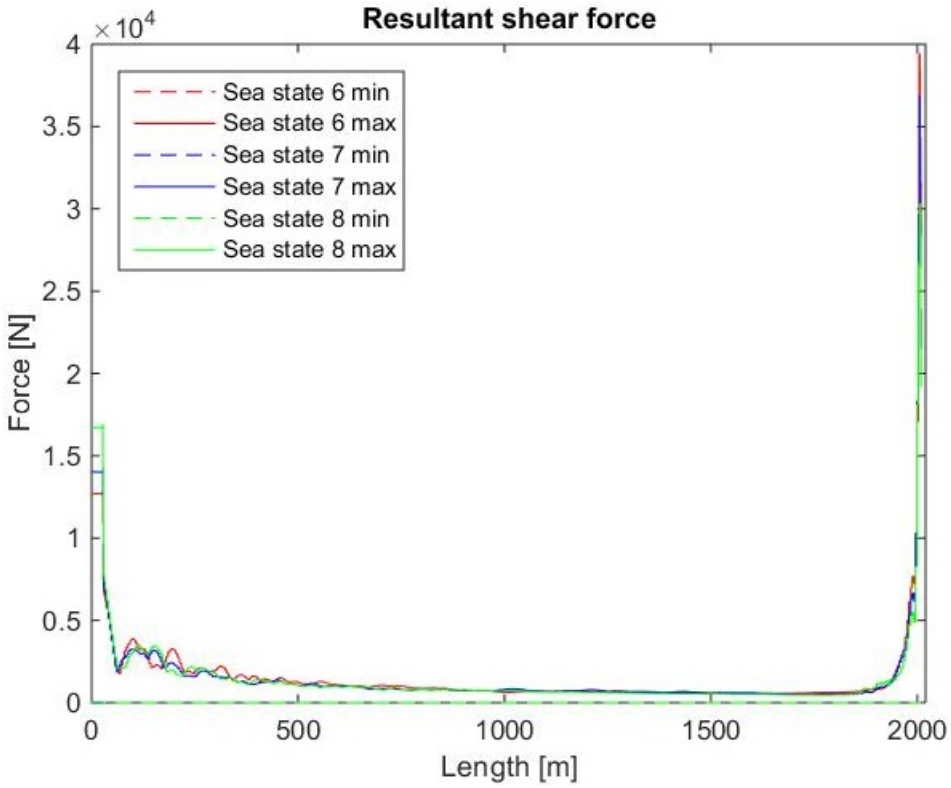

Figure 6.27: Shear force, 3-hour sea state

6.3 Fatigue analysis

Analysis with SCF 1

In the fatigue analysis, when SCF was 1, the results showed no damage over the whole riser. This was unexpected since the moment diagrams showed a great variation over the riser. The axial force was also investigated, but is only presented in the effective tension. Since both the axial force and bending moments had some variation, it was assumed that there would be more axial and bending stress variations. From investigating the output file from the fatigue analysis, it was discovered that the software calculates only damage if the lifetime is below 99999. If the fatigue life exceeds 99999 years, the value is set automatically equal to infinity or 99999. A lifetime of 99999 years is however, quite high and the small damage would most likely not have a significant impact on the riser. In order to see what the damage would be, the damage is calculated by hand calculation and by the equation D=1/N, given in chapter 3.2.4. The damage is then corrected by multiplying it with the correct probability. The results are shown in figure 6.28, 6.29 and 6.30. All three plots give the same results for each sea state because the lifetime exceeds 99999 years.

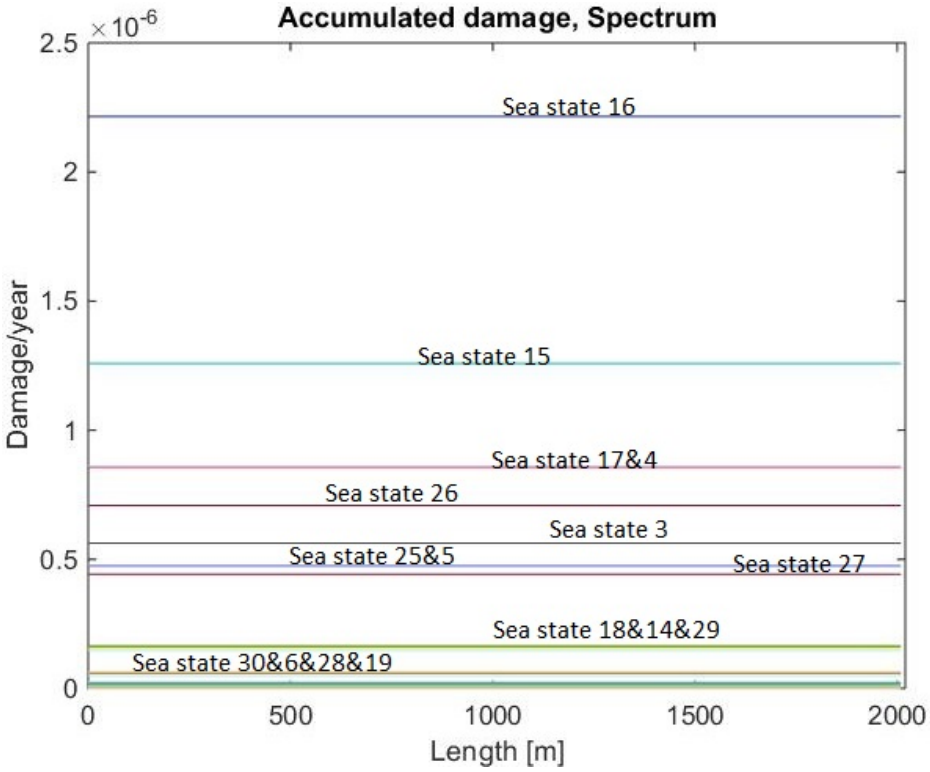

Figure 6.28: Fatigue damage, SCF 1, Spectrum method

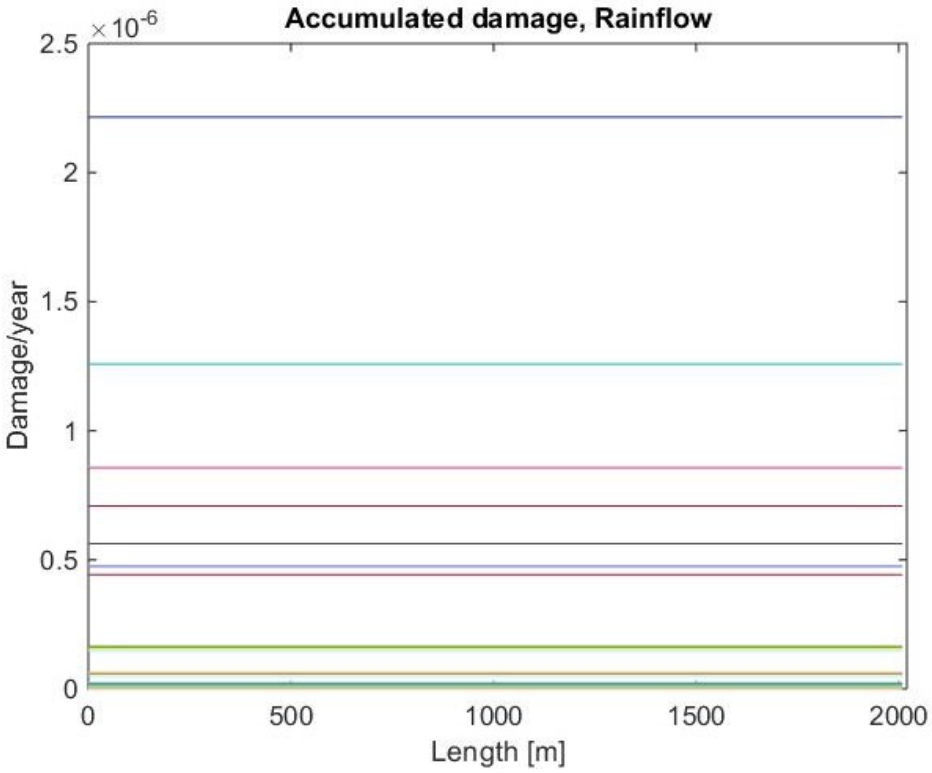

Figure 6.29: Fatigue damage, SCF 1, Rainflow method

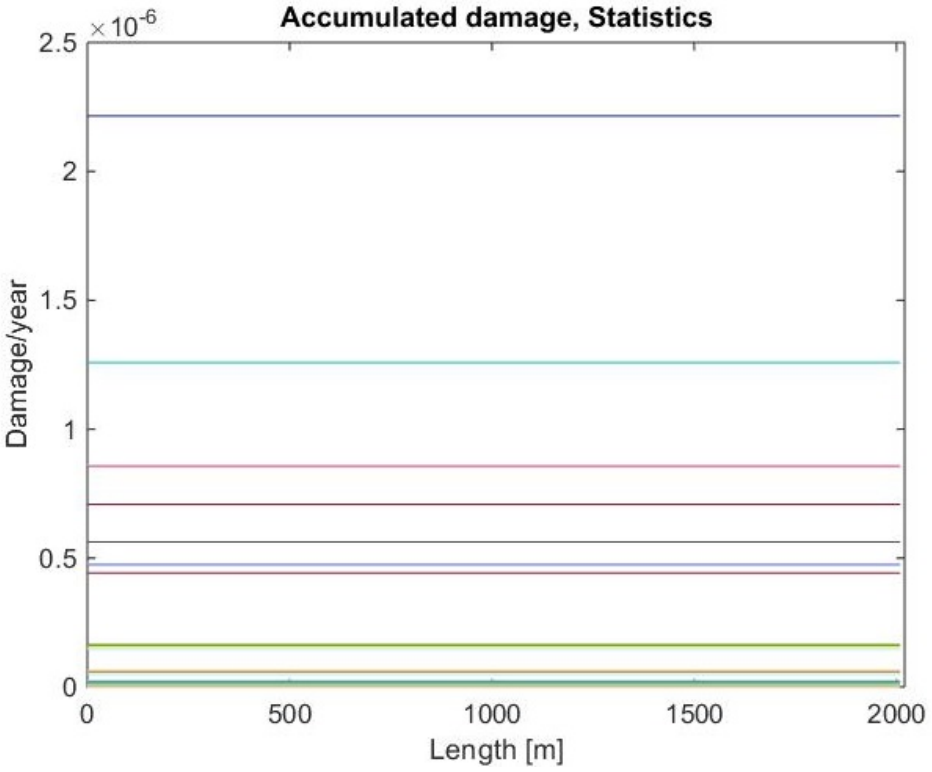

Figure 6.30: Fatigue damage, SCF 1, Statistics method

Analysis with SCF 10

In order to see when the riser would experience any damage, the SCF was increased to 10 and then 20. A SCF of 10 or 20 could be unrealistic, unless the geometry is very special. When the SCF was equal to 10, there were only three sea states that had a different lifetime than 99999 years. The three sea states were sea state 4, 5 and 6. The remaining sea states, which were constant, had a infinite lifetime.

Figure 6.31 shows the fatigue damage for sea state 6, 5 and 4 with the spectrum method. The largest damage occur at the top of the riser, for sea state 4. However, the damage is still quite small, with a magnitude close to 0.9E-5. Sea state 5 has the next largest damage of 0.5E-5. There is also a small change in damage at the bottom of the riser, where the damage is equal to 0.2E-5 for sea state 4, and 0.25E-5 for sea state 5.

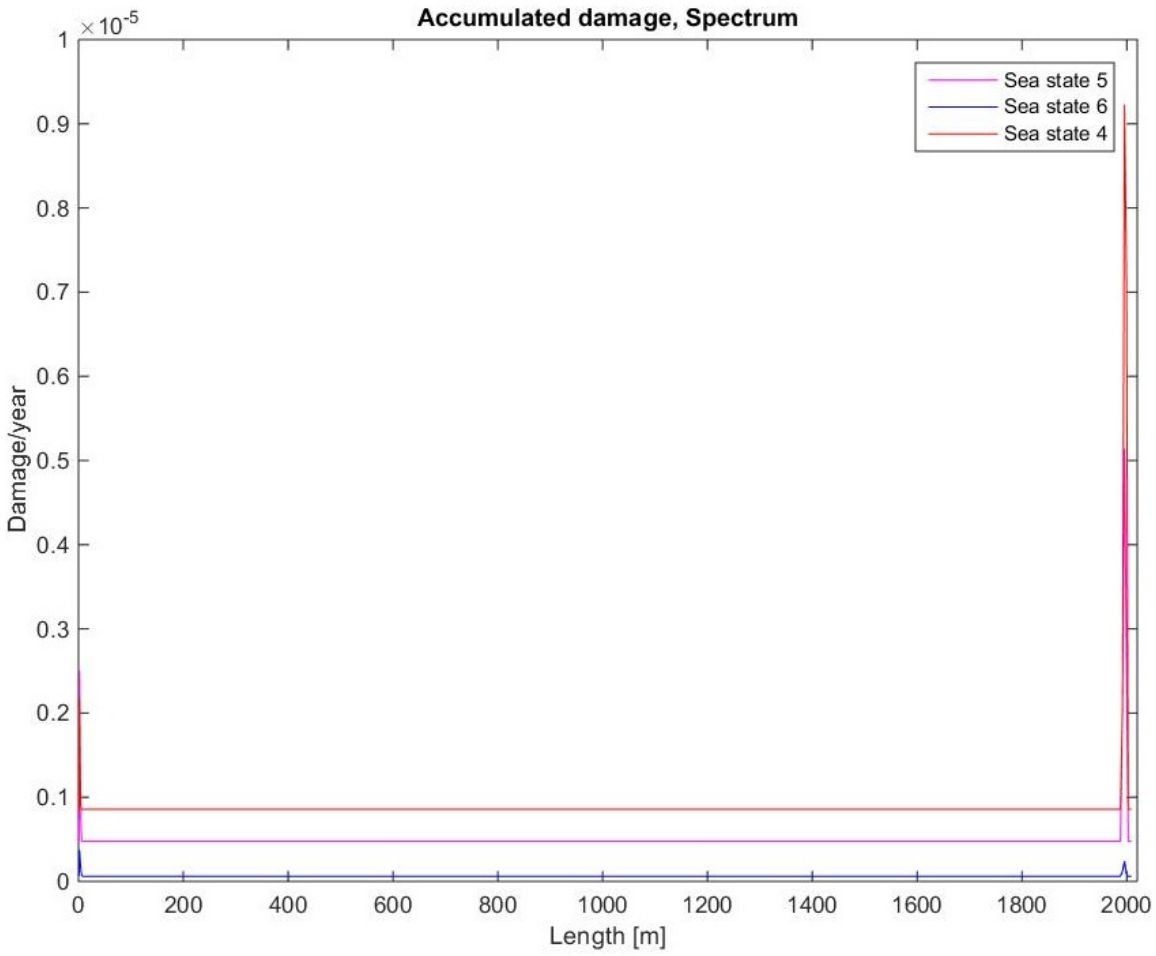

Figure 6.31: Fatigue damage, SCF 10, Spectrum method

The fatigue damage by using Rainflow counting shows that damage increases at the bottom and top of the riser. The damage at the top of the riser is close to 1.5E-5 for sea state 4, and at the bottom the damage is a little bit above 0.5E-5 for sea state 5. Compared to the spectrum method, the damage for sea state 4 with the rainflow method, is significantly higher than the damage from the spectrum method.

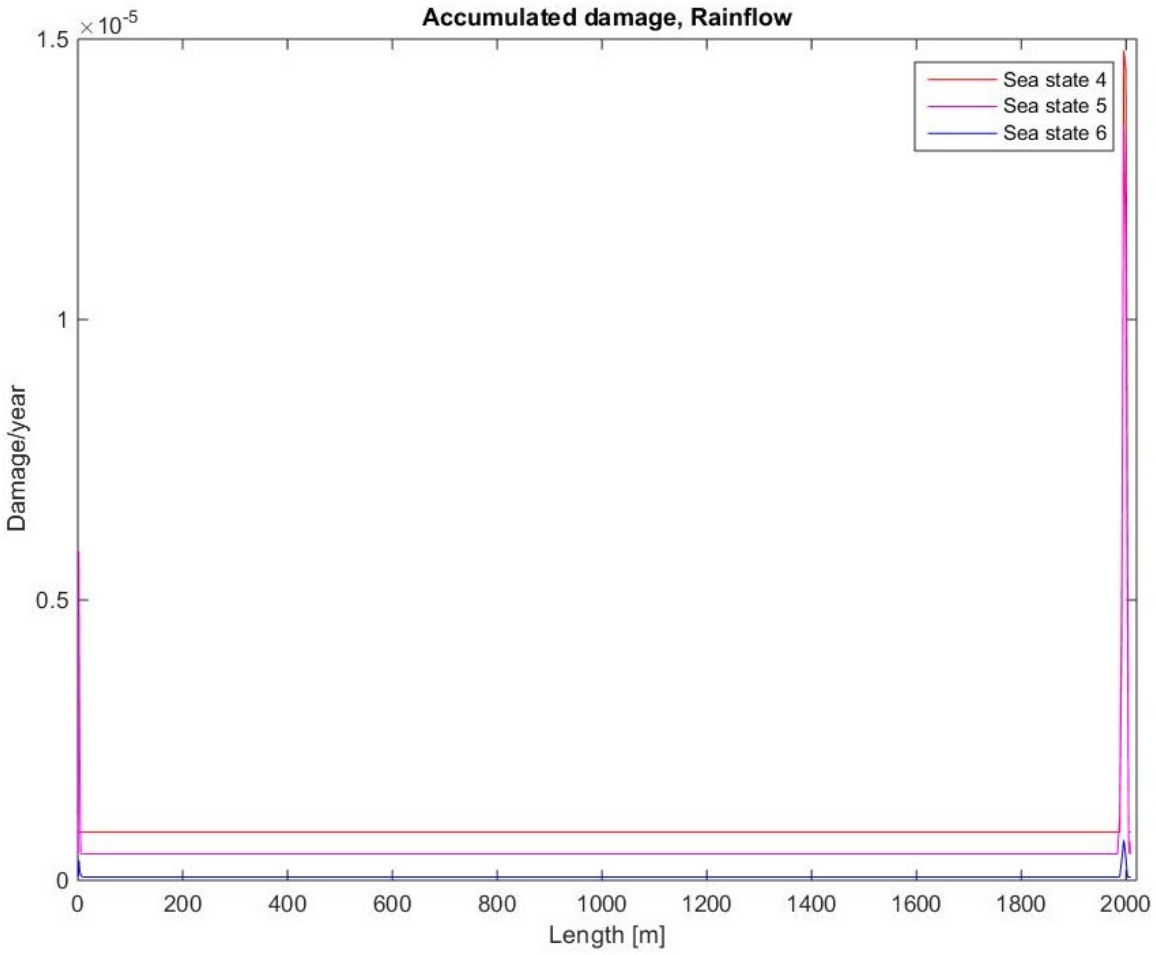

Figure 6.32: Fatigue damage, SCF 10, Rainflow method

Figure 6.31 shows the fatigue damage for sea state 6, 5 and 4 by using the statistics method. The largest damage occur at the top of the riser from sea state 4, and at the bottom from sea state 5. The damage at the top of the riser is close to 1.0E-5, and at the bottom the damage is close to 0.25E-5. If comparing the results from the statistics method with the results from the rainflow and spectrum method, it can be observed that the results from the spectrum and the statistics method are quite similar. The damage at the top of the riser and the bottom is however, higher from the statistics method.

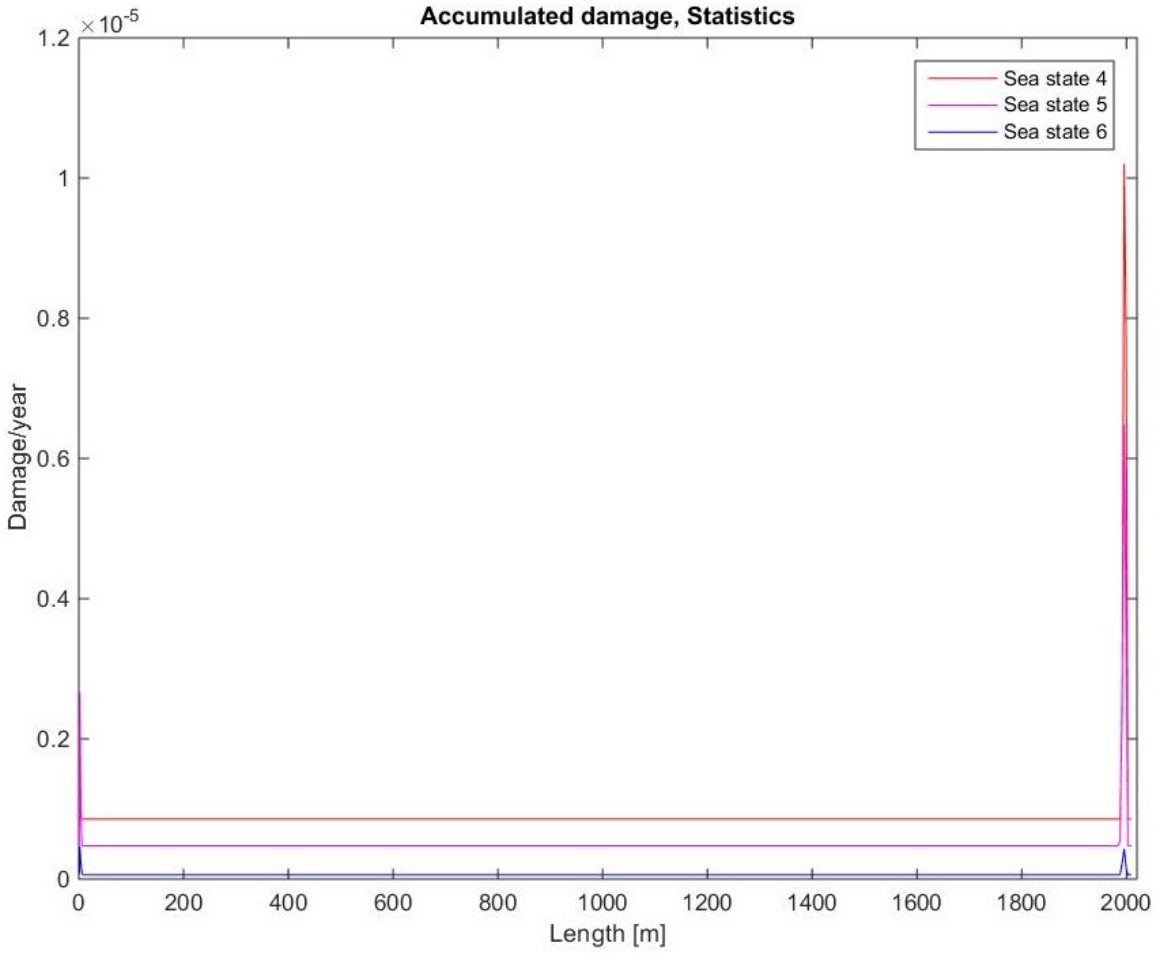

Figure 6.33: Fatigue damage, SCF 10, Statistics method

Analysis with SCF 20

When the SCF is increased to 20, sea state 1-7 and 14-19 show a change in the lifetime of the riser. The remaining sea states, which were constant, had a infinite lifetime.

Figure 6.34 shows the fatigue damage for the selected sea states obtained from the spectrum method. The largest damage occur at the top and at the bottom of the riser. The damage is highest at the top of the riser, where sea state 4 is the dominating sea state. The damage at the top of the riser is 1.18E-3 and 0.42E-3 at the bottom for sea state 4.

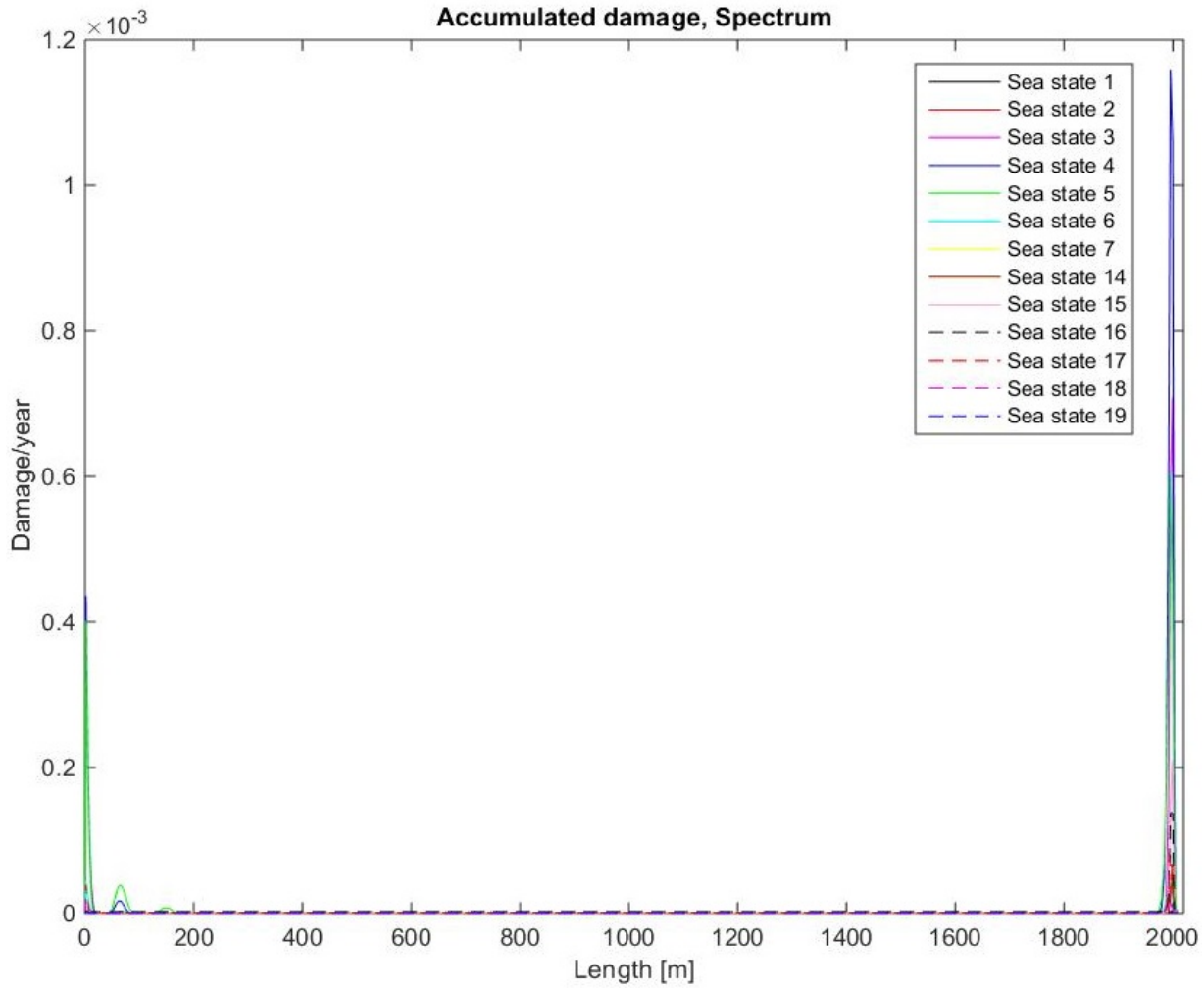

Figure 6.34: Fatigue damage, SCF 20, Spectrum method

A closer look at the damage at the top of the riser, is shown in figure 6.35. Sea state 4 gives the largest damage of approximately 1.2E-3. The next largest damage is given by sea state 3, and is approximately 0.7E-3.

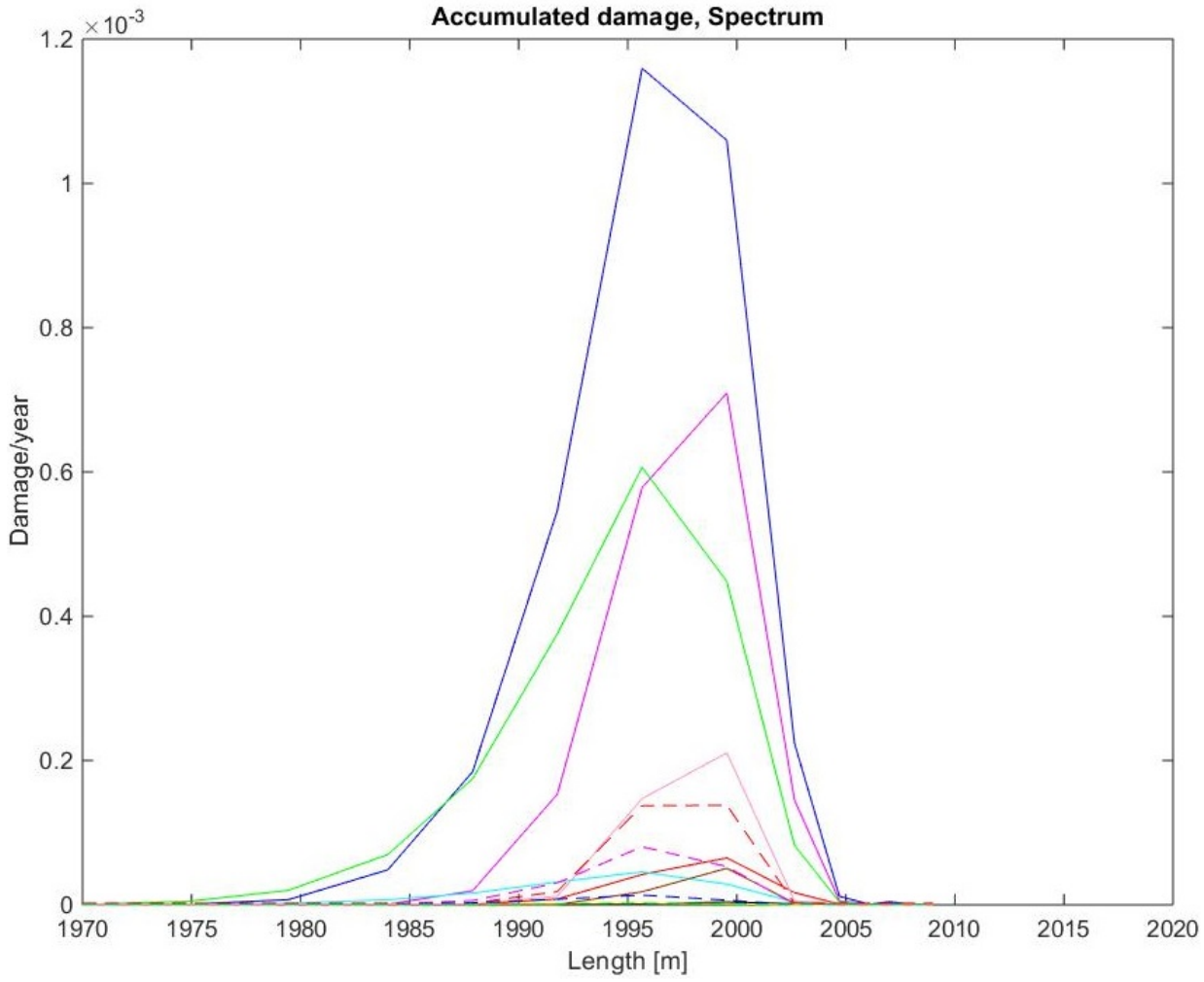

Figure 6.35: Fatigue damage at the top, SCF 20, Spectrum method

Figure 6.36 shows the fatigue damage from using rainflow method. The largest damage also occurs at the top and at the bottom of the riser. The damage is highest at the top of the riser, where sea state 4 is the dominating sea state.

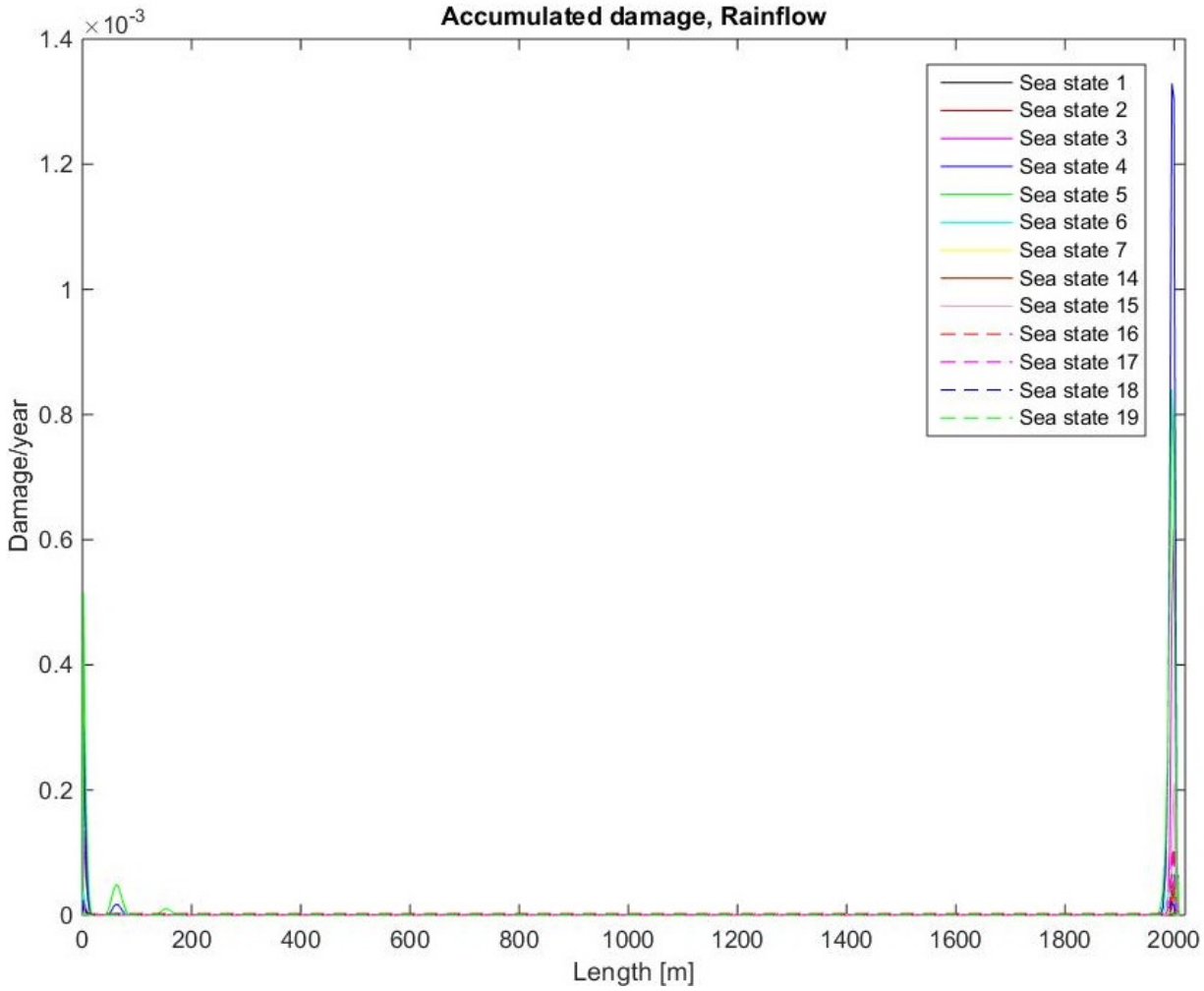

Figure 6.36: Fatigue damage, SCF 20, Rainflow method

A closer look at the damage at the top of the riser is shown in figure 6.37. Sea state 4 gives the largest damage of approximately 1.4E-3. The next largest damage is given by sea state 5, and is approximately 0.8E-3.

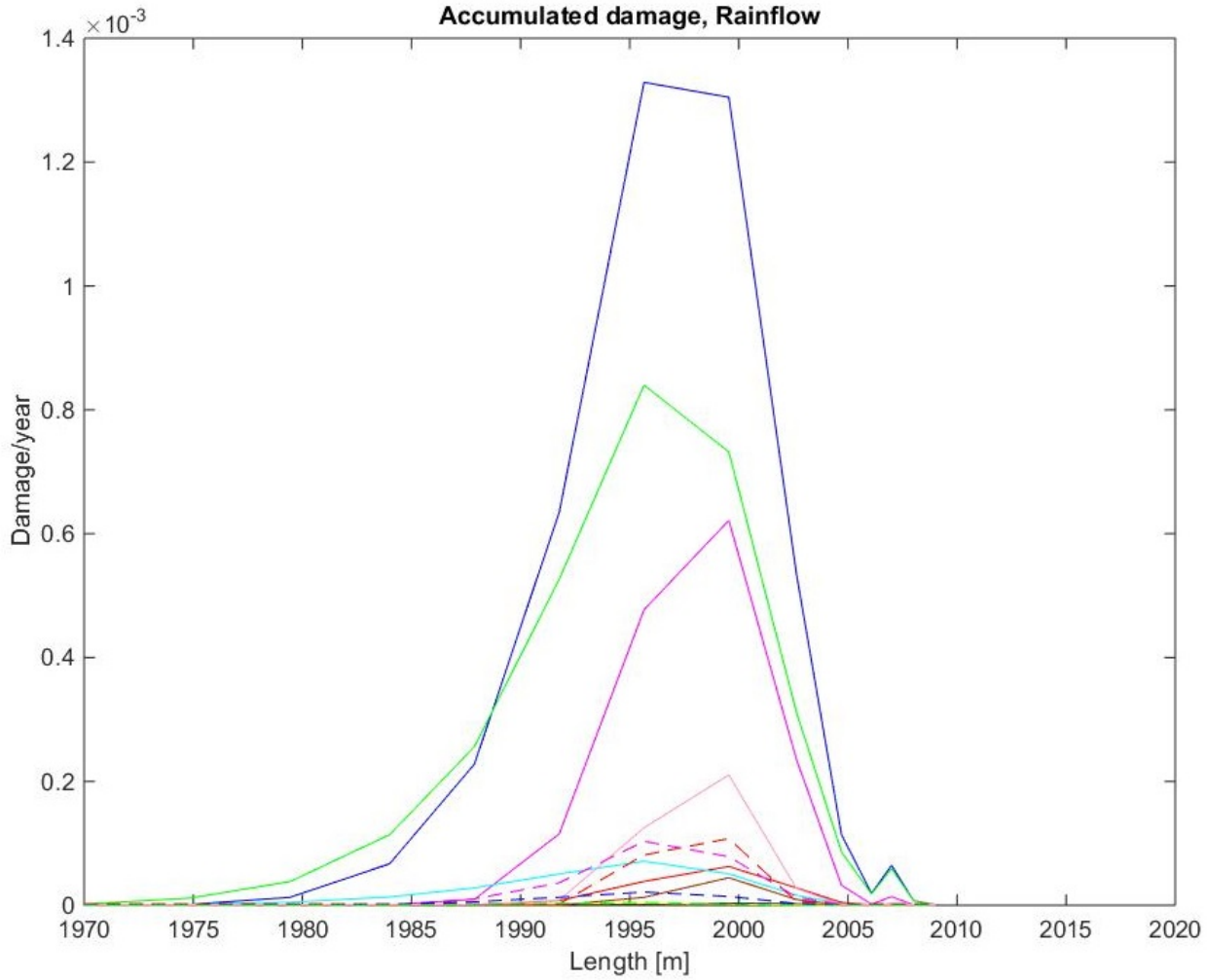

Figure 6.37: Fatigue damage at the top, SCF 20, Rainflow method

Figure 6.38 shows the fatigue damage from using the statistics method. The largest damage also occurs at the top and at the bottom of the riser. The damage is highest at the top of the riser, where sea state 4 is the dominating sea state.

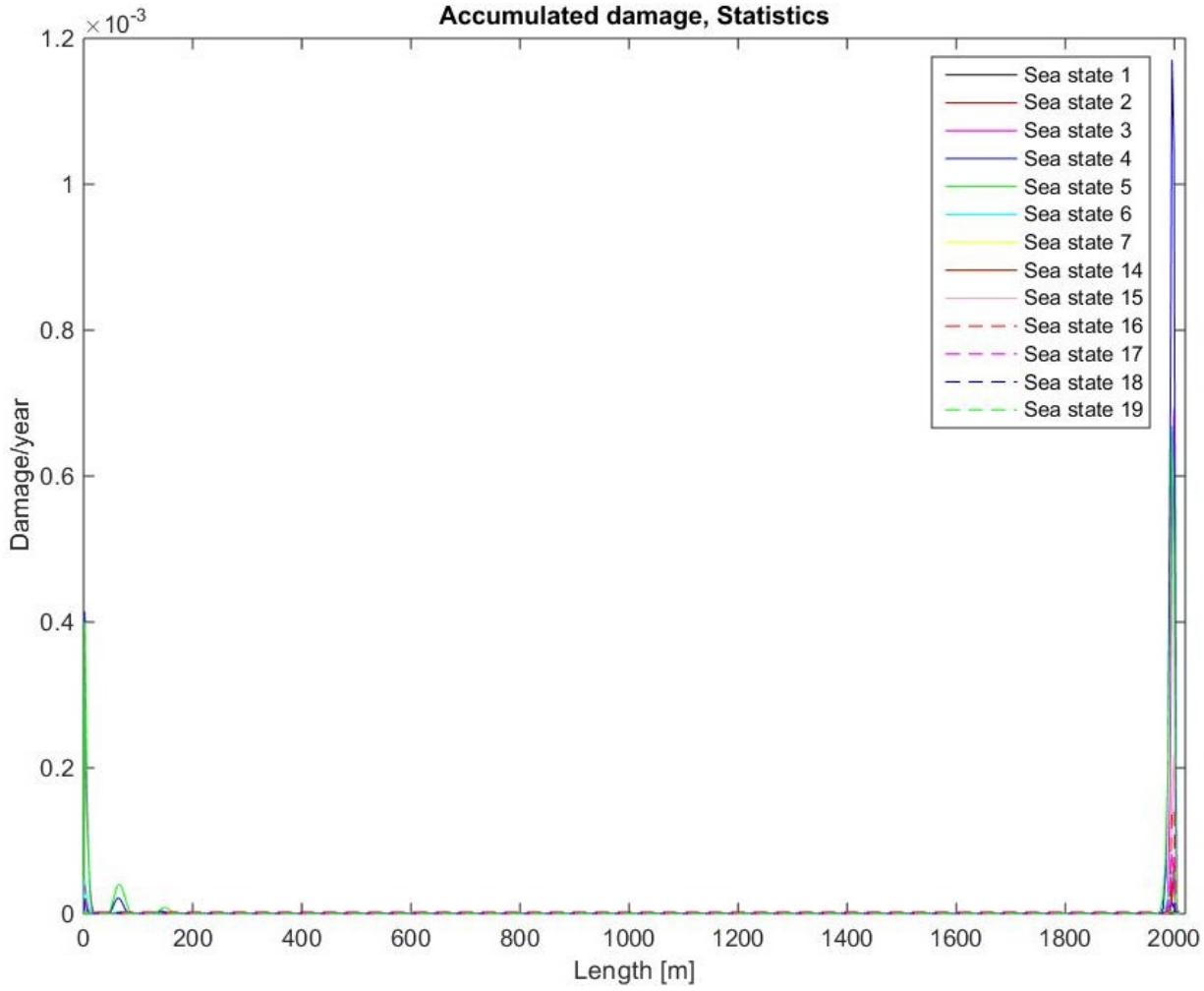

Figure 6.38: Fatigue damage, SCF 20, Statistics method

A closer look at the damage at the top of the riser is shown in figure 6.39. Sea state 4 gives the largest damage of approximately 1.2E-3. The next largest damage is given by sea state 3, and is approximately 0.7E-3. Sea state 5 gives a similar magnitude of damage from sea state 3.

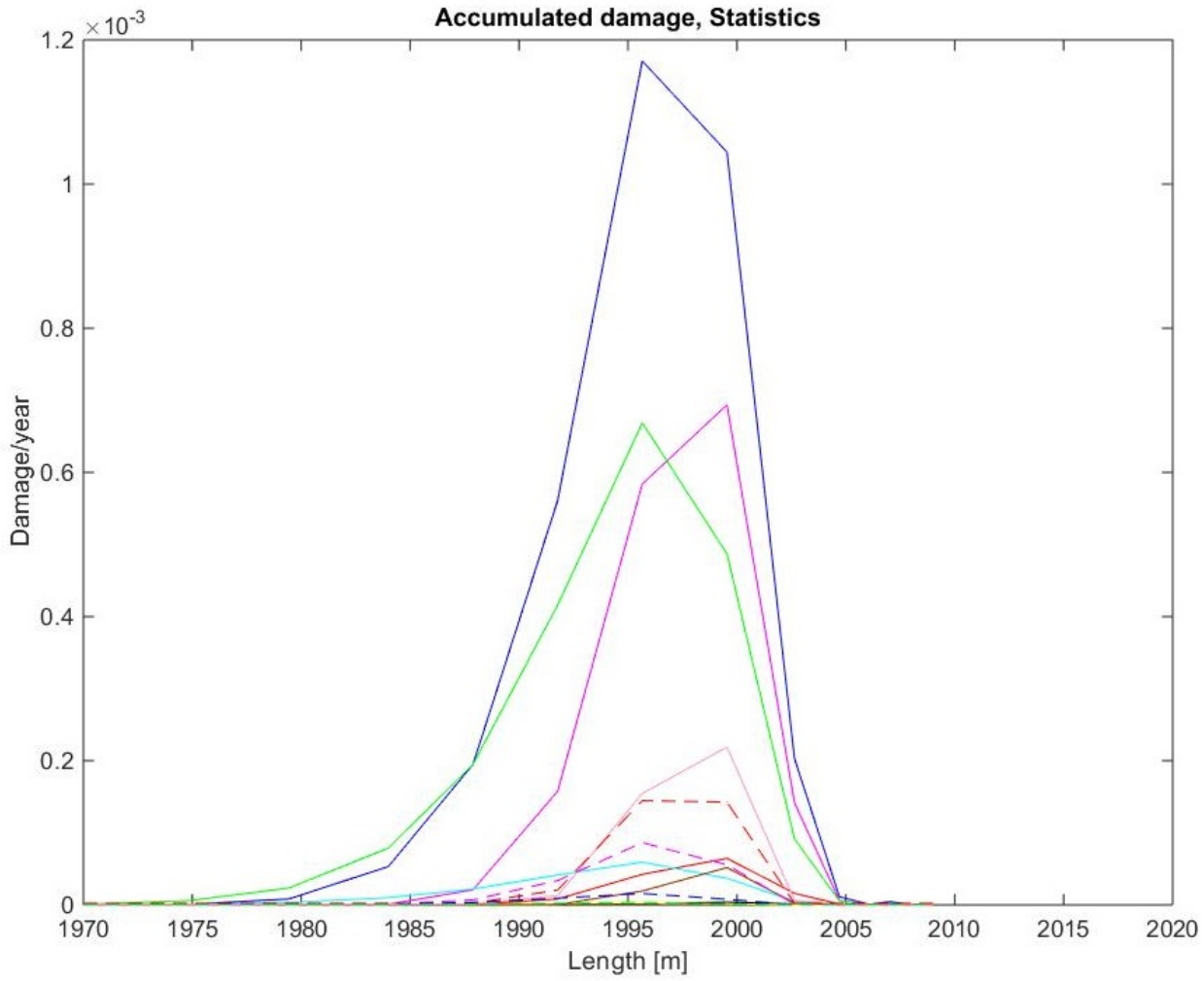

Figure 6.39: Fatigue damage at the top, SCF 20, Statistics method

When comparing the three different figures of the damage with SCF 20, it can be observed that the rainflow method gives the highest damage. The damage at the bottom from the spectrum and statistics method are quite similar. Both the statics and the spectrum method are based on the Rayleigh distributed stress peaks, and the damage was calculated from either standard deviation and mean zero up-crossing period or the combined stress. For the rainflow method however, the damage was found directly from the stress histories and the damage obtained with this method is therefore more accurate than the other two methods. The result from the rainflow

method should therefore be investigated when looking at the response from other drilling riser designs.

Fatigue hand calculations

Four sea states have been selected for further investigations, sea state 4, 5, 15 and 16. Sea state 4 and 5 are selected because they showed a change in the damage when the SCF was increased to 10. Sea state 16 and 15 are also selected because their probability of occurence gave these sea states the highest damage when all the sea states exceeded 99999 years in lifetime. Since Flexcom has limitations for calculating the true fatigue damage, the calculations are performed by hand for a few selected elements based on the stress histograms. The damage is shown in table 6.1.

Sea state	Element	Damage
4	1	3.04397E-12
	27	1.11314E-13
	30	6.70727E-15
	260	1.13576E-13
	466	2.50784E-10
5	1	2.34668E-13
	27	1.08089E-14
	30	8.43038E-16
	260	7.19117E-15
	466	9.72311E-12
15	1	6.70918E-14
	27	1.69715E-14
	30	1.95932E-14
	260	1.83826E-14
	466	1.60542E-11
16	1	3.65906E-13
	27	1.01969E-13
	30	1.88754E-13
	260	5.93358E-14
	466	1.48804E-11

Table 6.1: Hand calculations of damage

The elements selected for the fatigue hand calculations are element 1, 27, 30, 260 and 466. Element 1 is at the bottom of the riser, at the seabed. Element 27 is the element before the flex joint begins, and element 30 is the element after the flex joint. Element 260 is approximately at the middle of the riser, and element 466 is at the waterline at the telescopic joint.

The damage is calculated according to equation 6.2, where $\bar{a}$ and m is taken from the S-N curve from chapter 5.4. Since the stress is quite low, the parameters are taken from the slope which represents cycles over 1.0E+7.

$$D = \sum_{i=1}^{k} \frac{n_i}{N_i} = \frac{1}{\bar{a}} \sum_{i=1}^{k} n_i (\Delta\sigma_i)^m \tag{6.2}$$

The equation should however, only be used when the number of stress blocks, k, is higher than 20. This is to ensure that there is no problem with the numerical accuracy. The number of stress blocks from the fatigue analysis is less than 20 for all the elements. The damage shown in table 6.1 could possibly be incorrect (DNV, 2011a).

The hand calculations show that the damage is highest at the bottom and at the top of the riser. The largest damage occur at the top of the riser. This corresponds well with the results from the analysis. The hand calculations show that the damage is quite small for all of the sea states. The highest damage occur for sea state 4 at the top of the riser. This sea state has also the highest damage at the bottom of the riser. Sea state 5 should, according to the analysis in Flexcom, have the next highest damage at the top, but when comparing the damage with sea state 15 and 16, the damage is lower than these sea states. It is difficult to say why the damage is lower, but it could perhaps be related to the limitations of equation 6.2.

Analysis with no drift motions

The damage from sea state 4, 5, 15 and 16 are compared with the results from SCF 1, 10 and when the analysis does not consist of any second order vessel motions. Figure 6.40, 6.41 and 6.42 shows the comparison for the three different methods.

From all of the figures it can be seen that the damage does not change when second order vessel motions are not applied. The results from the fatigue analysis when SCF was 1, and the results from the fatigue analysis when only RAOs and wave spectrum were defined, are completely the same. This simplifies the methodology greatly because the calculations in Ariane are not necessary. This means that only the RAOs and the wave spectrum should be defined in the analysis. It is possible that the damage could be different when using another design/configuration or changing the water depth of the riser. This should be verified in future studies.

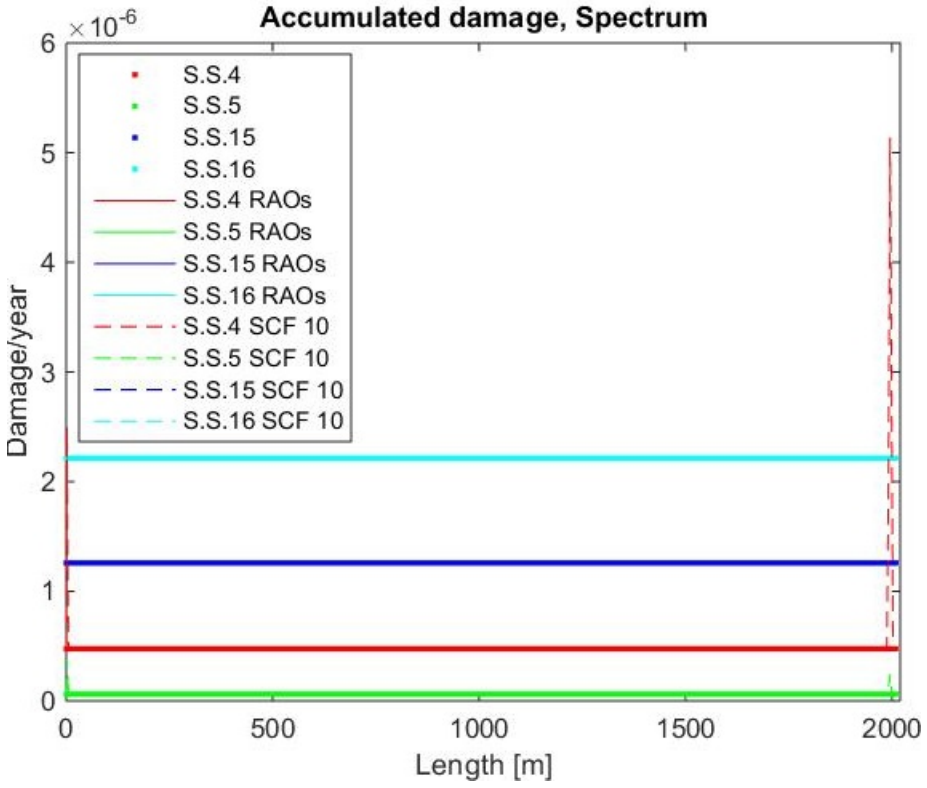

Figure 6.40: Fatigue damage from spectrum method with SCF 1, 10 and no drift motions

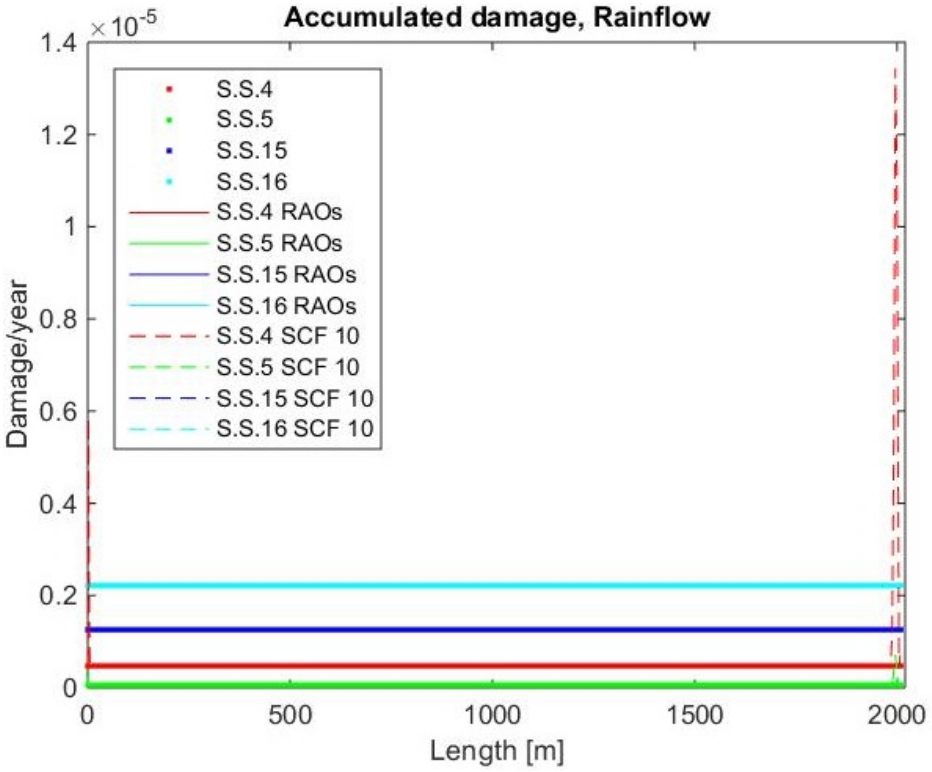

Figure 6.41: Fatigue damage from rainflow method with SCF 1, 10 and no drift motions

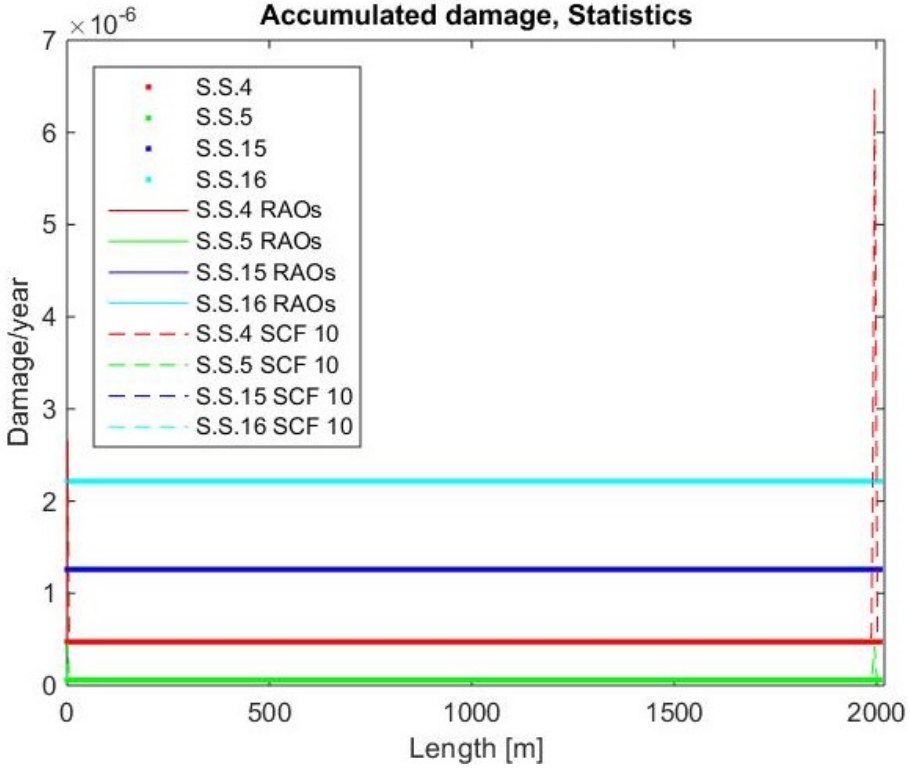

Figure 6.42: Fatigue damage from statistics method with SCF 1, 10 and no drift motions

When comparing the moment diagrams from the time domain analysis with second order vessel motions and without these motions, the result is different for the bending moments in y-direction. The bending moments in y and z-direction from the worst sea state from the time domain analysis, is shown in figure 6.43.

The z-moment shows that the moment is the same, or close to the same, for both analysis. The graph shows that the effect from the drift motions is insignificant, and that the wave kinematics dominate the response. This could be due to the phase difference between the drift motions and the wave motions. Since the WF and LF are out of phase, it is possible that the motions cancel each other. This should be investigated in future studies. For the y-moment the envelope curve is zero for the analysis with no drift motions. This is because the second order vessel motions are applied in y and z-direction, which give a moment in the y-direction. However, for the other analysis, the drift motions are not present and the loads are completely symmetrical about the axes. The environmental loads are the waves and the current, and both of these are applied at zero degrees, which is the y-direction in the model. This explains why the moment is zero. With respect to yield, it is difficult to say if the response from the two analysis will differ. The resultant moment should be compared for the two analysis in order to investigate this possibility. The focus has however been at the fatigue anaysis for the comparison of the two different cases, and from the results in the fatigue analysis the two options give no significant change of the damage.

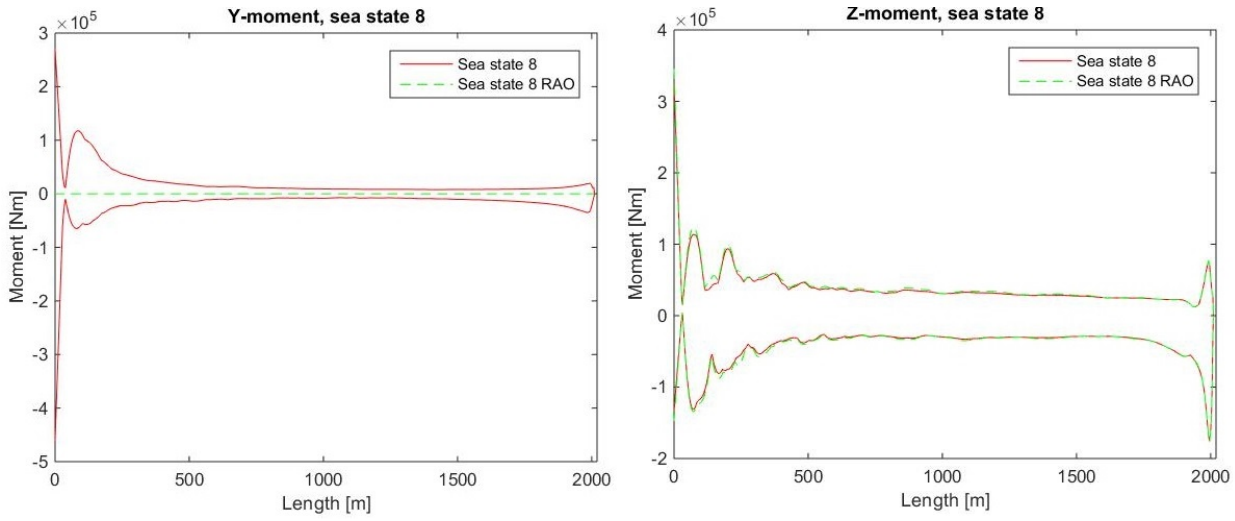

Figure 6.43: Local y and z-moment for sea state 8 with and without drift motions

6.4 VIV analysis

The results from the eigenvalue analysis must be found in order to perform the VIV analysis. In addition, the natural frequencies and mode shapes obtained from the analysis can give an indication how the riser will respond in the dynamic analysis.

As explained in chapter 5.5, the eigenvalues appear in pairs, where one of them is unknown and the other is a pure bending mode. The first seven eigenmodes and eigenvectors are found, but only the pure bending modes are presented in this chapter. The pure bending modes are found for both with and without current. The eigenfrequencies are given in table 6.2. The results in the table show that there are very little differences between the eigenvectors with current and without current. Additionally, the table shows that the eigenperiod is decreasing when the eigenvector is increasing. This is correct, because when the number of modes increases and the total length of the riser is fixed, the eigenperiod for each mode have to decrease.

Eigenvector	Eigenperiod no current [s]	Eigenperiod w/current[s]
1	113.29	113.23
3	55.14	55.12
5	36.36	36.35
7	27.03	27.02

Table 6.2: Eigenfrequencies and eigenperiods

Eigenmode 1, 3, 5 and 7 are compared to the expected shape, $sin(\frac{n\pi x}{L})$, where L is the total length of the riser (Larsen, 2014). When n equals one in the expression for the expected shape, mode 1 in figure 6.44 has a similar shape. When n equals 2, the expected shape is similar to the shape for mode 3 in figure 6.45. The same goes for mode shape 5, represented by figure 6.46 and mode shape 7, represented by figure 6.47. From these observations the results seems to be correct.

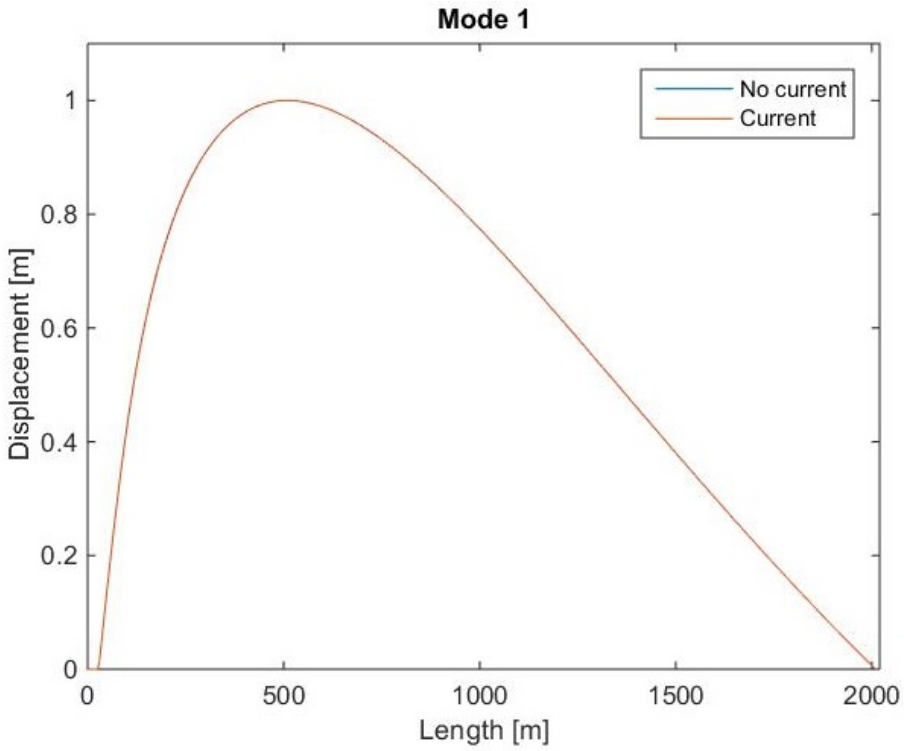

Figure 6.44: Eigenmode 1

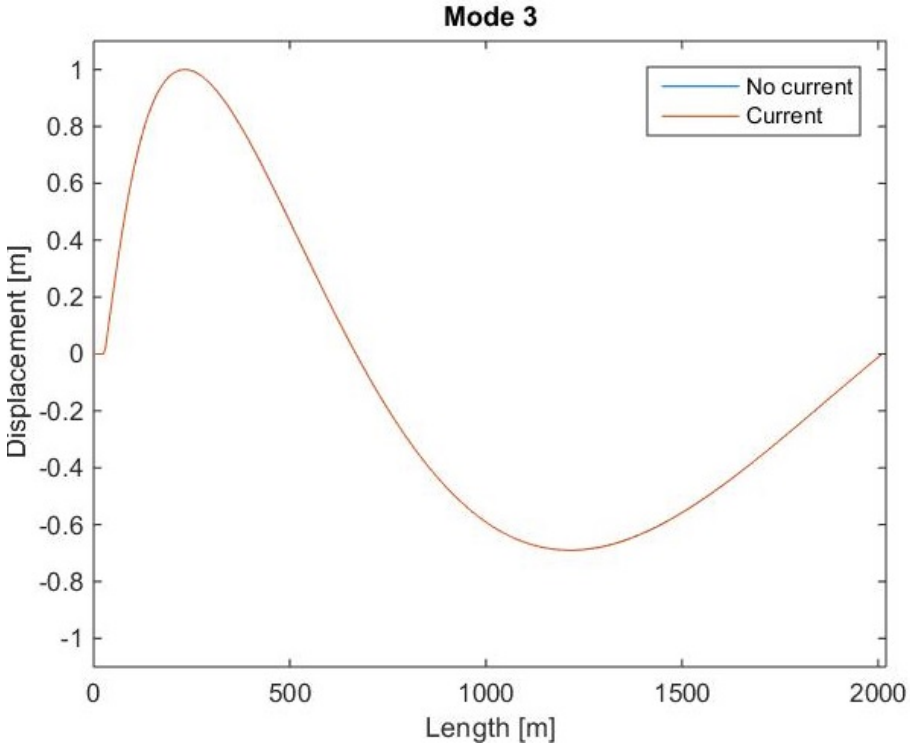

Figure 6.45: Eigenmode 3

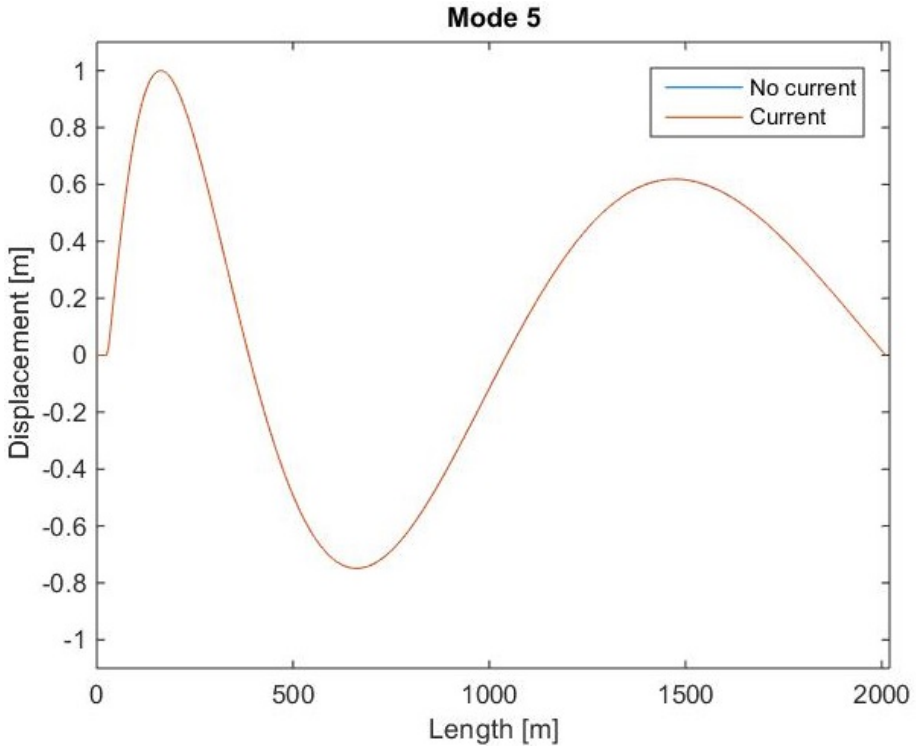

Figure 6.46: Eigenmode 5

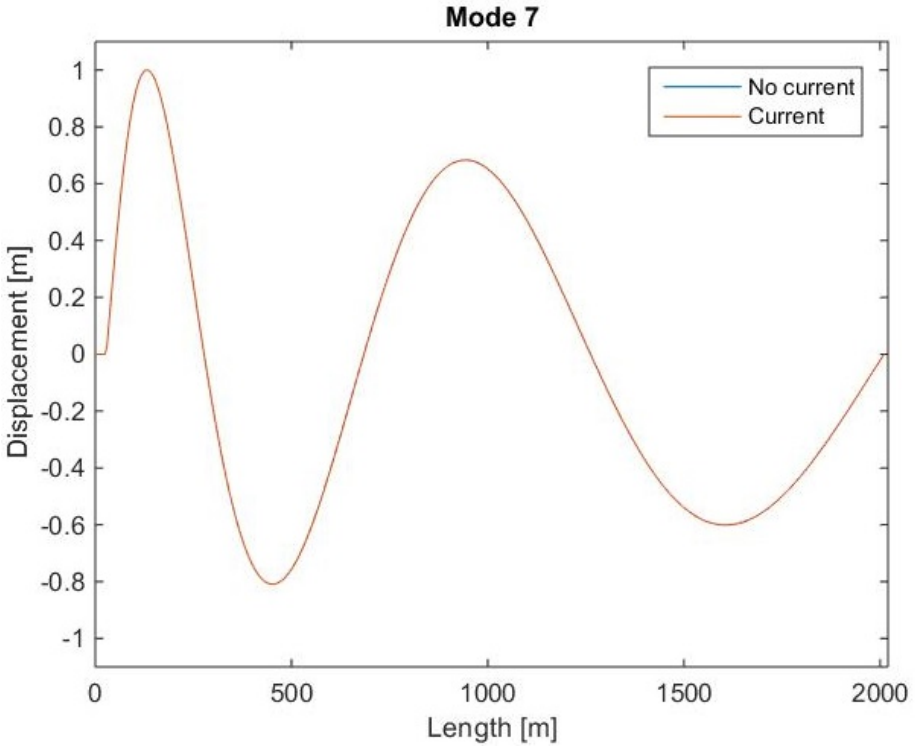

Figure 6.47: Eigenmode 7

In order to investigate if the bending modes from the eignvalue analysis are pure bending modes and not mixed modes, the maximum curvature for the modes should increase monotonically. The maximum curvature is given in figure 6.48. The graph without current is increasing monotonically. However, the graph with current has a local maxima at node 31. This means that mode 31 is a mixed mode, and needs to be removed for the Shear7 analysis. When mode 31 is removed, the graph will look like figure 6.49.

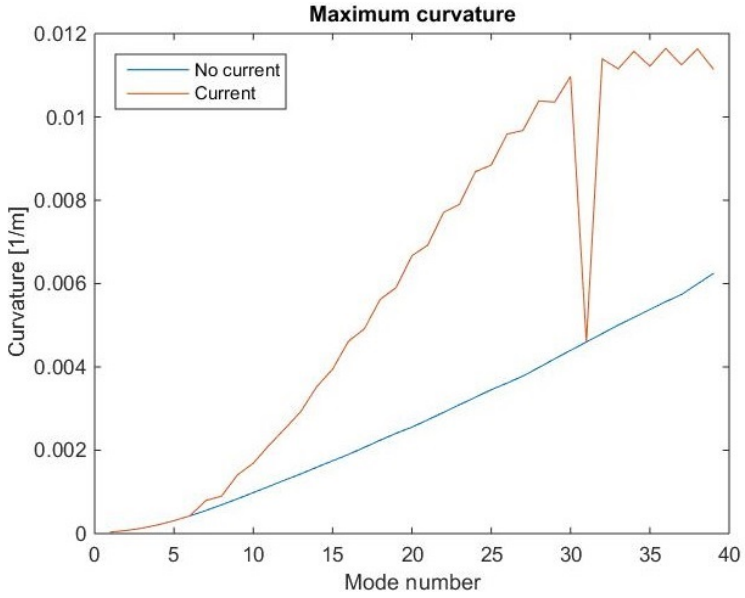

Figure 6.48: Curvature of bending modes with and without current

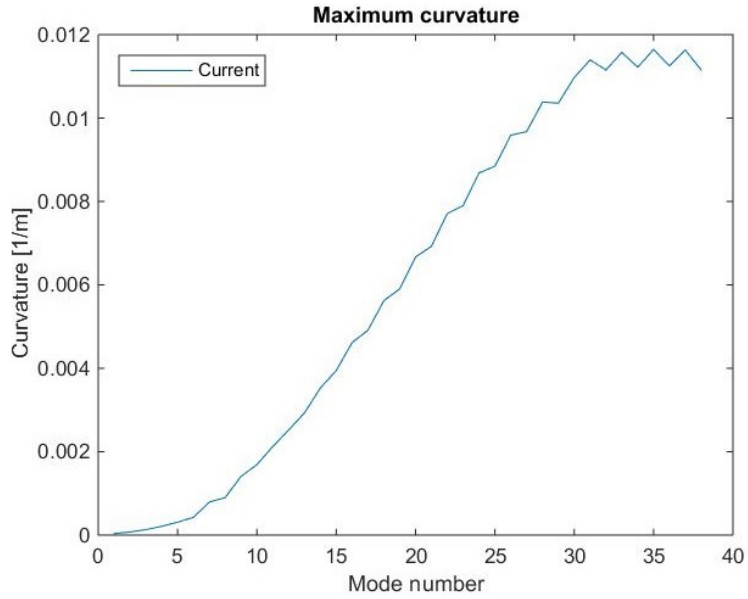

Figure 6.49: Modified curvature plot for current

The results from the VIV analysis with SCF 1 is shown in figure 6.50. The VIV analysis was performed for the eigenvalue solution with and without current, but from the graph it can be observed that the results remain the same with and without current. Since the current also had to be defined in the Shear7 analysis, it was possible that there would be a double effect when using the eigenmodes with current. However, from the results it seems that this has not affected the graph. The reason for this is probably because the eigenmodes with and without current were quite similar. However, for another riser design/configuration the effect could contribute to a more significant change in the graphs, and should therefore be investigated in future studies.

From the figure the damage is highest at the bottom and at the top of the riser. The damage is around 1.13E-5 at the bottom, and close to 0.4E-5 at the top. The damage is close to constant from 500m from the seabed to around 1900m.

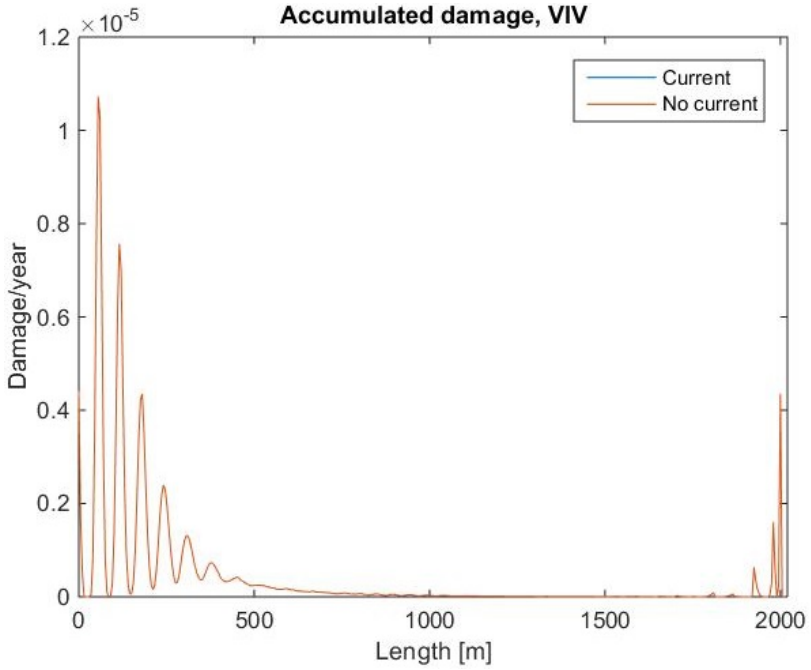

Figure 6.50: Fatigue damage from VIV with SCF 1

A new analysis was performed with a higher SCF in order to see how the response would change. With a SCF of 1.3, the damage can be found in figure 6.51. The figure shows that the damage is still quite low, but it has increased at the bottom of the riser to 4E-5 and at the top to 1.5E-5. When the SCF is increased to its maximum value 9, the results show that the damage is quite high. The damage at the bottom is close to 0.46 and at the top the damage is close to 0.22.

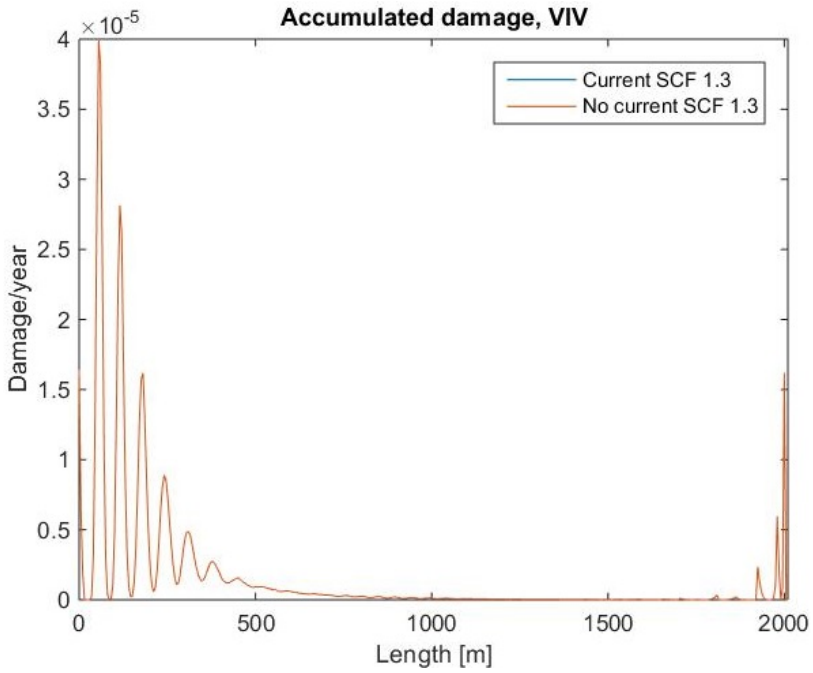

Figure 6.51: Fatigue damage from VIV with SCF 1.3

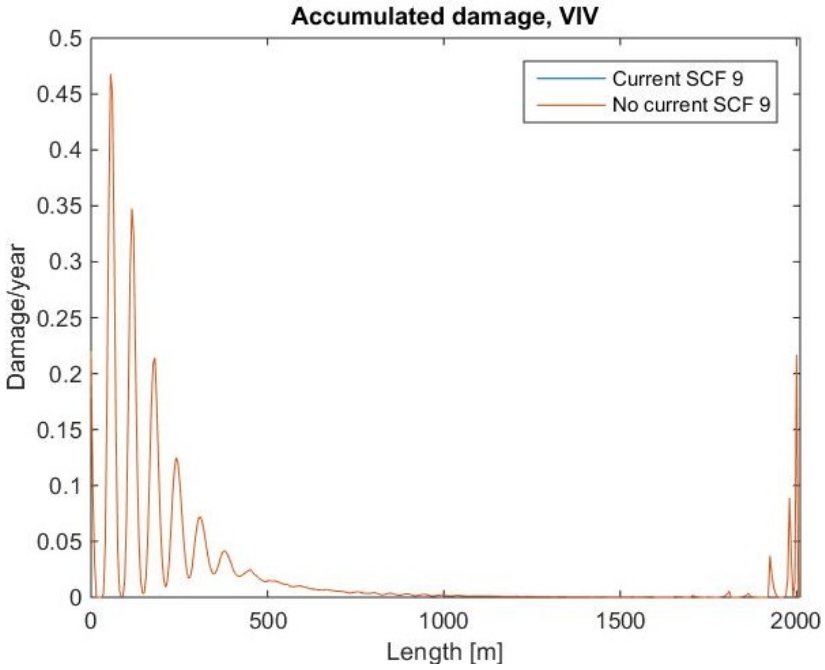

Figure 6.52: Fatigue damage from VIV with SCF 9

6.5 Uncertainties

The results for the marine drilling riser is based on assumptions, simplifications and experimental data. It is therefore important to be aware of these uncertainties when evaluating the data obtained from the analysis. Some of the uncertainties are presented below.

6.5.1 Simplified model

The design of the riser is very simplified in the analysis. The different components, such as the BOP and LMRP, have a complex and detailed geometry. This has however, not been considered in the analysis. The results from the analysis could therefore be quite different if the model was designed with more details.

6.5.2 Finite element method

The program is based on the finite element method (FEM), which is an approximate method. Uncertainties from for instant the choice of element type or number of elements for each segment, could affect the results. The maximum element length for the buoyancy joint was changed in the analysis from 1m to 4.6m, in order to decrease the computational time. The stiffness transition from one element in one segment to another element in another segment did however not exceed a factor of 2. For future studies, a sensitivity study could be performed with 1m maximum element lengths for the buoyancy joint, in order to see if this changes the results.

6.5.3 Damping

Damping from the auxiliary lines and the velocity dependent bending moment of the flex joint, is not included in the analysis. In addition, the interaction between the soil and the template to the wellhead system, is not included in the analysis. Damping contributes to reduce the dynamics, which can reduce the fatigue damage. By not including these contributions of damping, the results from the analysis will be non-conservative (Holm et al., 2013).

6.5.4 Drag coefficient

The drag coefficient is a function of the Reynolds number, and the Reynolds number depend on the velocity and the hydrodynamic diameter. For Reynolds number between 50 and 2.0E+5, the drag coefficient is almost a linear function. Between 2.0E+5 and 5.E+5, the wake of the cylinder becomes more narrow, which leads to a lower pressure gradient and a drop of the drag coefficient. When the Reynolds number increases again, the drag coefficient will gradually increase again. In the analysis the drag coefficient is equal to one for all components, but it should in reality be varying (Chakrabarti, 2005).

6.5.5 Seed number

The seed number was set equal to 0 in the analysis. The seed number could have an impact on the results and a sensitivity analysis should therefore be conducted in order to investigate if the fatigue damage changes.

6.5.6 Number of segments in VIV analysis

The number of segments from the element set in the eigenvalue analysis must be defined as a positive non-zero number. This number could affect the results significantly. From the output file in the Shear7 analysis, the suggested number of segments should either be equal or greater than 180. A sensitivity analysis should therefore be performed in order to see the effect from this parameter.

6.5.7 Environment

The scatter diagram used in the analysis, are based on a metocean report provided by Bureau Veritas (Bureau Veritas, 2016a). The data in the scatter diagram are based on predictions and historical data obtained over a certain period. The data will always consist of uncertainties. In addition directional spreading of the waves is neglected. If this effect was taken into account,

the waves would hit the rig out of plane, which results in movement of the BOP in two planes. The BOP would move in circles, which would reduce the fatigue damage (Holm et al., 2013).

6.5.8 S-N curve

The S-N curves are based on experimental data and the "Safe-life" design approach. This means that the intercept of the log N axis is given by the mean minus two standard deviations. This is a conservative approach and the probability of failure is 2.5%. When comparing this to the "Fail-safe" design approach, which is the mean minus one standard deviation, the probability of failure becomes 15%. The difference in the probabilities show a great difference in the degree of conservatism of the results. Figure 6.53 shows the regressions lines for a) the mean fatigue life, b) mean minus one standard deviation and c) mean minus two standard deviation (Almar-Næss, 1985).

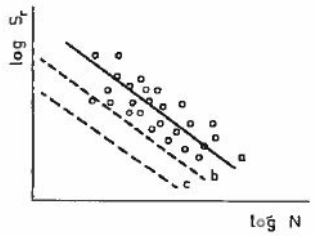

Figure 6.53: Regression lines for S-N curve (Almar-Næss, 1985)

6.5.9 Miner summation

The Miner rule does not take stress interaction into account. Since the fatigue is due to cycle loading, the damage is connected to all of the cycles. The load histories give stress variation around a constant mean level. Due to interaction effects, the miner sum becomes smaller than one. From tests a mean value of 0.5 has been found, and is suggested in a relative miner sum. However, the design codes use a failure criterion equal to one, and therefore overestimates with a factor two on the cumulative fatigue life. Even though failure criterion is set to one, most standards require a Miner sum lower than one for certain type of structures, because of a need for an additional safety factor due to difficulties for repair and maintenance (Almar-Næss, 1985).

Chapter 7

Conclusion

The main goal for this thesis was to develop a methodology for the mechanical assessment of marine riser joints during drilling operation. A model has been established for a global, fatigue and VIV analysis, and sensitivity studies of SCF, application of drift motions, type of drift motions, boundary conditions and current directions, have been carried out. The model has been created based on the literature study of existing technology and rules and standards.

From the global load analysis, the boundary conditions at the top of the riser were investigated both with fixed and free rotations. The results showed a great increase in the bending moment at the top of the riser when the rotations were fixed. The difference between the moments were 2.8MNm, which led to the conclusion that the rotations should be free. The investigation of current direction showed that the critical spots on the riser were at the bottom of the riser. A current at 0 degrees gave the highest bending moments in z-direction and a current at 90 degrees gave the highest bending moments in y-direction. A comparison of the response from the simplified motion and the true drift motions showed that the moments were significantly larger in the simplified analysis. The investigation from wave effects showed an increase in the moment at the top of the riser. This led to the conclusion that wave kinematics must be considered in the method.

One combination of headings was investigated in terms of yield and fatigue. The worst bending moments from the resultant moment within the limiting conditions were sea state 6, 7, and

8. Sea state 8 gave the highest moment of approximately 475kNm at the bottom of the riser. Sea state 6 gave the highest bending moment at the top of the riser of approximately 250kNm. The the standard deviation, effective tension, shear force and resultant bending moment were investigated in terms of yield for sea state 6, 7, 8 for a 3-hour sea state.

The fatigue damage from the time domain analysis gave low damage from all the three cycle counting methods. This was surprising since the moments and axial force showed variations over the riser, which would give stress variations. A sensitivity analysis with SCF 10 showed that sea state 6, 5 and 4 gave an increase in damage at the top and bottom part of the riser, and sea state 1-7 and 14-19 showed a difference when SCF was 20. Rainflow counting, when SCF was 10, gave the highest damage of 1.5E-5 at top from sea state 4, compared to the statistic and spectrum method. From SCF 20, sea state 4 gave a damage of 1.35E-3 at the top with rainflow counting. Fatigue hand calculations showed that sea state 4 gave the highest damage at the top of the riser, but sea state 15 and 16 gave the next highest. Further investigation should be performed in order to obtain agreement in the results from Flexcom and the hand calculations.

A comparison of the fatigue analysis with no drift motions showed that the damage remained unchanged. This could be because the drift motions are not significant enough to cause stress variations. The wave effects are also not large enough to contribute to significant stress cycles of the riser, which could be due to the limiting condition of the wave heights. Other reasons could be that the high top tension, in combination with the stiff elements, prevent stress variations of the riser.

The results from the VIV analysis showed also low damage, but oppose to the time domain analysis, the largest damage occurred at the bottom of the riser, close to 1.15E-5 for SCF 1 and 0.47 for SCF 9. The combination of the current profile from the metocean report and the surface velocity from the standard is perhaps not significant enough to cause large damage to the riser. Other possibilities could be that the S-N curve is too conservative. This could also be the reason for the low damage in the time domain analysis.

Based on the results from the different analysis, the potential of the methodology is shown. With further work, as discussed in chapter 8, the methodology can hopefully be a useful tool when developing new standards for deeper water depths.

Chapter 8

Further work

The methodology presented in this chapter serves as a framework for the mechanical assessment of riser joints. One geometry case has been investigated, but in order to validate the methodology the response from several cases should be studied. An investigation of different riser lengths, combinations of headings, environments and other drilling platforms, i.e.jack-up, could also be investigated for a broader application of the method.

Since the results from the fatigue analysis and VIV analysis gave a low damage, further investigations of the applied loads, structural properties and fatigue data should be conducted. Additionally, since the hand calculations gave results which disagreed with the results from the Flexcom analysis, further investigations of the calculations of stress cycles should be conducted.

Since the drilling phase has been investigated in the analysis, other phases could be studied such as the installation and tripping phase. In addition, since the riser has been investigated in connected condition, other conditions such as disconnected, drift-off or emergency connect could be investigated in order to broader the application of the methodology. All sea states should then be taken into account in disconnected condition.

Due to time limitations, the focus has been on the global load analysis, fatigue analysis and VIV analysis. In order to obtain the exact damage for given hotspots, a local analysis of the joints on the riser should be conducted in a finite element software.

References

Ahmad, s., & Datta, T. (1989). Dynamic Response of Marine Risers. *Engineering Structures*, *11*(3), 179-188. doi: 10.1016/0141-0296(89)90005-9

Ahmad, s., & Datta, T. (1992). Nonlinear Response Analysis of Marine Risers. *Computers & Structures*, *43*(2), 281-295. doi: 10.1016/0045-7949(92)90145-P

Allen, D. (1998, May). *Vortex-Induced Vibration of Deepwater Risers*. Paper presented at Offshore Technology Conference, Houston.

Almar-Næss, A. (1985). *Fatigue handbook: Offshore Steel Structures*. Trondheim: Tapir akademisk forlag.

Amdahl, J. (2014). *TMR4205 Buckling and Ultimate Strength of Marine Structures, Chapter 2: Buckling of bars and frames*. Retrieved 06.04.2016, from `http://www.ivt.ntnu.no/imt/courses/tmr4205/literature/chpt2_Buckling_of_bars_and_frames.pdf`

API. (2007). *API 2INT-MET: Interim Guidance on Hurricane Conditions in the Gulf of Mexico*.

API. (2010a). *API RP 16Q: Recommended Practice for Design, Selection, Operation and Maintenance of Marine Drilling Riser Systems*.

API. (2010b). *API SPEC 16R: Specification for Marine Drilling Riser Couplings*.

Berek, G. (2016). *Changing Practice in Gulf of Mexico Design and Operating Criteria*. Retrieved 02.05.2016, from `http://www.iooc.us/wp-content/uploads/2010/09/Changing-Practice-in-Gulf-of-Mexico-Design-and-Operating-Criteria.ppt`

Berge, S. (2006). *Fatigue and Fracture Design of Marine Structures II: Fatigue Design of Welded Structures.* Trondheim: Department of Marine Technology, NTNU.

Bureau Veritas. (2015a). *Ariane8 User guide.* Paris: Bureau Veritas.

Bureau Veritas. (2015b). *NR 493 DT R03 E: Classification of Mooring Systems for Permanent and Mobile Offshore Units.*

Bureau Veritas. (2016a). *Internal metocean report.*

Bureau Veritas. (2016b). *NR 569 DT R01 E:Classification of Drilling Ships.*

Burke, B. (1973, May). *An Analysis of Marine Risers For Deep Water.* Paper presented at Offshore Technology Conference, Houston.

Campbell, M. (1999, March). *The Complexities of Fatigue Analysis for Deepwater Risers.* Paper presented at Deepwater Pipeline Technology Conference, New Orleans.

Chakrabarti, S. (2005). *Handbook of Offshore Engineering* (Vol. 2). Oxford: Elsevier.

Chen, J., Duan, M., & Tian, K. (2012). Dynamic Response and Fatigue Damage Analysis for Drilling Riser. In *Proceedings of 2012 International Conference on Mechanical Engineering and Material Science (MEMS 2012),28-30 December 2012, Shanghai, China* (p. 704-707). Shanghai: Atlantis press.

Claxton. (2014a). *Making Drilling Riser Systems Happen.* Retrieved 14.03.2016, from `http://claxtonengineering.com/wp-content/uploads/2014/10/Claxton-Riser-Systems-Brochure.pdf`

Claxton. (2014b). *Surface risers, Comprehensive Surface Riser Supply From the North Sea Leader.* Retrieved 14.03.2016, from `http://claxtonengineering.com/wp-content/uploads/2014/10/Surface-Risers-2.pdf`

DNV. (2010a). *DNV-OS-F201: Dynamic Risers.*

DNV. (2010b). *DNV-RP-F204: Riser Fatigue.*

DNV. (2011a). *DNV-RP-C203: Fatigue Design of Offshore Steel Structures.*

DNV. (2011b). *Wellhead Fatigue Analysis Method: JIP Structural Well Integrity, Statoil, Marathon, Lundin, Eni, Total, ExxonMobil, BP, BG Group, Talisman, Det Norske, Shell* (No. /DNV Reg No.:2011-0063/12Q5071-26).

DNV GL. (2015). *DNVGL-OS-C101: Design of Offshore Steel Structures, General-LRFD Method.*

Dril-Quip. (2014). *Rapid-dePloy, Marine Drilling System.* Retrieved 10.02.2016, from `http://www.dril-quip.com/resources/catalogs/05.%20Rapid%20Deploy%20Marine%20Drilling%20Riser%20System.pdf`

Dumont, M. (2016). *Personal communication.*

Faltinsen, O. (1998). *Sea Loads on Ships and Offshore Structures.* Cambridge: Cambridge University Press.

GE Oil & Gas. (2008). *Capital Drilling Equipment, Advanced, Field-proven Risers, Diverters and Connectors.* Retrieved 01.02.2016, from `http://site.ge-energy.com/businesses/ge_oilandgas/en/literature/en/downloads/capital_drilling_equipment.pdf`

Haver, S. (2013). *Prediction of Characteristic Response for Design Purposes (PRELIMINARY VERSION).* Statoil.

Holm, H., Holden, H., & Russo, M. (2013). Wellhead Fatigue Analysis Method: Steps for Improving the Quality of the Global Riser Analyses. In *Proceedings of the Twenty-third (2013) International Offshore and Polar Engineering Conference, 30 June-5 July, Anchorage, Alaska* (p. 161-169). Anchorage: International Society of Offshore and Polar Engineers.

Hyne, N. (2001). *Nontechnical Guide to Petroleum Geology, Exploration, Drilling, and Production* (2nd ed.). Tulsa: Penn Well Corporation.

Kavanagh, K., Dib, M., Balch, E., & Stanton, P. (2002, May). *New Revision of Drilling Riser Recommended Practice (API RP 16Q).* Paper presented at Offshore Technology Conference, Houston.

Langen, I., & Sibjørnsson, R. (1979). *Dynamisk analyse av konstruksjoner.* Trondheim: Tapir akademiske forlag.

Larsen, C. (2011). *Vortex Induced Vibrations: VIV: A Short and Incomplete Introduction to Fundemental Concepts.* Trondheim: Department of Marine Technology, NTNU.

Larsen, C. (2014). *TMR4182 Marin Dynamikk.* Trondheim: Akademika forlag.

Maclachlan, M. (1987). *An Introduction to Marine Drilling.* Ledbury: Oilfield Publications Limited.

MARINTEK. (2013). *RIFLEX User Manual V4.0rev3.* Trondheim: MARINTEK.

MARINTEK. (2015a). *RIFLEX Theory Manual V4.6v0.* Trondheim: MARINTEK.

MARINTEK. (2015b). *SIMA user guide.* Trondheim: MARINTEK.

Mather, A. (2011). *Offshore Engineering and Production* (3rd ed.). Livingston: Witherby Publishing Group Ltd.

Matrix Composites and Engineering. (2014). *Drilling Riser Buoyancy Systems.* Retrieved 14.03.2016, from `www.offshore-europe.co.uk/__novadocuments/99923?v=635757726584230000`

Moan, T. (2003). *TMR4190 Finite Element Modelling and Analysis of Marine Structures.* Trondheim: Department of Marine Technology, NTNU.

Monroy, C. (2015). *HydroStar training.* Paris: Bureau Veritas.

Morooka, C., Coelho, F., Shiguemoto, D., Franciss, R., & Matt, C. (2006). Dynamic Behavior of a Top Tensioned Riser in Frequency and Time Domain. In *Proceedings of the Sixteenth (2006) International Offshore and Polar Engineering Conference, 28 May-2 June, San Francisco, California, USA* (p. 31-36). San Francisco: International Society of Offshore and Polar Engineers.

Myrhaug, D. (2007). *TMR4180 Marin Dynamikk: Uregelmessig sjø.* Trondheim: Akademika forlag.

Oil States Industries. (2012a). *Riser & Drilling Products, OR-6C connector.* Retrieved 11.03.2016, from `http://oilstates.com/wp-content/uploads/OR-6C-Connector.pdf`

Oil States Industries. (2012b). *Riser & Drilling Products, OR-F connector.* Retrieved 11.03.2016, from `http://oilstates.com/wp-content/uploads/OR-F-Connector.pdf`

Oil States Industries. (2016a). *Flexjoint Products*. Retrieved 14.03.2016, from http://oilstates.com/riser-systems-conductor-solutions/drilling/flexjoint-products/

Oil States Industries. (2016b). *Riser Connectors*. Retrieved 14.03.2016, from http://oilstates.com/riser-systems-conductor-solutions/drilling/riser-connectors-jackups/

Oil States Industries. (2016c). *Riser Connectors*. Retrieved 14.03.2016, from http://oilstates.com/riser-systems-conductor-solutions/drilling/riser-connectors-semisub/

Pettersen, B. (2007). *TMR4247 Marin Teknikk 3-Hydrodynamikk*. Trondheim: Department of Marine Technology, NTNU.

Sævik, S. (2016). *Personal communication*.

Schlumberger. (2015). *Drilling Products Overview, Total Rig Package Solutions for Your Drilling Needs*. Retrieved 28.01.2016, from https://www.c-a-m.com/-/media/cam/resources/2014/10/16/18/24/drilling-products-overview-catalog.ashx

Sexton, R., & Agbezuge, L. (1976, May). *Random Wave and Vessel Motion Effects on Drilling Riser Dynamics*. Paper presented at Offshore Technology Conference, Houston.

Sparks, C. (1984). The Influence of Tension, Pressure and Weight on Pipe and Riser Deformations and Stresses. *Journal of Energy Resources Technology, 106*(1), 46-54. doi: 10.1115/1.3231023

Steinkjer, O., Sødahl, N., & Grytøyr, G. (2010). Methodology for Time Domain Fatigue Life Assessment of Risers and Umbilicals. In *Proceedings of the ASME 2010 29th International Conference on Ocean, Offshore and Arctic Engineering (OMAE2010), June 6-11, 2019, Shanghai, China* (p. 177-184). Shangai: ASME.

Suzuki, H., Sævik, S., Chai, S., Chatzigeorgiou, Y., Howells, H., Kuiper, G., ... Watanabe, Y. (2015). Risers and Pipelines. In *Proceedings of the 19th International Ship and Offshore Structures Congress* (Vol. 2, p. 867-902). Cascais: Taylor & Francis Group.

Toderan, C. (2015). *Bureau Veritas proposal N° DTO4 -6 m Thesis: Assessment of Marine Riser Joints during Offshore Drilling Operation*. Paris: Bureau Veritas.

Toderan, C. (2016). *Personal communication.*

Wood Group Kenny. (2015). *Flexcom manual V8.4.1.* Galway: Wood Group Kenny.

Young, R., Fowler, J., Fisher, E., & Luke, R. (1978). Dynamic Analysis as an Aid to the Design of Marine Risers. *Journal of Pressure Vessel Technology, 100*(2), 200-205. doi: 10.1115/1.3454452

Appendix A

Top tension calculations

Properties of the foam, fluid and steel are given in table A.1.

Fully submerged joints	85	[-]
Partly submerged joints	1	[-]
Steel density	7850	[kg/m^3]
Foam density [3]	800	[kg/m^3]
Waterbased density [3]	1250	[kg/m^3]
Oilbased density [3]	980	[kg/m^3]
Saltwater density	1025	[kg/m^3]
G-modulus	7.93E+10	[N/m^2]
E-modulus	2.1E+11	[N/m^2]

Table A.1: Material properties

Areas of the foam, steel and fluid for the buoyancy joint are given in table A.2.

A_{steel} [m^2]	A_{foam} [m^2]	A_{fluid} [m^2]
0.0372	0.3346	0.2091

Table A.2: Steel, foam and fluid area for buoyancy joint

[1] Weight of pipe includes the weight of foam, waterbased fluid and steel

[2] At the LFJ

[3] Given by Toderan (2016)

Mass for one buoyant joint is calculated in table A.3.

	M_{steel} [kg]	M_{foam} [kg]	$M_{waterbased}$ [kg]	$M_{oilbased}$ [kg]	Buoyancy [kg]
Joint (23m)	6714	6156	6012	4713	13694
Lines	1208.4				
Connection	40				
Total	7962	6156	6012	4713	13694

Table A.3: Mass calculations for one buoyant joint

Mass for the partly submerged joint is calculated in table A.4.

	M_{steel} [kg]	M_{foam} [kg]	$M_{waterbased}$ [kg]	$M_{oilbased}$ [kg]	Buoyancy [kg]
Not submerged (7m)	2411		1830	1435	
Submerged (16m)	5551	4283	4182	3279	9526
Total	7962	4283	6012	4713	9526

Table A.4: Mass calculations for partly submerged buoyant joint

Mass for all buoyancy joints are calculated in table A.5.

	M_{steel} [kg]	M_{foam} [kg]	$M_{waterbased}$ [kg]	$M_{oilbased}$ [kg]	Buoyancy [kg]
Total (86 joints)	684732	527543	517032	405318	1173516

Table A.5: Mass calculations for all buoyancy joints

Top tension calculations are shown in table A.6

Top tension	250000	600000	[kg]
Buoyancy	1173516	1173516	[kg]
Weight of pipe [1]	1729307	1729307	[kg]
Required [2]	-305.8	44	[tonnes]

Table A.6: Top tension calculations

[1] Weight of pipe includes the weight of foam, waterbased fluid and steel

[2] At the LFJ

[3] Given by Toderan (2016)

Appendix B

Buckling calculations

The transition between tension and compression must be found when 250 tonnes is applied as top tension. Equilibrium was found at 38.49 joints from the top by subtracting the top tension and the buoyancy from the weight of the pipe. The mass calculations are given in table B.1.

	$M_{steel\ \&\ fluid\ \&\ foam}$ [kg]	M_{foam} [kg]	Buoyancy [kg]
Total (38.49 joints)	537859	235071	522914

Table B.1: Mass calculations for the joints in tension

The top tension calculations for the 38.49 joints are given in table B.2.

Top tension	250000	[kg]
Buoyancy	521682	[kg]
Weight of pipe [1]	772930	[kg]

Table B.2: Top tension calculations for joints in tension

The buckling calculations for the beam in compression (47.51 joints) are shown in table B.3. The average force of the required load has been used to calculate the actual load.

Length f/bottom	1093	[m]
Critical load	2339	[N]
Actual load	1499903	[N]

Table B.3: Buckling calculations

Appendix C

Damage calculations

Sea state 4 has probability of occurrence equal to 0.04746. The damage is found in table C.1.

Element	No. of cycles	Equivalent range [MPa]	Damage [1]
1	2949248.790	0.25	
	2170286.896	0.75	
	612363.108	1.25	
	135080.097	1.75	
			3.044E-12
27	6083107.046	0.25	
	684405.826	0.75	
			1.113E-13
30	10387659.48	0.25	
			6.707E-15
260	7704068.213	0.25	
	576341.748	0.75	
	9005.340	1.25	
			1.136E-13
466	4592723.307	0.25	
	1688501.216	0.75	
	1211218.205	1.25	
	567336.409	1.75	
	324192.233	2.25	
	229636.165	3.25	
	36021.359	5.00	
	9005.334	7.00	
			2.508E-10

Table C.1: Damage calculations for sea state 4

Sea state 5 has probability of occurrence equal to 0.00613. The damage is found in table C.2.

Element	No. of cycles	Equivalent range [MPa]	Damage [1]
1	3111344.907	0.25	
	1909132.041	0.75	
	508801.700	1.25	
	45026.699	1.75	
			2.347E-13
27	5966037.629	0.25	
	508801.996	0.75	
			1.081E-14
30	10108493.940	0.25	
			8.430E-16
260	7447416.028	0.25	
	324192.233	0.75	
			7.191E-15
466	5020476.948	0.25	
	1972169.420	0.75	
	900533.982	1.25	
	391732.282	1.75	
	243144.175	2.25	
	171101.457	3.25	
	9005.334	5.00	
			9.723E-12

Table C.2: Damage calculations for sea state 5

[1] Coefficients used for calculating the damage: m=5 & $\bar{a}$=7.178E+16

Sea state 15 has probability of occurrence equal to 0.12587. The damage is found in table C.3.

Element	No. of cycles	Equivalent range [MPa]	Damage [1]
1	9635888.330	0.25	
	121574.292	0.75	
			6.709E-14
27	9910556.174	0.25	
			1.697E-14
30	11441491.700	0.25	
			1.959E-14
260	10734559.710	0.25	
			1.838E-14
466	6276835.669	0.25	
	3759797.549	0.75	
	1166212.653	1.25	
	207126.572	1.75	
	22513.758	2.25	
			1.605E-11

Table C.3: Damage calculations for sea state 15

[1] Coefficients used for calculating the damage: m=5 & $\bar{a}$=7.178E+16

Sea state 16 has probability of occurrence equal to 0.22149. The damage is found in table C.4.

Element	No. of cycles	Equivalent range [MPa]	Damage [1]
1	7632256.872	0.25	
	468291.867	0.75	
			3.659E-13
27	10860769.070	0.25	
94558.935			1.020E-13
30	11211987.970	0.25	
	211631.902	0.75	
			1.888E-13
260	10937316,78	0.25	
	36022.451	0.75	
			5.934E-14
466	7114434.134	0.25	
	3160970.103	0.75	
	774482.703	1.25	
	72044.903	1.75	
	9005.613	2.25	
			1.488E-11

Table C.4: Damage calculations for sea state 16

[1] Coefficients used for calculating the damage: m=5 & $\bar{a}$=7.178E+16

Appendix D

Response amplitude operators

Heave

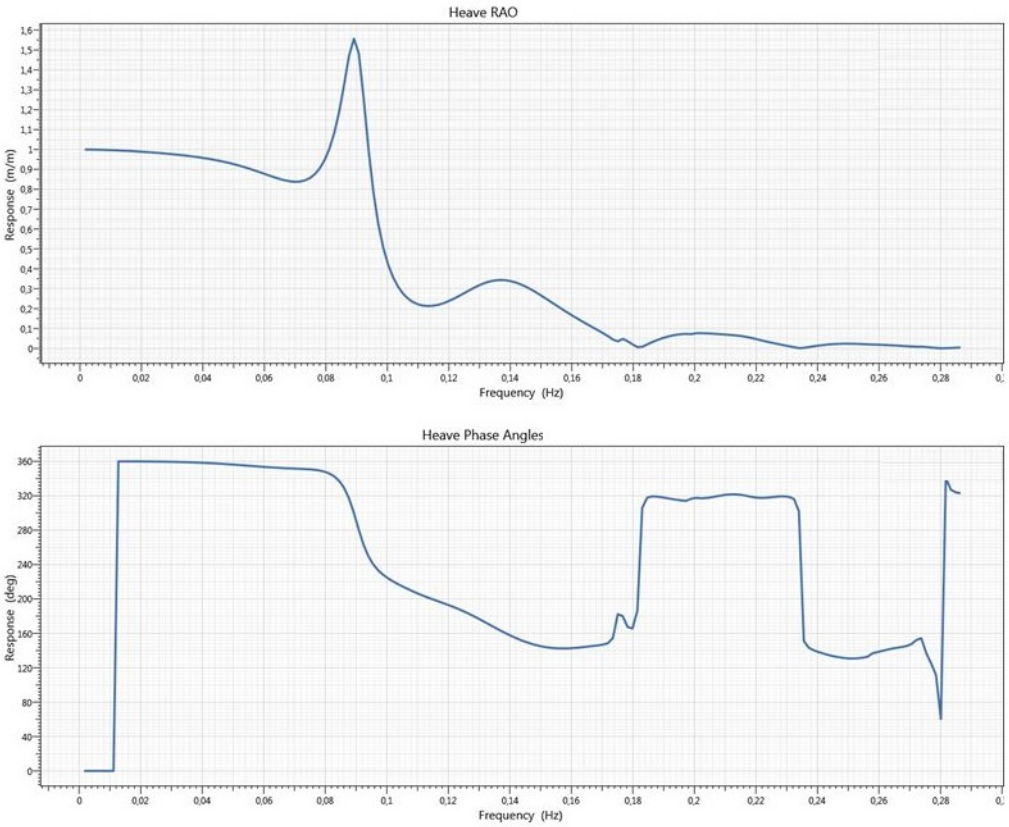

Figure D.1: Heave, 0 degrees

Surge

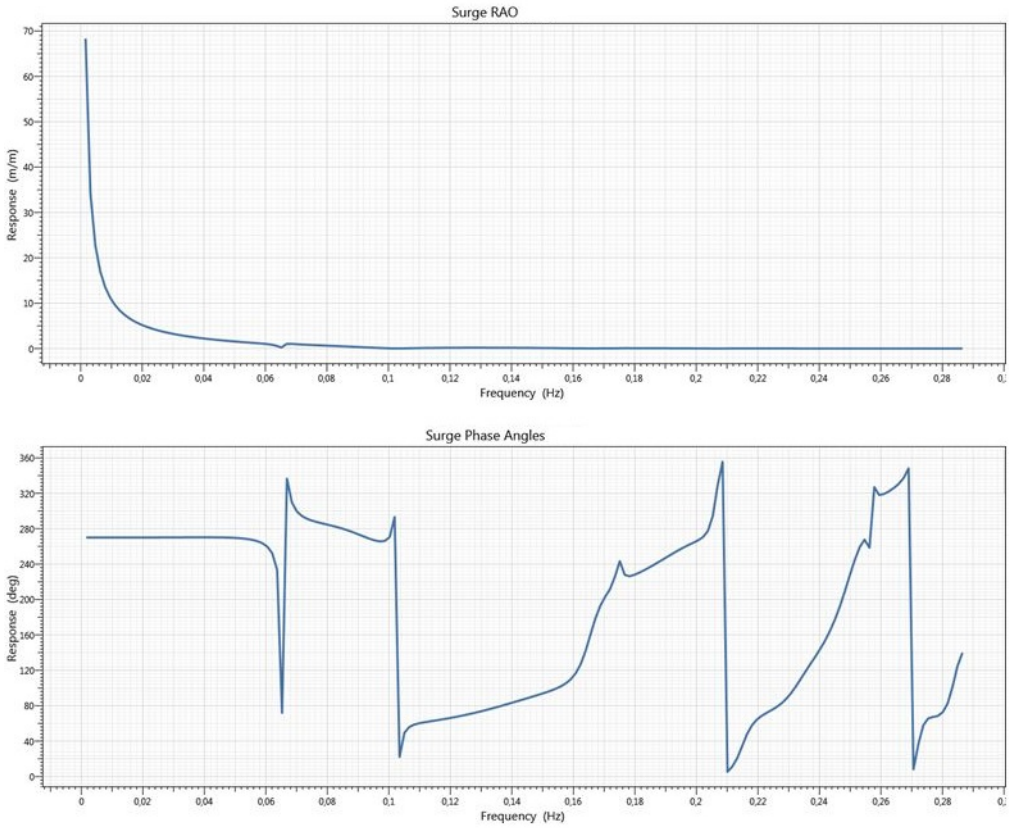

Figure D.2: Surge, 0 degrees

Pitch

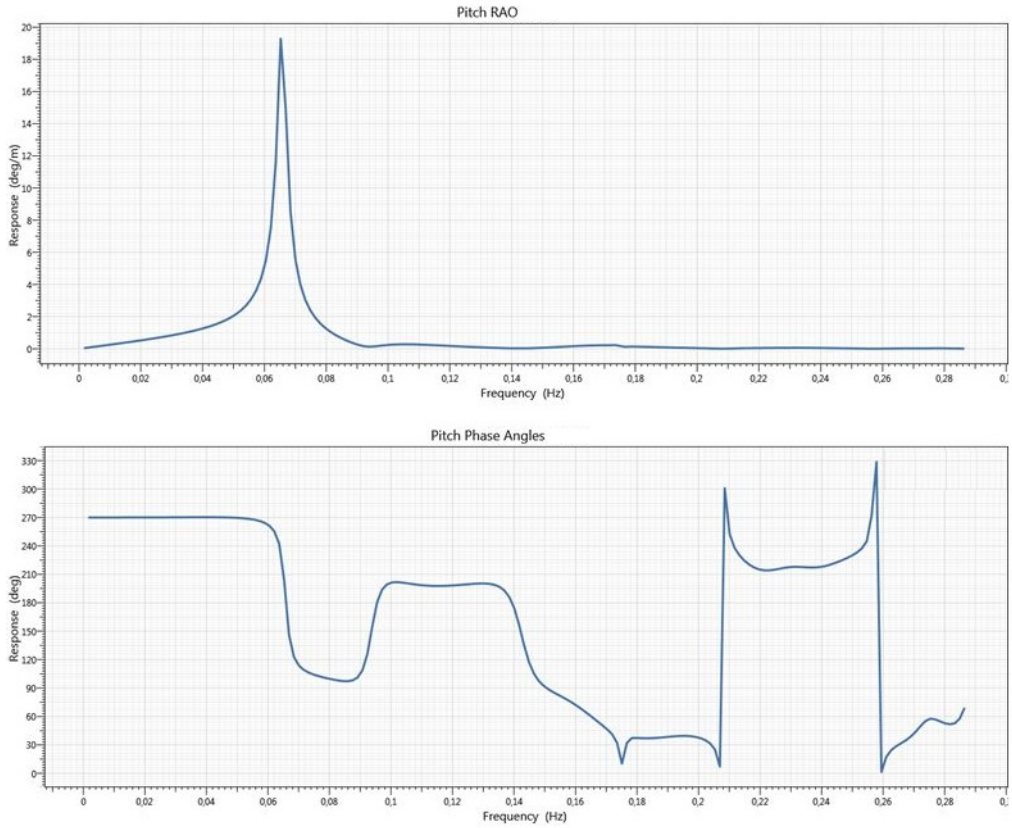

Figure D.3: Pitch, 0 degrees

Appendix E

Workplan

BV Marine&Offshore Division DTO4 – Subsea&Drilling	Nr : ---	29/01/2016 Paris - HO
Scope : Internship of Martine Bay – Memo Jan 16	Concerns: Catalin Toderan (CTN) Martine Bay (MBY)	Author(s) : CTN MBY Validation : CTN

1st Memo of M. Bay Internship – 29 Jan 2016

1. **Scope of the internship – discussion**

   The scope was discussed and clarified during the first week of internship, in accordance with the internship agreement from 2015. The understanding is as follows:

   - The work do not concern any operational project, certification or consultancy service
   - The goal is to define and validate a full methodology for the assessment of drilling risers and components with regard to yielding and fatigue; this methodology will be used by BV in the next future to perform a large number of tests to calibrate acceptance criteria for risers and risers joints (this calibration is outside the scope of the internship)
   - The validation is done on a number of case studies selected by MBY and CTN based on the documentation carried out during the first phase of the work
   - The work will involve BV specialists from various departments : Research Dep (Hydro, Metocean), Operational team DTO2 (use of Flexcom and Shear7 tools), Operational Team DTO1 or Tecnitas (Detailed FEM, fatigue assessment).

2. **Internship Workplan**

   CTN proposes the following workplan:

Phase 1	Technology documentation : - Design and manufacturing of risers and components : models, types, suppliers - Technical standards (API, NORSOK, DNVGL) - Calculation tools background (Flexcom, Shear 7)	Estimated duration 3 weeks
Phase 2	Investigation on environmental loads and familiarization with associated software tools (Hydrostar). Co-work with the Research Department. Targeted regions will be: N Sea Norway, GoM, Brazil or West Africa. Selection of sites for case studies.	Estimated duration 1 month
Phase 3	Technical investigation on VIV and Shear 7 limitations. Test of Shear 7 for various riser sections	Estimated duration 1 month
Phase 4	Final selection of 2 or 3 case studies (site+technology)	Estimated duration 1 week
Phase 5	Modeling, validation of models, solving and postprocessing : Flexcom, Shear7, Hydrostar, Abaqus Validation of the method and identification of limitations	Estimated duration 2.5 months
Phase 6	Final reporting and presentation	0.5 months

The detailed scheduling is kept flexible for fitting with the availability of BV personnel, in particular operational teams. For this reason, we may have some overlaps for the phases 1 to 4.

Appendix F

Contents in Zip-file

Flexcom

Flexcom program folder: Contains all of the Flexcom files **.keyxm* and the project file *Drilling.fcproj*.

Input files folder:

- Excel input files for using "Excel variations" in Flexcom: *Sea_ states_ first.xlsx, Sea_ states_ RAO.xlsx, Time_ domain_ first.xlsx, Time_ domain_ RAO.xlsx* - Input file in Ariane: *Batch.txt*.

- Input files for drift motions in Flexcom:*Displacement_ LF_ i.dat*, i=0,...32

- RAOs for 0 degree heading: *RAOS.incx*.

Post-processing

- Time domain output files: Data to create plots for final time domain analysis.

- Fatigue output files: Data to create plots for fatigue analysis.

- Histograms: Data for calculating damage by hand.

- Shear7 output files: Data to create plots for VIV analysis.

Excel

Fatigue calculations.xlsx: Fatigue hand calculations from appendix C.

Top tension calculations.xlsx: Top tension and buckling calculations from appendix A and B.

Other

Poster.pdf: Poster for poster exhibition at NTNU.